Nonlinear behaviour of ultracold atoms in optical dipole traps:

Large atomic light shifts, a quantum phase transition, and interaction-dependent dynamics

PhD Thesis

Simon Coop

July 11, 2018

Abstract

This thesis reports on theory and results from two experiments related to nonlinear behaviour in ensembles of optically-trapped ultracold atoms.

The first experiment, performed at ICFO in Barcelona, regards the prediction and measurement of strong ac Stark shifts (light shifts). We present a numerical method based on Floquet's theorem for calculating light shifts to all orders with fewer approximations than the usual calculation based on second-order perturbation theory. The method is experimentally validated by performing absorption spectroscopy of a optically-trapped cloud of cold ^{87}Rb atoms in three scenarios. 1) The atoms are trapped in a singly-polarised monochromatic dipole trap with a wavelength detuned $\sim 30\,\mathrm{nm}$ from the nearest atomic transition. 2) A bichromatic two-polarisation trap, where one wavelength is much closer to atomic transitions ($\sim 0.01\,\mathrm{nm}$ detuning), and finally 3) Another monochromatic trap but with the wavelength variable and scanned close to atomic transitions, again with $\sim 0.01\,\mathrm{nm}$ detuning but three times the intensity of the near-resonant light in the previous experiment, producing nonlinear light shifts of the D_2 transition up to $\sim 1\,\mathrm{GHz}$. We discuss the potential application of the method to the accurate measurement of electric dipole transition matrix elements. The method is extended to calculate atomic energy level shifts in the presence of light and static magnetic fields.

The second experiment was performed at LENS in Florence, and involves ^{39}K atoms with tunable interactions cooled into the ground- and first-excited state of a two-mode optical potential. We derive a differential equation to describe behaviour of a two-mode quantum system with tunable interactions, and then solve it to model behaviour of the system in the three distinct regimes of attractive, zero, and repulsive interatomic interactions. With attractive interactions the system is shown to exhibit a quantum phase transition, and with repulsive interactions is shown to exhibit nonlinear dynamics, including behaviour analogous to a superconducting Josephson junction.

As background material the thesis presents a summary of standard laser cooling and trapping techniques, namely Doppler cooling, $\sigma^+ - \sigma^-$ polarisation gradient cooling, magneto-optical trapping, and optical trapping. Optical traps are discussed in detail. We discuss relevant basic physics, derive and analyse a technique for using light shifts to characterise an optical trap, discuss optical Bose-Einstein condensation and control of light intensity to reduce noise-induced heating. Also described is a theoretical proposal for optical evaporation with a constant-depth trap.

Resumen

Esta tesis describe la investigación teórica y los resultados de dos experimentos relacionados con el comportamiento no lineal en un conjuntos de átomos ultrafríos atrapados ópticamente.

En el primer experimento, realizado en ICFO en Barcelona, se presenta la predicción y unos resultados de fuertes cambios de ac Stark (light shifts). Se explica un método numérico basado en el teorema de Floquet para calcular light shifts a todos órdenes con menos aproximaciones que el método habitualmente usado basado en teoría de perturbaciones de segundo orden. El método se valida experimentalmente mediante la realización de espectroscopía de absorción en una nube de átomos de ^{87}Rb ópticamente atrapados en tres escenarios distintos. En el primero, los átomos están atrapados en una trampa de dipolo monocromática de polarización única con una longitud de onda desintonizada $\sim 30\,\mathrm{nm}$ a la transición atómica más cercana. En el segundo se emplea una trampa bicromática de dos polarizaciones, donde una longitud de onda está mucho más cerca de las transiciones atómicas ($\sim 0.01\,\mathrm{nm}$ fuera de resonancia). En el tercer y ultimo escenario, se usa una trampa monocromática con la longitud de onda variable y escaneado cerca de transiciones atómicas, nuevamente con $\sim 0.01\,\mathrm{nm}$ desintonizada pero tres veces más intensa que la luz casi resonante del experimento anterior, produciendo light shifts no lineales de la transición D_2 hasta $\sim 1\,\mathrm{GHz}$. Se discute la aplicabilidad del método para la medición precisa de los elementos de la matriz de transición dipolar eléctrica. Por último, el método se extiende permitiendo calcular los cambios de niveles de energía atómica en presencia de luz y campos magnéticos estáticos.

El segundo experimento que se describe en esta tesis se realizó en LENS, en Florencia, e involucra átomos de ^{39}K con interacciones sintonizables en átomos fríos ocupando al estado fundamental y el primer estado excitado de un potencial óptico de dos modos. Se deriva una ecuación diferencial para describir el comportamiento de un sistema cuántico de dos modos con interacciones sintonizables.

Esta se resuelve para modelar el comportamiento del sistema en tres regímenes distintos de interacciones inter-atómicas: atractivas, nulas y repulsivas. En el caso de interacciones atractivas se muestra que el sistema exhibe una transición de fase cuántica. En presencia de interacciones repulsivas el sistema muestra dinámica no lineal, incluyendo un comportamiento análogo a una unión superconductora de Josephson.

Como material de referencia, la tesis presenta un resumen de las técnicas estándar de enfriamiento y atrapamiento láser, concretamente enfriamiento Doppler, $\sigma^+ - \sigma^-$ enfriamiento por gradiente de polarización, atrapamiento magneto-óptico y atrapamiento óptico. Las trampas ópticas se revisan en detalle. Discutimos la física básica relevante, derivamos y analizamos una técnica para usar los light shift para caracterizar una trampa óptica. Analizamos la condensación óptica de Bose-Einstein y el control de la intensidad de la luz para reducir el calentamiento inducido por el ruido. También se presenta una propuesta teórica para la evaporación óptica con una trampa de profundidad constante.

List of publications

Publications associated with this thesis

S. Palacios, S. Coop, P. Gomez, T. Vanderbruggen, Y. Natali Martinez de Escobar, M. Jasperse, and M. Mitchell, "Multi-second magnetic coherence in a single domain spinor Bose-Einstein condensate," *New Journal of Physics* **20** 053008 (2018).

S. Coop, S. Palacios, P. Gomez, Y. Natali Martinez de Escobar, T. Vanderbrugen, and M. Mitchell, "Floquet theory for atomic light-shift engineering with near-resonant polychromatic fields," *Optics Express* **25** 32550-32559 (2017).

G. Spagnolli, G. Semeghini, L. Masi, G. Ferioli, A. Trenkwalder, S. Coop, M. Landini, L. Pezze, G. Modugno, M. Inguscio, A. Smerzi, and M. Fattori, "Crossing over from attractive to repulsive interactions in a tunneling bosonic Josephson junction," *Physical Review Letters* **118** 230403 (2017).

A. Trenkwalder, G. Spagnolli, G. Semeghini, S. Coop, M. Landini, P. Castilho, L. Pezze, G. Modugno, M. Inguscio, A. Smerzi, and M. Fattori, "Quantum phase transitions with parity-symmetry breaking and hysteresis," *Nature Physics* **12** 826-829 (2016).

Y. Natali Martinez de Escobar, S. Palacios, S. Coop, T. Vanderbruggen, K. Kaczmarek, M. Mitchell, "Absolute frequency references at 1529 and 1560 nm using modulation transfer spectroscopy," *Optics Letters* **40** 4731-4734 (2015).

T. Vanderbruggen, S. Palacios, S. Coop, Y. Natali Martinez de Escobar, and M. Mitchell, "Spontaneous PT symmetry breaking of a ferromagnetic superfluid in a gradient field," *Europhysics Letters* **111** 66001 (2015).

Other publications

S. Chai, J. Fekete, P. McDowall, S. Coop, T. Lindballe, and M. Andersen, "Survival resonances in an atom-optics system driven by temporally and spatially periodic dissipation," *Physical Review A* **97** 033616 (2018).

K. Tielrooij, L. Orona, A. Ferrier, M. Badioli, G. Navickaite, S. Coop, S. Nanot, B. Kalinic, T. Cesca, L. Gaudreau, Q. Ma, A. Centeno, A. Pesquera, A. Zurutuza, H. de Riedmatten, P. Goldner, F. García de Abajo, P. Jarillo-Herrero, and F. Koppens, "Electrical control of optical emitter relaxation pathways enabled by graphene," *Nature Physics* **11** 281-287 (2015).

Contents

Abstract **3**

Resumen **5**

List of publications **7**

1 Introduction **13**
1.1 A brief history of optical dipole traps 13
1.2 This thesis 14

2 Laser cooling of neutral atoms **19**
2.1 Sources of neutral atoms 20
2.2 Doppler cooling 20
2.3 Optical molasses 21
2.4 Magneto-optical trapping 22
2.5 Temperature measurements 23
2.6 Production of cold atoms 24

3 Absorption imaging of cold atoms **25**
3.1 Introduction 25
3.2 Absorption imaging 26
3.3 Noise reduction with an optimised background image 28

4 Optical dipole traps **31**
4.1 Basic physics 32
4.2 Light-shift tomography 34
4.3 Optical Bose-Einstein condensation 41
4.4 Laser intensity control and noise-induced heating 46
4.5 Microwave-assisted constant-depth optical evaporation 49

5 Light shifts with Floquet's theorem 59
5.1 Introduction . . . 59
5.2 Floquet theory of light shifts . . . 61
5.3 Combining light shifts and magnetic fields . . . 64
5.4 Conclusion . . . 66

6 Measurement of strong nonlinear light shifts 69
6.1 Light shifts @ 1560 nm + 1529 nm . . . 70
6.2 Higher precision measurements @ 1529 nm . . . 75
6.3 Conclusion . . . 83

7 Bimodal Bose-Einstein condensate with tunable interactions 85
7.1 Introduction . . . 85
7.2 Theory a of coherent two-mode quantum system . . . 86
7.3 Experimental apparatus . . . 88
7.4 Observables . . . 90
7.5 Dynamics of the double well . . . 94

8 Conclusion & outlook 101
8.1 Conclusion . . . 101
8.2 Outlook . . . 102

A Laser stability transfer with a temperature-controlled fibre interferometer 103
A.1 Temperature control with an Arduino . . . 105
A.2 Frequency control and fringe counting with an Arduino . . . 106
A.3 Calibration of the interferometer . . . 106

B Phase-contrast imaging system for the experiment in Florence 113
B.1 Introduction . . . 113
B.2 Basic theory of PCI . . . 114
B.3 Optical performance of the relay lens . . . 115
B.4 Calculation of light propagation in an atomic cloud . . . 116

C Experiment control system 121
C.1 Software . . . 121
C.2 Hardware . . . 124
C.3 Laser frequency stabilisation and control . . . 125
C.4 Camera . . . 126

D Absorption imaging model for determining detection limits 129
D.1 Noise sources 130
D.2 Atom distribution 130
D.3 Simulating a real measurement 131
D.4 Comparison with real data 132
D.5 Atom-number fluctuations in the double-well 133
D.6 Feasibility of sub-shot-noise resolution 135
D.7 Conclusion 135

Bibliography 137

Chapter 1

Introduction

1.1 A brief history of optical dipole traps

Erwin Schrödinger wrote in 1952 (italics his):

"... we *never* experiment with just *one* electron or atom or (small) molecule. In thought-experiments we sometimes assume that we do; this invariably entails ridiculous consequences ... it is fair to state that we are not experimenting with single particles, any more than we can raise Ichthyosauria in the zoo" [1].

He would probably have been delighted to learn that since the advent of laser cooling, control of single atoms has reached such high fidelity that arrays of trapped single atoms can be deterministically arranged and imaged [2], and we can even measure the interaction of a single atom with a single photon [3, 4][1].

The trapping and observation of single atoms might be considered the ultimate limit of the exquisite manipulation and control of atoms made possible with laser cooling and optical dipole traps. The existence of "radiation pressure" - the force exerted on matter by light - has been known for centuries. Nichols and Hull in 1903 refer to Kepler studying the pressure of sunlight on the tails of comets [7]. Fast-forward to 1970 when Art Ashkin reported on what was probably the first controlled trapping of particles using the optical dipole force, where he trapped micron-sized latex spheres suspended in water with a pair of counter-propagating focused laser beams [8]. Since then the field has exploded, with the first report

[1] He probably would also have been delighted to learn that a recently extinct goat was brought back to life by cloning in 2009 [5], and that responsible management of de-extincted species is now the subject of serious academic debate [6].

of a cloud of atoms trapped in a single laser beam in vacuum in 1986 (again involving Art Ashkin) [9]. Optical traps have also found a huge application in the biological sciences, being used to trap and observe viruses and bacteria as early as 1987 (again by Art Ashkin) [10].

Nowadays, as well as the single-atom trapping mentioned above, optical dipole traps (ODTs) are used for a variety of precise and delicate physics. For example, the first Bose-Einstein condensate (BEC, a form of matter where all the constituent particles have the same spatial wavefunction) made all-optically was reported in 2001 [11], ODTs are used for the study of exotic quantum states of matter (e.g. observation of the superfluid to Mott insulator phase transition [12]), quantum simulators (e.g. the creation of artificial graphene [13]), and precision magnetometry. Optical lattices - spatially-periodic potentials made by interfering two or more laser beams - are crucial to the latest generation of atomic clocks. Optical lattice atomic clocks have reached a relative uncertainty on the order of 10^{-18} [14], and are poised to reach 10^{-20} in the near future [15]. Current uncertainty is small enough to measure relativistic time-dilation by moving 2 cm higher or lower in the Earth's gravitational field.

This thesis presents work related to two experiments employing optical dipole traps. One experiment in Barcelona studies the interaction of laser-cooled atoms in an optical dipole trap with the trapping light itself, and how this affects the internal structure of the atoms. The results of this project may be important for improving understanding of how atoms interact with light through the ac Stark effect. The other project involves atoms cooled into the ground state of a two-mode optical potential. This project demonstrates the first observation of a quantum phase transition with full control over all the experimentally-relevant variables, and also studies the system in a regime where the behaviour is analogous to a superconducting Josephson junction.

1.2 This thesis

The majority of my PhD was spent in the group of Professor Morgan Mitchell at ICFO in Barcelona. When I joined in mid-2013, the group in Barcelona was just beginning construction of a new optical BEC experiment, and the first two years of my PhD were mostly spent on the construction and characterisation of this experiment. Mid-2015 I moved to Florence to work in the group of Dr. Marco Fattori at LENS in Florence for one year. The experiment in Florence had completed construction some time before I joined, and was already in the

process of gathering scientific data. After one year in Florence I moved back to Barcelona for the remainder of my PhD.

Due in part to these logistical constraints, this thesis is organised as follows: Chapters 2, 3, and 4 describe background material common to both experiments. There is a stronger emphasis on experimental data from the Barcelona experiment, due to the fact I contributed to the construction of this experiment and worked on the calibration of many components. However the material is relevant to both experiments. The 'main' results of the thesis are chapters 5 and 6, which describe theory and experimental results, respectively, from the Barcelona experiment, and chapter 7, which describes some theory and results from the Florence experiment. Each experiment is introduced more thoroughly in its respective chapter, however below are short introductions to both.

The experiment in Barcelona concerns large nonlinear ac Stark shifts (light shifts) of atoms in optical dipole traps. Light shifts are the result of off-resonant light coupling atomic energy levels, resulting in level shifts. Usually these shifts are calculated using second-order perturbation theory, which describes the shifts well in the case they are linear in light intensity and much smaller than the atomic hyperfine splitting. This thesis presents a way of calculating these shifts based on Floquet's theorem. The calculation requires fewer approximations than the perturbative calculation, with the result that the shifts can be nonlinear and larger than the hyperfine splitting and can induce strong mixing of the hyperfine levels. The thesis also presents experimental data of light shifts in ^{87}Rb in a regime where some levels are shifted up to 1 GHz, which disagree with theory by 20-45 MHz. This small discrepancy is not explained in this thesis. As far as I am aware this is the first calculation and measurement of nonlinear light shifts.

The other experiment, in Florence, studies the ground-state phases and dynamics of a two-mode ^{39}K BEC with tunable interactions. ^{39}K has broad Feshbach resonances at a relatively low magnetic field, enabling fine tuning of inter-atomic interactions over positive and negative values. The BEC is formed in double-well potential, with a tunable barrier between the two wells. This combination of tunable interactions and control of the inter-well coupling enables the observation of a variety of interesting physical effects. This thesis reports on the observation of a quantum phase transition, and nonlinear Josephson dynamics.

1.2.1 Outline

Chapter 2 reviews standard laser cooling techniques of neutral atoms. Namely, Doppler cooling, $\sigma^+ - \sigma^-$ polarisation gradient cooling (AKA optical molasses),

magneto-optical traps, and also an explanation of time-of-flight temperature measurements.

Chapter 3 focuses on absorption imaging. First I derive an equation for extracting atomic density data from absorption images, and then describe an algorithmic technique used for reducing noise in processed images.

Chapter 4 discusses optical dipole traps in-depth. Firstly it reviews the basic physics of trapping atoms with far-off resonant light, then reviews a technique for characterising optical dipole traps called light-shift tomography, showing some example measurements. Next is a brief discussion of Bose-Einstein condensation in optical dipole traps, which is relevant to the results presented in Chapter 7. Then I describe a system to control the intensity of the dipole trap lasers in the Barcelona experiment. Finally, I present a new idea for performing optical evaporation without reducing the trap depth, as is done in the standard approach. The idea has not been tested experimentally but the theoretical analysis presented here suggests that it is at least worth further investigation.

Chapter 5 presents a calculation based on Floquet's theorem for calculating atomic light shifts (AKA ac Stark shifts). Starting from Schrödinger's equation, this chapter describes a numerical technique using Floquet's theorem to find the eigenenergies of a periodic Hamiltonian. This result is used in combination with the electric dipole operator to describe light shifts of atoms with an arbitrary number of light fields with arbitrary polarisation, in the electric dipole approximation. The final part of this chapter describes how to include magnetic fields in the light shift calculation, giving a kind of toolbox for engineering of atomic energy levels.

Chapter 6 describes an experiment to measure large nonlinear light shifts to test the theory of Chapter 5, and presents and discusses experimental data. An initial measurement agrees with theory well outside of the linear shift regime to within experimental uncertainty. However a second, more accurate, measurement appears to show a discrepancy between data and theory.

Chapter 7 describes an experiment at LENS in Florence, in the group of Dr. Marco Fattori. This experiment is a ^{39}K BEC experiment with a one-dimensional optical lattice and a tunable inter-atomic interaction strength. The optical lattice is used to realise a two-mode system with tunable coupling between the two modes. The experiment is used to study a quantum phase transition and Josephson physics.

Appendix A describes a transfer lock for stabilising the frequency of a laser used in several of the measurements performed in Chapter 6. Appendix B describes works done towards implementing a phase-contrast imaging system in the Florence experiment. Appendix C outlines the architecture and components of the control system for the Barcelona experiment. Appendix D describes a model of the imaging system in Florence that was used to try and understand the detection limits of that experiment, and whether or not it can be used to detect atom-number squeezing.

Chapter 2

Laser cooling of neutral atoms

All the work described in this thesis depends on having an ensemble of near-stationary neutral atoms, as isolated as possible from the external environment. The realisation of such an ensemble has been made possible by the work of, among others, Steven Chu, Claude Cohen-Tannoudji, and Bill Phillips, who were awarded the 1997 Nobel Prize in physics "for development of methods to cool and trap atoms with laser light" [16]. Their work was based on earlier theoretical proposals and experimental work involving ions [17].

The field of laser cooling of atoms is now quite mature, with most major developments occuring in the last quarter of the 20th century. The field has seen fantastic optimisation over the last twenty years, but the fundamental techniques have remained largely the same. More complicated schemes of cooling, such as Raman sideband cooling or gray molasses, were widely used and understood by the year 2000 [18]. In this section I'll review the most common techniques of optical cooling and trapping of atoms: Doppler cooling, optical molasses, and magneto-optical trapping, all of which were employed for work described in later sections in this thesis. Due to their importance for my work, I describe optical dipole traps, and the final method of laser cooling - optical evaporation - separately in Chapter 4.

2.1 Sources of neutral atoms

Cold-atom physics experiments depend on a source of alkali atoms inside a ultrahigh-vacuum chamber with optical access. Typical background vapour pressures inside a vacuum chamber are $10^{-10} - 10^{-11}$ Torr, which is comparable to the pressure on the surface of the moon [19].

Once ultrahigh vacuum has been reached, there are two standard sources of atoms: most alkali metals have a relatively low melting point, and as such have a relatively high vapour pressure. Thus one can place a lump of solid alkali metal inside a vacuum chamber, which emits enough vapour to perform experiments. In this case differential pumping and transfer techniques are used to move clouds of trapped atoms to regions of the vacuum chamber away from the solid metal, such that the constant uncontrolled vapour emission does not interfere with experiments. An experiment with such a source usually requires a sophisticated multi-chamber vacuum system.

Another standard source of atoms is to use a "dispenser", which consists of an alkali salt inside a tube which can be heated with electric current. The hot metal tube liberates alkali atoms from the salt, forming a beam of atoms which can be switched on and off at will. However there is the danger of accidentally passing too much current through the dispenser, and liberating all the metal at once.

2.2 Doppler cooling

Analogous to stopping a freight train by throwing millions of tennis balls at it, Doppler cooling works by transferring atomic momentum onto a beam of incident laser light. The process can be explained as follows: Imagine an atom is at the intersection of three pairs of counter-propagating laser beams, each pair aligned with a different axis in Cartesian coordinates. All the lasers are slightly detuned to the red of an atomic resonance. If the atom is moving toward any of the six lasers, the Doppler effect causes the laser to be closer to resonance with the atom, which is then more likely to absorb a photon and its corresponding momentum, once absorbed it re-radiates the photon in a random direction. Over many absorption-emission cycles, the atom mostly absorbs photons from the laser beam opposing its direction of motion and the emission averages to zero, thus the atom is cooled. Under the right conditions, this effect can be very strong. Atoms can be cooled from room temperature, with velocities on the order of $\sim \mathrm{km\,s^{-1}}$, to microkelvin ($\sim \mathrm{cm\,s^{-1}}$) over a distance of centimetres. Assuming a two-level atom, the minimum achievable temperature with this effect is

$$T_D = \frac{h\Gamma}{2k_B} \tag{2.1}$$

where h is Planck's constant, Γ is the transition linewidth in Hz, and k_B is Boltzmann's constant. For rubidium cooled on the D_2 line, this temperature is about 150 µK. A more quantitative analysis can be found in [20].

2.3 Optical molasses

In 1987, Bill Phillips and colleagues experimentally measured much lower temperatures in ensembles of laser cooled atoms than what was theoretically possible according to Eq. (2.1) [21]. It was recognised that the derivation of the limit in Doppler cooling naively assumes a two-level system, however it was thought the multi-level structure was irrelevant: the Zeeman sublevels are all degenerate and, in the case of sodium which was used in the experiments, other levels are too far off-resonant to be relevant [17]. The mechanism behind this sub-Doppler cooling was explained by Dalibard and Cohen-Tannoudji in 1989, and it turned out the multi-level Zeeman sub-structure was important after all [22].

The sub-Doppler cooling mechanism requires two things: an atom with ground-state angular momentum $J_g \geq 1$, and red-detuned laser light with a polarisation gradient. There are two possible ways of creating a polarisation gradient, the most common technique is to counter-propagate two beams of opposite circular polarisation, creating an optical lattice of constant intensity but linearly changing polarisation (this configuration is known as $\sigma^+ - \sigma^-$ polarisation-gradient cooling). This adds a term to the atomic Hamiltonian

$$V = kvJ_z \tag{2.2}$$

where k is the magnitude of the wavevector of the light, v is the velocity of the atom in the lab frame, and J_z is the projection of atomic angular momentum on the quantisation axis. It can be seen that this term removes the degeneracy of the ground state levels, in a way that looks like a magnetic field. In one picture of this effect, this fictitious magnetic field modifies the steady-state occupation of the ground state levels in such a way that a moving atom is predominately in the state which absorbs photons from the beam opposing its motion. Thus whichever way the atom moves it feels a force opposing its motion, while if it is stationary it is equally likely to scatter a photon from any of the laser beams and feels no net force. This velocity-dependent friction force is analogous to moving through molasses. The theoretical lower-limit of this effect is the recoil limit, which is the temperature associated with the momentum transferred by absorption and

emission of a single photon. In practice it is possible to get very close to this limit, for example the recoil limit for rubidium is about 0.4 µK, and [23] reports a measured temperature of 1.5 µK in a rubidium fountain clock.

As the sub-Doppler cooling mechanism effectively relies on the Zeeman effect to function, this technique is very sensitive to external magnetic fields. For cooling to function well external fields must be compensated or blocked. The optimal laser detuning depends on many experimental parameters, but is usually 5-10 transition linewidths red of resonance. The process typically takes a few tens of milliseconds. Sub-Doppler cooling necessarily reduces the density of the atomic ensemble, as the atoms are free to diffuse (albeit slowly).

2.4 Magneto-optical trapping

Doppler cooling and optical molasses serve to slow down atoms, but on their own these two effects do not actually trap atoms as there is no "restoring" force to confine the atoms. In 1987 E. L. Raab *et al* published a paper describing a technique of combining optical cooling with spatially-dependent magnetic fields to create an optical trap [24]. This technique became known as a magneto-optical trap (MOT). MOTs are now routinely used to trap atoms directly from room-temperature vapour, and can typically trap 10^7 - 10^8 atoms at densities around $10^{11}\,\mathrm{cm}^{-3}$. MOTs are dynamic: Every trapped atom is constantly absorbing and re-emitting light which limits the maximum density and minimum temperature through a self-heating effect. Every atom emits light which heats surrounding atoms (also known as multiple scattering, see e.g. [25]).

A MOT consists of three orthogonal pairs of counter-propagating laser beams and two magnetic field coils, as shown in Fig. 2.1. The basic idea of the MOT is to use magnetic fields to create a position-dependent force from the lasers such that atoms inside the trap are always pushed towards the centre. The magnetic field coils are in the anti-Helmholtz configuration, creating a quadrupole field: i.e. a magnetic field that is zero in the centre, and varies linearly in every direction away from the centre (for small distances). The lasers are all red-detuned from an atomic resonance, such that an atom exactly in the centre interacts as little as possible with any of the lasers, but if it atom strays from the centre, the magnetic causes a Zeeman shift of the atomic energy levels such that the atom starts to feel a force mostly from the laser beam which pushes it back to the centre of the trap.

The optimum detuning for a MOT comparable to that used in Doppler cooling, about 2-3 linewidths red of atomic resonance.

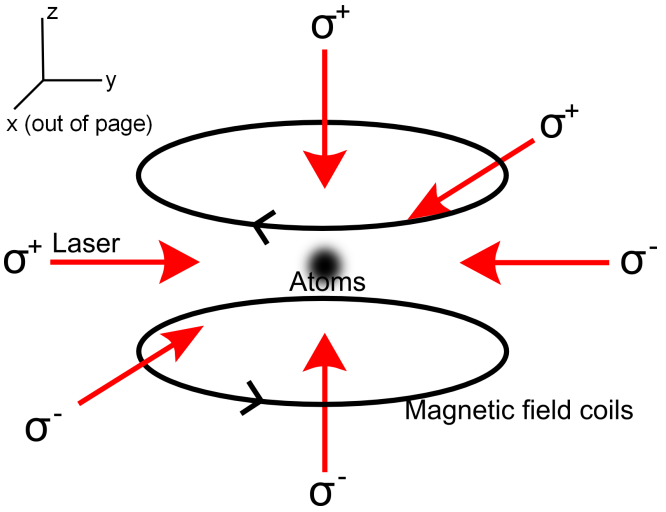

Figure 2.1. Magnetic field and laser beam configuration for a magneto-optical trap. The arrows on the coils show the direction of electric current. The $\sigma^{+(-)}$ indicates left (right) circularly polarised light respectively. Image from [26].

2.5 Temperature measurements

The most common method for measuring temperatures of clouds of cold atoms is the "time-of-flight" method, which is simply measuring the size of the cloud after turning off all potentials to measure the expansion rate. It can be shown (e.g. [26]) that a thermal cloud of gas at temperature T expanding in free space has density

$$n(x,t) = \frac{A\nu_0^3\pi}{\sqrt{r_0^2 + t^2\nu_0^2}} \exp\left(-\frac{x^2}{r_0^2 + t^2\nu_0^2}\right), \tag{2.3}$$

where $\nu_0 = \sqrt{\frac{2kT}{m}}$ is the most probable velocity, $A = \left(\frac{m}{2\pi kT}\right)^{3/2}$, and r_0 is the $1/e$-width at $t = 0$. Note that this is valid for each direction. In principle the temperature can be different in different directions but usually in a MOT all directions have the same temperature. Measuring the temperature then involves taking a series of photos of the cloud at a range of times t, and fitting a straight line to a plot of r^2, where r is the $1/e$-width of the cloud, vs t^2. The gradient of this line is then ν_0^2.

2.6 Production of cold atoms

Conveniently, the laser polarisations required to make a MOT are identical to those required to perform the $\sigma^+ - \sigma^-$ polarisation-gradient cooling described above. However a MOT requires a strong magnetic field gradient, which interferes with the sub-Doppler cooling mechanism described above. Production of samples of cold atoms is thus usually performed in a timed sequence: The magnetic field is switched on and the six trapping lasers are tuned to the optimum MOT frequency, typically 2-3 linewidths red of resonance. The MOT loads from background vapour until the desired number of trapped atoms is reached, which is usually on the order of 1-10 seconds depending on the experiment. The magnetic field is then quickly switched off and the lasers are detuned further from resonance before the atoms have time to move from the centre of the trapping beams, to perform the sub-Doppler cooling.

Many of the applications of cold atoms mentioned in the introduction require colder temperatures and/or higher densities than what is possible with a MOT, and many dramatic quantum effects are only observable at higher densities. Additionally, in a MOT the atoms are constantly subject to resonant interactions with the trapping light, which strongly influences behaviour. For these reasons, a MOT and sub-Doppler cooling are often used as the preparation steps to load atoms into a conservative minimally-interacting potential such as a magnetic trap, an optical dipole trap, or an optical lattice.

Optical dipole traps are discussed in detail in Chapter 4. Although a magnetic trap was used in the preparation of the experiments described in Chapter 7, magnetic traps are otherwise not directly relevant to results discussed in this thesis and so I will not discuss them in any detail. Magnetic traps have played an important role in the development of the field of ultracold gases, the first observation of magnetically trapped atoms was reported in 1985 [27]. Nowadays they are important for miniature "chip-based" atom traps, see e.g. [28]. While not talking about traps directly, the interaction of atoms with magnetic fields is further discussed in Chapter 5.

Chapter 3

Absorption imaging of cold atoms

3.1 Introduction

An important measurement in experimental atomic physics is determining the atomic spatial distribution. This is typically done using a CCD camera and a "probe beam". The camera is used to measure the absorption of the probe beam by the atomic cloud, which can be converted to atomic column density. This can be done fast and accurately: a typical measurement takes a few tens of microseconds and can reach near-single-atom resolution, e.g. [29] reports a resolution of ± 3.7 atoms in a cloud of about 300. Absorption imaging of a single ion was reported in [30][1], and single-atom absorption of a probe beam was reported in [31]. Fluorescence imaging can reach even more impressive accuracy, for example [32] reports single-atom resolution in clouds of up to 1200 atoms. However for quantitative measurements of large, dense clouds of atoms fluorescence imaging fails due to self-absorption by the cloud [33].

This chapter explains how absorption imaging is used to measure atomic clouds: Firstly I derive an equation used to quantify the number of atoms by measuring absorption of a probe beam. Then an algorithmic technique is described which is used to reduce noise in absorption images (not invented by us, but found in [34]).

[1] The title of this paper is "Absorption imaging of a single atom", while the article actually reports absorption imaging of a single ion, which comes with significantly different technical challenges from imaging neutral atoms.

3.2 Absorption imaging

The photon scattering rate R_{sc} of a two-level atom in a laser beam is given by [20, 35]

$$R_{sc} = \frac{\Gamma}{2} \frac{I/I_0}{1 + I/I_0 + 4\left(\frac{\Delta}{\Gamma}\right)^2} \tag{3.1}$$

where Γ is the natural linewidth, $I = I(x, y, z)$ is the light intensity, I_0 is the saturation intensity, and Δ is the detuning of the light from resonance.

The rate of change of intensity of a laser beam (the probe beam) propagating in the z-direction through an atomic cloud with density $n = n(x, y, z)$ is then

$$\frac{dI}{dz} = -n\hbar\omega R_{sc} \tag{3.2}$$

where $\omega = 2\pi c/\lambda$ is the angular frequency of the probe beam. For on-resonance light ($\Delta = 0$) this becomes

$$\frac{dI}{dz} = -\sigma_0 \frac{I}{1 + I/I_0} n \tag{3.3}$$

where $\sigma_0 = 3\lambda^2/2\pi$ is the absorption cross-section [33, 35]. This equation can be solved by separation of variables

$$\int \frac{1}{I} + \frac{1}{I_0} dI = -\sigma_0 \int n(x, y, z) dz. \tag{3.4}$$

The limits of the integration can be defined by the size of the atomic cloud. If we assume it's localised, then we just need to integrate over the cloud, rather than to $\pm\infty$. We also assume that the input probe beam is an infinite plane wave, and that there are no lensing effects from the atomic cloud, which is the case with on-resonant light. I indicate "initial" and "final" positions before and after the atomic cloud with the subscripts i and f, respectively. In practice, I_f and I_i are measured at the same position, but with and without the atomic cloud, respectively. I call I_f the "absorption image", and I_i the "background image". With these limits Eq. (3.4) can be solved as

$$\begin{aligned} \left(\ln(I) + \frac{I}{I_0}\right)\Bigg|_{I_i}^{I_f} &= -\sigma_0 n(x, y) \\ -\ln\left(\frac{I_f}{I_i}\right) + \frac{I_i - I_f}{I_0} &= \sigma_0 n(x, y) \end{aligned} \tag{3.5}$$

giving an equation relating the atomic column density $n(x, y) = \int n(x, y, z) dz$ with the two measured images of the probe beam.

The background image I_i needs to be measured without any atoms visible in the field of view. To reduce noise as much as possible the absorption and background images are typically measured one after the other as fast as possible. The longer the time between the images the more likely it is for mechanical vibrations, etc, to affect the probe beam, which is preferably identical in both of the images. As the absorption image is measured first, the atoms need to be removed or made invisible for the background image. This needs to be done quickly as the time between images is typically hundreds to thousands of microseconds. In the experiments I worked on during my PhD we used two techniques to make the atoms invisible after the absorption image. In the Barcelona experiment we excited the atoms on the $F = 2 \rightarrow F' = 2$ transition, which depumped all of them to the $F = 1$ ground state within a few hundred microseconds, making them invisible to the probe beam which was resonant with the $F = 2 \rightarrow F' = 3$ transition. We could not use the probe beam at a different frequency as this would move the position of fringes in the probe beam, and so the position of fringes in the two images would no longer match. The Florence experiment was able to quickly apply large magnetic fields, which were used to move the resonances of the atoms to be far away from the probe beam frequency.

In reference [36], the authors show that it is beneficial to use σ_0/α in place of the "ideal" $\sigma_0 = 3\lambda^2/2\pi$, where α is a unitless parameter that accounts for imperfections in the measurement such as imperfect probe polarisation, non-idealities resulting from having a multi-level atom, etc. α must be characterised, which can be done by measuring n for different intensities of the probe beam, then choosing the α which minimises the variation of n as a function of input light intensity.

Any imaging system also has noise. A major noise contributor for the CCD cameras typically used in this measurement is dark noise, which can be characterised and the mean can be subtracted to reduce the effect of hot pixels or any other inhomogeneity across the area of the CCD. Taking an image with no atoms or probe beam results in a dark noise image I_d. Including I_d and the α parameter the atomic column density can then be written as

$$n(x, y) = \frac{\alpha}{\sigma_0} \left[\ln\left(\frac{I_i - I_d}{I_f - I_d} \right) + \frac{I_i - I_f}{I_0} \right] \tag{3.6}$$

Figure 3.1 shows an example of absorption image processing with Eq. (3.6). (a) and (b) show $I_i - I_d$ and $I_f - I_d$, respectively. (c) shows the processed result.

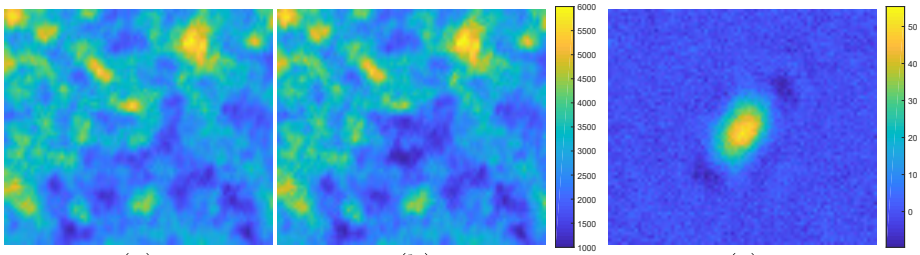

(a) (b) (c)

Figure 3.1. Example of absorption image processing. (a) shows an example of I_i, the light distribution without atoms. (b) shows I_f, the light distribution after absorption by a cloud of atoms. The colour bar shows the number of photon counts per pixel. (c) shows the result of processing the two images using Eq. (3.6). The colour bar shows the column density, i.e. number of atoms per pixel. The total number of atoms in this image is about 8000.

3.3 Noise reduction with an optimised background image

The wavefront of the probe laser is typically far from flat, which in principle should not be a problem because the absorption imaging signal depends only on the difference between the absorption image and the background image. However, due to mechanical instability and light intensity drifts, there can often be a small difference in the light intensity distribution between the two images, resulting in a "fringing" effect such as that seen on the left-hand side of Fig. 3.2. To combat this, we use an algorithmic technique to produce an optimised background image for a given absorption image, from a library of background images. This reduces the fringing effect and can also reduce the contribution of shot noise. The technique was first published in [34] but originates from a group at the University of Hamburg [37] [38].

Given a set of reference background images R_k, we choose coefficients c_k to generate the background image Q, which can be used in place of I_i in Eq. (3.6):

$$Q = \sum_k c_k R_k \tag{3.7}$$

For each absorption image A, we find the best possible background image by choosing c_k to minimise the least-squares difference E between A and Q *outside*

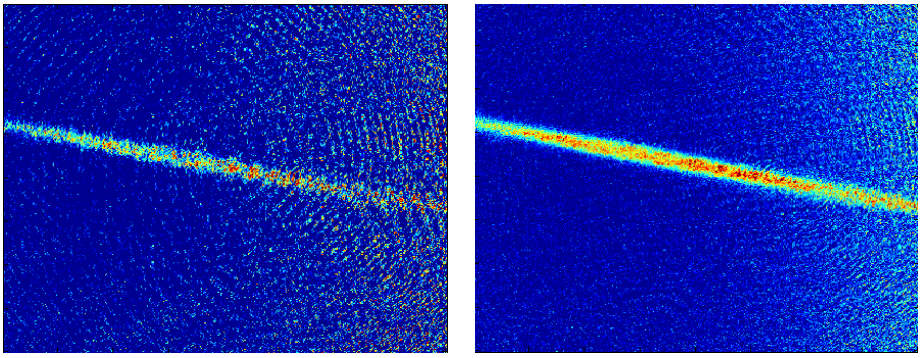

Figure 3.2. The left-hand image shows an absorption image processed with a single background image. The right-hand image shows an absorption image processed with the optimised background generated from 50 other background images. The left image shows increased shot noise and distortion from fringes. The two images have the same colour scale.

of the signal region. The signal region is "where the atoms are", and needs to be manually defined.

$$E = \sum_x m_x (A_x - Q_x)^2 \tag{3.8}$$

where $m = 1$ outside the signal region, $m = 0$ inside the signal region, and x is pixel index, assuming the images have been arranged into column vectors.

To minimise E we first take the partial derivative with respect to c_j and set the result to zero.

$$\frac{\partial E}{\partial c_j} = 2 \sum_x (A_x - \sum_k c_k R_{x,k}) R_{x,j} = 0 \tag{3.9}$$

If we let

$$B_{j,k} = \sum_x m_x R_{x,j} R_{x,k} \tag{3.10}$$

we then have

$$\sum_k c_k B_{j,k} = \sum_x m_x A_x R_{x,j}, \tag{3.11}$$

so we can easily find coefficients **c** by inverting the square matrix B. Note that B is symmetric so only half the elements actually need to be calculated.

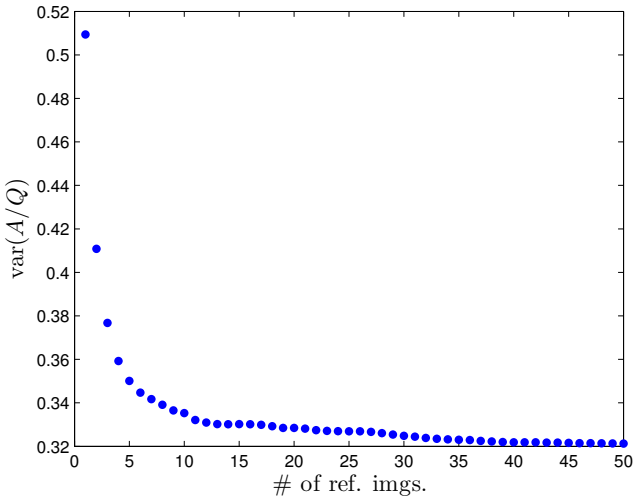

Figure 3.3. Variance of A/Q as a function of the number of images used to generate Q.

To quantify the noise reduction, Fig. 3.3 shows the variance of A/Q outside of the signal region for different numbers of background images. As well as reducing the effect of moving fringes, this technique also reduces the contribution of shot noise to noise in the processed image. Because the background image is now an averaged image, the contribution of random shot noise is reduced.

3.3.1 Additional noise-reduction techniques

Reference [29] discusses how careful selection of the "region of interest" in an absorption image can significantly reduce noise in the integrated atom number. In this paper they have an elliptically-shaped atomic cloud, and can halve the noise contribution by using an elliptically-shaped integration region instead of the usual rectangular one. Also in this paper is discussion of how compensation of pushing of the atomic cloud by the probe beam can reduce uncertainty in the measurement of total atom number, although this is more relevant in imaging systems with a large numerical aperture (NA) and consequently small depth-of-field, such as that in the experiment in Florence (which has a imaging system with an NA of about 0.47, while the experiment in Barcelona has an imaging system with an NA of 0.14).

Chapter 4

Optical dipole traps

Both of the experiments I worked on during my PhD largely depended on optical dipole traps (ODTs) to prepare and hold ensembles of atoms for measurements. ODTs exploit the interaction of the atomic electric dipole moment with light to produce conservative traps which cause very little resonant excitation of the atoms, and can produce much denser and colder samples of atoms than what is possible with a MOT. ODTs can also hold atoms for long periods of time, as the lifetime of atoms in the trap is usually only limited by collisions with background gas. As such, atoms can be held for many tens of seconds in a high-vacuum well-isolated from the external environment[1]. In this section I will review the basic physics of ODTs, present experimental apparatuses and characterisation data, and discuss some applications.

The first atomic optical dipole trap was experimentally demonstrated by Steven Chu and team in 1986 [9], where they loaded 500 sodium atoms into a trap and observed them for several seconds. The invention of the MOT greatly improved loading capability, and now it is routine to observe many millions of atoms in an ODT. Under the right conditions ODTs provide a state-independent potential for atoms, making them an excellent substrate for *spinor* physics, the study of the complex interactions of many atoms in different internal states [39]. Two or more counter-propagating ODTs interfere to make a periodic potential known as an *optical lattice*, the backbone of the field of *quantum simulators*: For example, atoms in an optical lattice see a potential analogous to that seen by electrons moving in a crystalline solid, and it is hoped that this will lead to, for example,

[1] For example in the Florence experiment the $1/e$-lifetime of atoms in the dipole trap in the science cell is over 80 seconds. In the Barcelona experiment we were limited to a lifetime of about 5-10 seconds due to higher background vapour pressure.

insights in the understanding of the mechanism of high-temperature superconductivity [40]. Optical lattices are also crucial for modern optical atomic clocks [41].

4.1 Basic physics

Here I derive some of the fundamental properties of ODTs, illustrated using data from the Barcelona experiment. Note that much of this section has been adapted from [42].

4.1.1 Optical dipole potential and scattering rate

Atoms are polarisable particles, so placing an atom in an oscillating electric field described by

$$\mathbf{E}(\mathbf{r},t) = \mathcal{E}(\mathbf{r})\exp(-\mathrm{i}\omega t)\hat{\mathbf{n}} + c.c. \tag{4.1}$$

induces an oscillating dipole moment in the atom given by

$$\mathbf{p}(\mathbf{r},t) = p(\mathbf{r})\exp(-\mathrm{i}\omega t)\hat{\mathbf{n}} + c.c. \tag{4.2}$$

where $\hat{\mathbf{n}}$ is the polarisation vector. The amplitude p of the polarisation is related to the amplitude $\mathcal{E}$ of the electric field by

$$p = \alpha\mathcal{E} \tag{4.3}$$

where α is the complex atomic polarisability which is generally a complex function of the properties of the applied light and of the atom (Chapter 5 is largely devoted to accurate calculation of this value). However, if we make some approximations - that there is a single electric-dipole transition from the atomic ground state, and we have a classical light field which is far-detuned from resonance - we can write α using a simple formula:

$$\alpha = 6\pi\epsilon_0 c^3 \frac{\Gamma/\omega_0^3}{\omega_0^3 - \omega^3 - \mathrm{i}(\omega^3/\omega_0^3)\Gamma} \tag{4.4}$$

where ϵ_0 is the permittivity of free space, c is the speed of light, ω_0 is the atomic transition frequency, ω is the laser angular frequency, and Γ is the natural linewidth of the transition.

The oscillating electric field creates a potential for the induced dipole, which can be calculated as

$$U_{\mathrm{dip}} = -\frac{1}{2}\langle \mathbf{pE}\rangle = -\frac{1}{2\epsilon_0 c}\mathrm{Re}(\alpha)I(\mathbf{r}) \tag{4.5}$$

where the angular brackets indicate the time-average and $I = 2\epsilon_0 c|\mathcal{E}|^2$ is the light intensity.

Another quantity of interest is the scattering rate. The atom is a damped oscillator, so it absorbs energy from the light and re-emits it as dipole radiation. The power absorbed is given by

$$P_{\text{abs}} = \langle \dot{\mathbf{p}}\mathbf{E} \rangle = 2\omega \ \text{Im}(p\mathcal{E}^*) = \frac{\omega}{\epsilon_0 c}\text{Im}(\alpha) I(\mathbf{r}) \tag{4.6}$$

This can be converted to a scattering rate by dividing by the energy of a single photon

$$\Gamma_{\text{sc}} = \frac{P_{\text{abs}}}{\hbar\omega} = \frac{1}{\hbar\epsilon_0 c}\text{Im}(\alpha) I(\mathbf{r}) \tag{4.7}$$

Substituting eq. (4.4) into eqs. (4.5) and (4.7) gives

$$\begin{aligned} U_{\text{dip}}(\mathbf{r}) &= -\frac{3\pi c^2}{2\omega_0^3}\left(\frac{\Gamma}{\omega_0 - \omega} + \frac{\Gamma}{\omega_0 + \omega}\right) I(\mathbf{r}) \\ \Gamma_{\text{sc}}(\mathbf{r}) &= \frac{3\pi c^2}{2\omega_0^3}\left(\frac{\omega}{\omega_0}\right)^3 \left(\frac{\Gamma}{\omega_0 - \omega} + \frac{\Gamma}{\omega_0 + \omega}\right)^2 I(\mathbf{r}). \end{aligned} \tag{4.8}$$

We define the detuning Δ as $\Delta = \omega_0 - \omega$. In the case where $|\Delta| \ll \omega_0$, we can make the rotating-wave approximation, and eqs. (4.8) become

$$\begin{aligned} U_{\text{dip}}(\mathbf{r}) &= -\frac{3\pi c^2}{2\omega_0^3}\frac{\Gamma}{\Delta} I(\mathbf{r}) \\ \Gamma_{\text{sc}}(\mathbf{r}) &= \frac{3\pi c^2}{2\omega_0^3}\left(\frac{\Gamma}{\Delta}\right)^2 I(\mathbf{r}), \end{aligned} \tag{4.9}$$

which illustrate two important points about ODTs:

1) Red-detuned light (i.e. $\Delta > 0$) makes a negative potential for the ground state, so atoms are attracted to regions of high-intensity, while blue-detuned light does the opposite.

2) The potential is proportional to I/Δ, while the scattering rate is proportional to I/Δ^2. Thus for the maximum ratio of trap depth to scattering rate, ODTs typically employ high-intensity far-detuned light.

4.1.2 Trap geometry and depth

An ODT can be made with a single focussed Gaussian laser beam. In this case, the light intensity as a function of position is, in cylindrical coordinates:

$$I(r, z) = \frac{2P}{\pi w^2(z)} \exp\left(-2\frac{r^2}{w^2(z)}\right) \tag{4.10}$$

where P is the total optical power in the beam, and

$$w(z) = w_0 \sqrt{1 + \left(\frac{z}{z_R}\right)^2} \tag{4.11}$$

where $w(z)$ is the $1/e^2$ beam radius, and $z_R = \pi w_0^2/\lambda$ is the Rayleigh range. In this configuration the confining force is much stronger in the radial direction than the longitudinal direction, so at equilibrium the density distribution of a cloud of trapped atoms forms a cigar shape (e.g. see Fig. 4.1a).

If the cloud of trapped atoms has a thermal energy $k_B T$ much less than the trap depth and the longitudinal distribution is less than the Rayleigh range z_R, where T is the temperature of the ensemble and k_B is Boltzmann's constant, we can approximate the trap potential by expanding eq. 4.10 in a power series and taking the first two terms:

$$U(r, z) \approx U_0 \left(2 \left(\frac{r}{w_0}\right)^2 + \left(\frac{z}{z_R}\right)^2 - 1 \right), \tag{4.12}$$

so $-U_0$ is the potential at the centre of the trap.

Particles trapped in a parabolic potential undergo harmonic oscillations. The frequency of oscillation can be calculated by equating the potential energy of a harmonic oscillator $U(x) = \frac{1}{2} m\omega^2 x^2$ with eq. 4.12 at the positions $(r, 0)$ and $(0, z)$. The oscillation frequencies in the radial and longitudinal directions are given by

$$\begin{aligned} \omega_r &= \sqrt{\frac{4U_0}{m w_0^2}} \\ \omega_z &= \sqrt{\frac{2U_0}{m z_R^2}} \end{aligned} \tag{4.13}$$

where m is the mass of the trapped atom species. So by knowing the waist w_0 of our trapping beam, which can be determined from the optics used in the experiment, we can measure the trap oscillation frequencies to find out the depth of the trap. Figure 4.1 shows an example of radial trap oscillations from the Barcelona experiment.

4.2 Light-shift tomography

An unavoidable consequence of trapping atoms with light is that the light interacts with the energy levels of the atoms, inducing level shifts known as ac

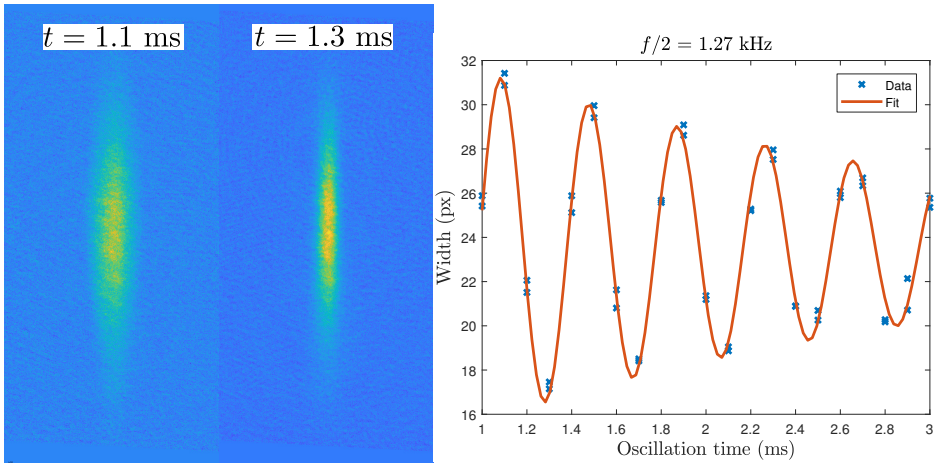

(a) (b)

Figure 4.1. Radial trap oscillations of ^{87}Rb atoms in a single focussed-beam dipole trap at 1560.492 nm. The trapped atoms are excited by switching the trap off and on again within 100 µs, inducing "breathing mode" oscillations at twice the trap frequency. (a) shows two 10 ms time-of-flight images after the oscillation time shown in each respective label. The width of the cloud is measured near the centre as a function of oscillation time. (b) shows the width as a function of oscillation time, and a fit with an exponentially decaying sinusoid function to get the oscillation frequency given at the top of the figure.

Stark shifts or light shifts. This is of course the very mechanism that traps the atoms in the first place: if the trapping light is sufficiently far-detuned such that excitation is negligible, the spatially-dependent light shift of the ground state is identical to the trapping potential. In general, every level experiences a shift due to the light field but the polarisability of each level is different, meaning the light shift of each level is different. This differential light shift means the transition frequencies become dependent on the local light intensity, an effect which can be used to characterise the ODT.

Figure 4.2 shows the effect of a differential light shift on an atom in a Gaussian ODT. The diagram is representative of the shift experienced by the D_2 transition in ^{87}Rb in an ODT at 1560.492 nm: both the excited and ground states experience a negative shift, but the excited state shift is much larger (in this specific case $\alpha_e/\alpha_g \approx 50$, Chapter 5 discusses how to calculate this value).

4.2.1 Transition frequency shift due to differential light shift

The actual transition frequency shift as a function of light intensity can be calculated as follows: Consider an atomic transition with polarisability of the ground state α_g and polarisability of the excited state α_e, in a Gaussian optical potential $I(r)$. Fig. 4.2 shows that the light shift of the transition is $\Delta(r) \propto (\alpha_g - \alpha_e)I(r)$. Given that $U(r) \propto -\alpha_g I(r)$, we can write

$$\hbar\Delta = \left(\frac{\alpha_e}{\alpha_g} - 1\right) U(r). \tag{4.14}$$

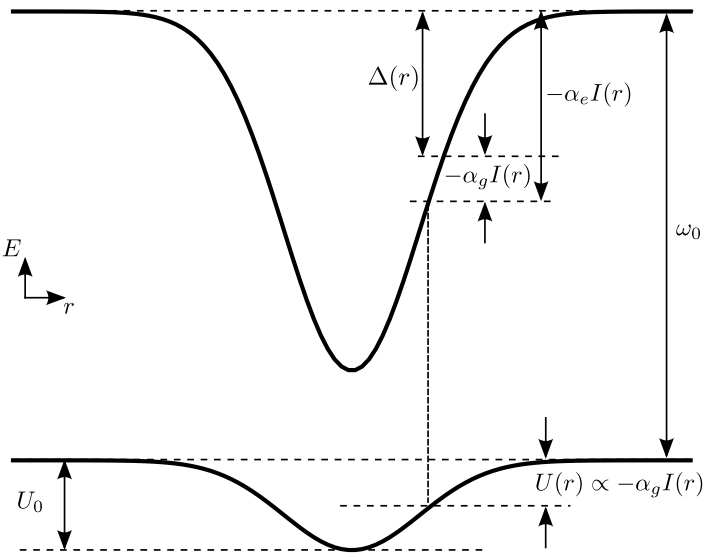

Figure 4.2. Energy level shifts of an atomic transition of an atom in a Gaussian potential. Each level has a different polarisability α, resulting in a position-dependent shift of the transition frequency.

4.2.2 Tomography of an ODT with a homogeneous distribution of atoms

Here I'll describe a technique for using differential light shift to map out an optical potential. First described in [43], where it is used to extract information about

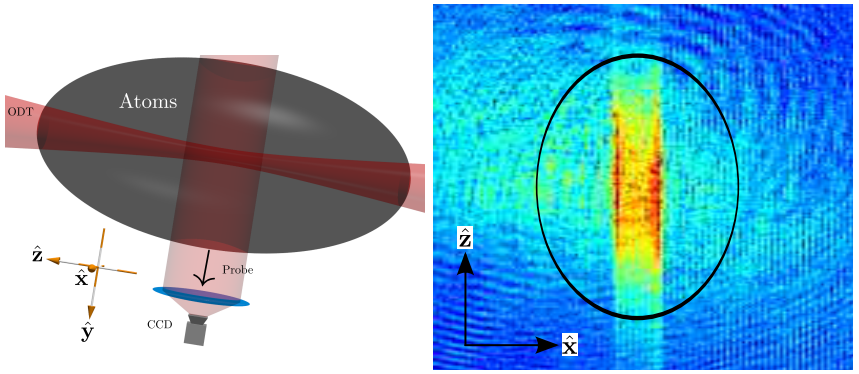

(a) (b)

Figure 4.3. (a) Experiment geometry for using light shifts to measure the size of the optical potential. The atom cloud is approximately homogeneous across the ODT, so variation in the signal on the CCD comes from the induced light shifts. The system has translational symmetry along the z-axis over the area of the probe beam. (b) Typical absorption data from this measurement. The area inside the black circle has approximately homogeneous atom density.

the temperature of the atoms and depth of the trap, here I also use it to extract data about the size of the dipole trap, as is described in [44].

Consider the cylindrically-symmetric system shown in Fig. 4.3a: a single focused Gaussian laser beam propagating through a large cloud of cooled atoms. The atom cloud is approximately homogeneous across the waist of the laser beam. A probe beam projects the atomic absorption onto the CCD camera, which can be measured as a function of frequency of the probe beam. Atoms in the path of the focused beam experience a light shift depending on the intensity of the the beam, which is seen as a position-dependent absorption of the probe beam. A typical absorption image from this system is shown in Fig. 4.3b.

The apparent number of atoms at a given position $\mathbf{r}$ and probe detuning δ is given by[2]

$$N(\mathbf{r}, \delta) = n(\mathbf{r})\sigma(\mathbf{r}, \delta), \tag{4.15}$$

[2]I'm using this strange notation so that a later result can be compared to an equation in reference [43]. Instead of "apparent number of atoms" one would normally discuss absorption of a probe beam.

where $\sigma(\mathbf{r}, \delta)$ is the absorption cross-section of a single atom normalised such that the on-resonance cross-section is 1, and $n(\mathbf{r})$ is the atomic density. $\delta = (\omega - \omega_0)/\Gamma$ is the normalised detuning of the laser from the free-space transition frequency $\omega_0 = 2\pi c/\lambda$. In the low-intensity limit, the normalised σ of a single two-level atom with a transition with linewidth Γ is

$$\sigma(\delta) = \frac{1}{1 + 4(\delta - \Delta(\mathbf{r})/\Gamma)^2}, \tag{4.16}$$

In cylindrical coordinates, the light shift $\Delta(\mathbf{r})$ shown in Fig. 4.3a is only a function of r, and the potential is Gaussian, so Δ can be written as

$$\Delta(r) = \frac{U_0}{\hbar}\left(\frac{\alpha_e}{\alpha_g} - 1\right) e^{-2r^2/w_0^2} \tag{4.17}$$

where w_0 is the $1/e^2$ waist of the ODT. The signal on the camera is then the projection of Eq. 4.15 onto the $x - z$ plane with $n(\mathbf{r}) = n_0$:

$$N(x, \delta) = n_0 \int_{-\infty}^{\infty} \left[1 + 4\left(\delta - Ae^{-2(x^2+y^2)/w_0^2}\right)^2\right]^{-1} dy \tag{4.18}$$

giving the 'Batman' signal shown in Fig. 4.4a. Here $A = (U_0/\hbar\Gamma)(\alpha_e/\alpha_g - 1)$. The absorption signals at different detunings can be fitted collectively to find a value for w_0, the waist of the ODT (Fig. 4.4b). Note that this measurement is done *in-situ*, so can be useful for diagnosing imperfections in the ODT introduced by windows, optics, etc. Also, while the tomography is done here for a Gaussian potential, it has been demonstrated for mapping the modes of a cavity [44], and could be used for a more complicated potential created with e.g. a spatial light modulator [45].

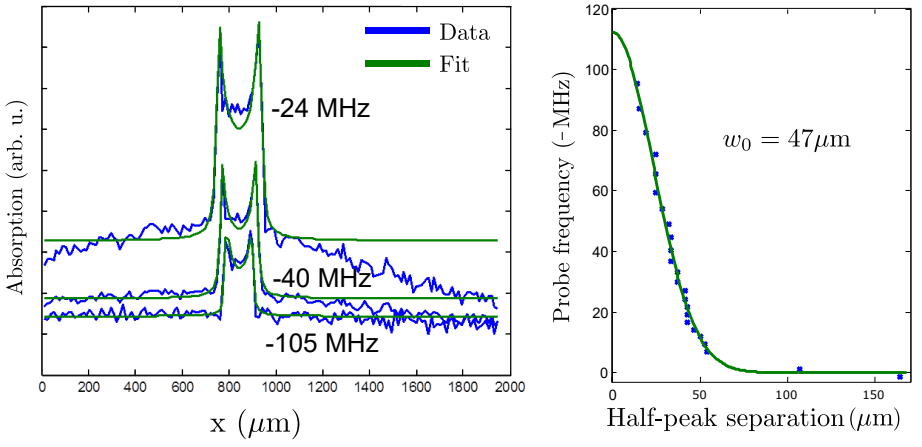

Figure 4.4. (a) 'Batman' signal created by projecting a cylinder of absorption on to the flat plane of a camera for different laser detunings. (b) Fitting the peak separation of many 'Batmen' to a Gaussian function can be used to measure w_0 of an ODT *in-situ*. Here the measurement gives 47 µm, which is very close to the 45 µm we expected from the optics used in this system. Note that the data in (b) was measured at a lower optical power than the data in (a).

4.2.3 Tomography of a thermalised gas in a harmonic potential

Rather than using a homogeneous atom cloud to probe the optical potential, it is also possible to use differential light shifts to probe the distribution of atoms trapped inside the dipole trap. This can give information on the trap depth and the cloud temperature. In this section I first of all re-derive a result from reference [43], which describes the number of atoms measured vs trap depth in a harmonic potential. There appears to be a small mistake in the published equation, which is rectified here. This equation is then used to extract information about the ODT used in the Barcelona experiment.

We want to find $N(\delta)$, the total number of atoms as a function of detuning of the probe beam, for a distribution of atoms trapped in an ODT. For this derivation assume we have a spherically symmetric Gaussian potential, so we integrate

Eq. 4.15 over all space, shown here in Cartesian and spherical coordinates:

$$N(\delta) = \int d^3\mathbf{r}\; n(\mathbf{r})\sigma(\mathbf{r},\delta) = \int_0^\infty dr\; 4\pi r^2 n(r)\sigma(r,\delta). \tag{4.19}$$

We know the absorption cross section σ from Eq. 4.16, but here we make the approximation that the thermal energy of the atoms k_BT is much smaller than the trap depth U_0. In this case for the potential $U(r)$ we can use Eq. 4.12 with $z = 0$. So

$$U(r) = U_0\left(\frac{2r^2}{w_0^2} - 1\right). \tag{4.20}$$

The density $n(\mathbf{r})$ of a gas at thermal equilibrium in a conservative potential $U(\mathbf{r})$ is given by [46]

$$n(\mathbf{r}) = n_0 e^{-U(\mathbf{r})/k_BT}, \tag{4.21}$$

where n_0 is the density at $U(\mathbf{r}) = 0$. We can find n_0 by equating the integral of the density with the total number of trapped atoms

$$\begin{aligned} N_{tot} &= \int_0^\infty 4\pi r^2 n_0 e^{-U(r)/k_BT} dr \\ &= \int_0^\infty 4\pi r^2 n_0 e^{-U_0(2r^2/w_0^2-1)/k_BT} dr \\ &= 4\pi n_0 e^{U_0/k_BT} \int_0^\infty r^2 e^{-U_0(2r^2/w_0^2)/k_BT} dr. \end{aligned} \tag{4.22}$$

We make use of the identity

$$\int_0^\infty x^2 e^{-ax^2} dx = \frac{1}{4}\sqrt{\frac{\pi}{a^3}}, \tag{4.23}$$

to get

$$N_{tot} = n_0 e^{U_0/k_BT}\left(\frac{\pi w_0^2 k_B T}{2U_0}\right)^{3/2}. \tag{4.24}$$

The integral 4.19 now looks like

$$N(\delta) = \int_0^\infty dr\; n_0 e^{-U(r)/k_BT} \times \frac{1}{1 + 4(\delta - \Delta(r)/\Gamma)^2} \times 4\pi r^2 \tag{4.25}$$

To solve eq. (4.25), we make the substitution $u^2 = \frac{2U_0}{w_0^2}\frac{r^2}{k_BT}$, so that

$$\Delta(r) = \frac{U(r)}{\hbar}\left(\frac{\alpha_e}{\alpha_g} - 1\right) = \frac{(u^2 k_B T - U_0)}{\hbar}\left(\frac{\alpha_e}{\alpha_g} - 1\right). \tag{4.26}$$

Substituting,

$$N(\delta) = 4\pi n_0 e^{U_0/k_B T} \left(\frac{w_0^2 k_B T}{2U_0}\right)^{3/2} \times \int_0^\infty u^2 e^{-u^2} \frac{du}{1 + 4[\delta + (U_0 - u^2 k_B T)(\alpha_e/\alpha_g - 1)/\hbar\Gamma]^2} \tag{4.27}$$

$$= \frac{4N_{tot}}{\sqrt{\pi}} \int_0^\infty \frac{u^2 e^{-u^2} du}{1 + 4(\delta + \nu - tu^2)^2}.$$

Where $\nu = \frac{U_0}{\hbar\Gamma}\left(\frac{\alpha_e}{\alpha_g} - 1\right)$ and $t = \frac{k_B T}{\hbar\Gamma}\left(\frac{\alpha_e}{\alpha_g} - 1\right)$. Note the extra "$-1$" factor in the definition of ν compared to [43].

Figure 4.5 shows one experiment geometry we used to perform tomography on a loaded ODT. The probe beam is co-propagating with the dipole trap beam when they pass through the atoms, and then the two are separated with a dichroic mirror sending the probe beam towards the camera. Fig. 4.6 shows some example results of measuring absorption of the probe beam by the atom cloud vs. frequency. The extracted values of U_0 and T agree reasonably well with those obtained from trap frequency measurements and time-of-flight measurements. However, one can see that the fit does not match the data well, especially near the peak. The reason for this is that this equation neglects the multi-level structure of the atom, something which is discussed in detail in Chapters 5 and 6.

4.3 Optical Bose-Einstein condensation

My experiment in Barcelona was originally designed to be a system for studying magnetometry with Bose-Einstein condensates (BECs), a form of matter where all the constituent particles have the same spatial wavefunction. BEC magnetometry is not the focus of my thesis, however I contributed towards the construction of the experiment and BEC physics is relevant to my work in Florence. In this section I will briefly review BECs and show some results from our experiment.

The first BEC was obtained in a magnetic trap with a dilute vapour of ^{87}Rb atoms in 1995 [47]. We successfully obtained a BEC all-optically with the same species in August 2016. The typical path to creating a BEC starts with trapping an ensemble of atoms in some confining potential, usually a magnetic or optical trap. The confinement quantises the allowed energy levels of particles in the ensemble. At low enough temperatures, a macroscopic number of particles occupies

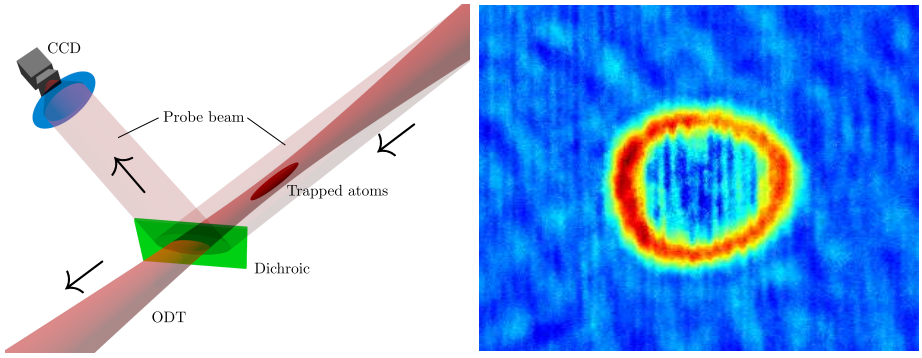

(a) (b)

Figure 4.5. (a) Experiment geometry used to perform tomography on a cloud of trapped atoms. (b) "Ring" of resonant atoms as a result of performing the measurement represented in (a),with the probe beam resonant with atoms halfway down the trap. The total absorption is obtained by integrating this entire image.

the lowest energy level available, creating the BEC. The formation condition of a BEC is usually defined as the point where the de Broglie wavelength of particles in the ensemble becomes larger than the inter-particle distance, such that the particles have to be described with a collective wavefunction. This condition can be quantified as

$$n\lambda_{dB}^3 > 2.612 \tag{4.28}$$

where n is the particle density, and λ_{dB} is the de Broglie wavelength (proportional to $1/\sqrt{T}$, see [48] for a derivation).

The trapped ensemble is usually cooled evaporatively (I say "usually" because I know of two experiments that have optically achieved BEC without evaporative cooling: [49] and [50]). In a magnetic trap this is usually done with the rf knife technique, while in an optical trap the only way is to reduce the depth of the potential, letting the hottest atoms escape while the remaining atoms thermalise at a lower temperature. It is challenging to achieve a BEC in an optical potential, as this final step of cooling requires relaxing the potential which reduces the particle density and collision rate.

A representation of the optical evaporation process is shown in Fig. 4.7. Atoms initially trapped in the ODT have a Maxwell-Boltzmann energy distribution. The light intensity is then reduced, reducing the depth of the potential. Higher-energy atoms escape while remaining atoms thermalise at a lower temperature. The rate

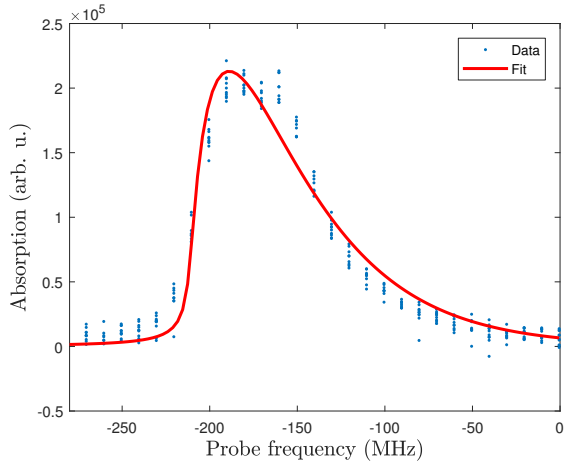

Figure 4.6. Absorption vs. probe frequency as a result of the measurement shown in Fig. 4.5. The values extracted by fitting Eq. 4.27, $U_0 = k_B \cdot 222\,\mu\text{K}$ and $T = 42\,\mu\text{K}$ agree well with complementary trap frequency and time-of-flight measurements.

of this thermalisation decreases as the trap depth decreases because the atomic oscillation frequency (and therefore collision rate) depends on the trap depth. With sufficiently high initial atom number, The transition to BEC is considered to occur when the ground state of the potential becomes macroscopically occupied. Even with an optimised evaporation procedure this typically involves throwing away more than 99% of the atoms trapped initially. Formation of a BEC has been shown to be a stimulated process, not a relaxation: once the BEC starts forming in a single energy level atoms preferentially scatter into that level, much like the gain mechanism in a laser [51].

Despite the technical challenge presented by the reducing collision rate, the first all-optical BEC was first obtained in 2001 by M. Barrett *et al.* [11]. It is interesting to note that BECs were successfully transferred into optical traps before this, e.g. [52]. There are many excellent articles on the physics of evaporation, for example see [53] for a review of the state-of-the-art in 1996, or [54] for a theoretical description of evaporation in an optical trap.

A BEC in an optical trap has the big advantage over magnetic traps that an optical potential can be state-independent. For example, the three $F = 1$ magnetic sublevels in the $5S_{1/2}$ ground state of ^{87}Rb in an ODT at 1560 nm have

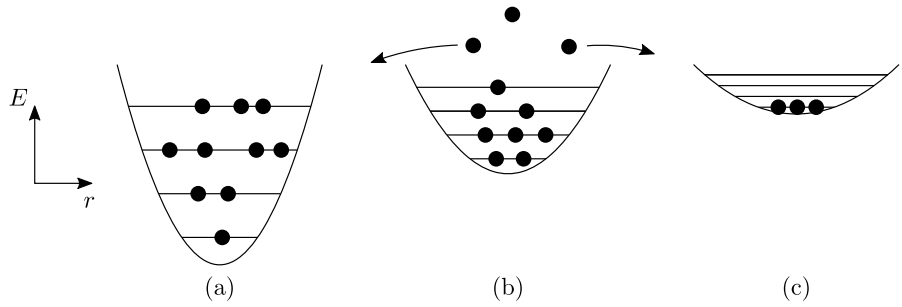

Figure 4.7. Representation of the optical evaporation process to reach BEC. (a) Atoms in an optical potential occupy discrete energy levels with a Maxwell-Boltzmann distribution. (b) Reducing the trap depth removes higher-energy atoms while remaining atoms thermalise at a lower temperature. (c) Eventually the only remaining atoms are in the same energy level.

the same polarisability, and therefore experience the same potential. This is necessary for applications such as optical magnetometry: in optical magnetometry magnetic fields are detected by measuring the precessing spin of the atoms, which is the same as measuring the time-dependent superposition of the atomic ground states. A magnetic trap can only trap a single ground state, so such precession is not possible. In any case for obvious reasons it would be impractical to measure magnetic fields with magnetically trapped atoms.

Figure 4.8 shows the geometry of the Barcelona BEC experiment. The BEC is formed at the crossing of two ~ 10 W ODTs at 1560.492 nm (for full details see the PhD thesis of Silvana Palacios [55]). Fig. 4.9 shows crossing the BEC transition by increasing evaporation time, with subsequent lowering of the potential depth. All of the images show an evaporatively cooled atomic cloud after a 16 ms time-of flight with the length of the evaporation given in the respective figure.

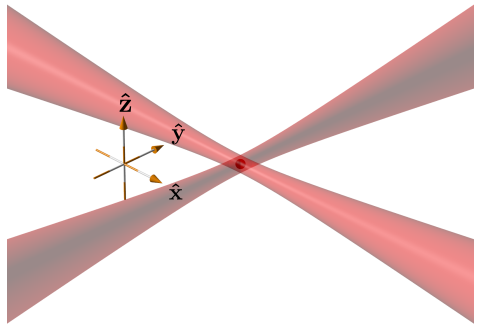

Figure 4.8. Geometry of ODTs in the Barcelona experiment: Two beams cross in the horizontal plane at a 90° angle and the atoms are trapped at the crossing. The two beams are not equal in power, so the trap frequencies are anisotropic. Imaging is done about 45° from the vertical axis.

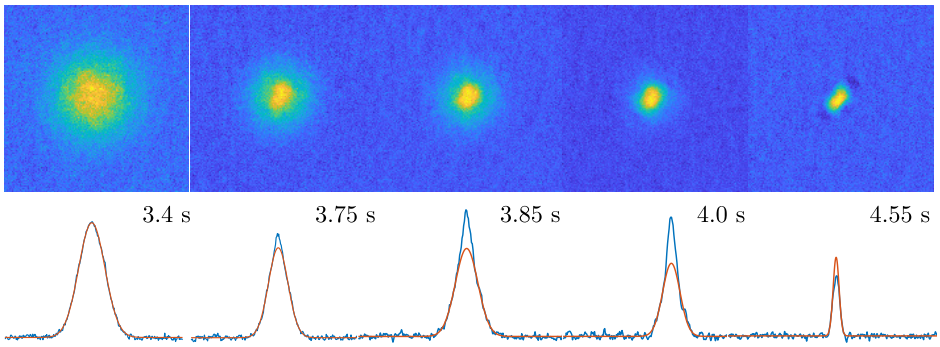

Figure 4.9. Absorption images after 16 ms time-of-flight for different evaporation times, showing the transition from a thermal ensemble to a BEC in the Barcelona experiment. The top row is absorption images, and the bottom row the same image integrated vertically. Blue lines are data, red lines are a Gaussian fit excluding the central third of the peak (i.e. fitting only data below the half-maximum). The first image is a fully thermal cloud, which is well-fit by a Gaussian. Then a sharp peak grows, showing an increasing condensed fraction. Finally a fully condensed cloud (no detectable thermal fraction) with a Thomas-Fermi density distribution has sharp edges, making the fit over-estimate the peak height in the centre. The final image also has a pronounced anisotropy, characteristic of a BEC released from an anisotropic trap.

4.4 Laser intensity control and noise-induced heating

4.4.1 Feedback control of laser intensity

Lasers, especially the high-powered ones used for dipole traps, tend to have intensity noise. If this noise is strong enough at twice the trap frequency it can parametrically heat atoms trapped in the laser and cause unnecessary atom loss. To control the intensity of the laser beam - which is necessary for controlled optical evaporation - and to reduce intensity noise I built a "noise-eater" feedback system for our ODT lasers. A schematic of this system is shown in Fig. 4.10.

The feedback system consists of a pure integrator, which was found to function sufficiently well in reducing noise and for dynamic control of the laser power. The actuator is an acousto-optic modulator (AOM), and the laser power is detected on a large-area photodiode (we used a Thorlabs PDA10CS-EC, with 0.8 mm^2 area and 17 MHz bandwidth). The entire laser wavefront needs to be focussed on the photodiode, with room to move, so that beam-pointing noise is not converted into intensity noise.

To characterise the feedback system, I measured the relative intensity noise $\epsilon(t)$ at the in-loop photodiode for a range of different conditions. $\epsilon(t)$ is defined as

$$\epsilon(t) = \frac{I(t) - I_0}{I_0} \tag{4.29}$$

where $I(t)$ is the signal as a function of time, and I_0 is the mean of the signal over the measurement period. Fig. 4.11 shows the power spectrum of $\epsilon(t)$ with the laser at full power without feedback, with the laser at full power with the feedback circuit closed, and finally with no laser power at all (to measure the electronic noise of the photodiode). The reduction in noise in the locked signal is significant for frequencies up to about 8 kHz. There is a peak in the electronic noise at 100 Hz, probably from the room lights despite the photodiode being covered by a bandpass filter with passband at the laser wavelength 1560 ± 10 nm. There is another significant peak in the free-running laser at about 2 kHz, which is reduced by over 20 dB by the feedback. The large peak in the locked spectrum at about 30 kHz shows the bandwidth of the feedback system, and is expected behaviour because an integrator "pushes" noise to higher frequencies. The noise due to shot noise was estimated from the power incident on the photodiode as

$$\epsilon_{sn} = \frac{2G^2 e S P_{opt}}{\langle V \rangle} \tag{4.30}$$

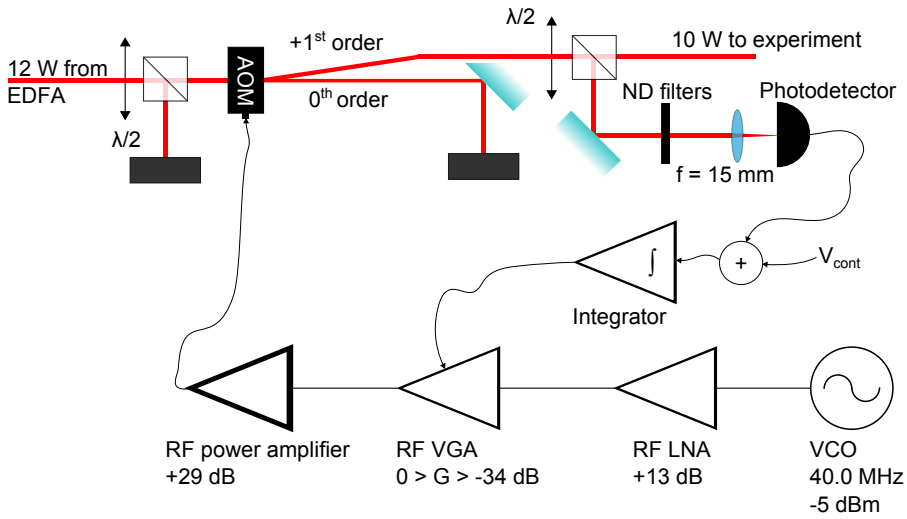

Figure 4.10. Noise-eater feedback system. The ODT intensity is controlled by an acousto-optic modulator (AOM). A small part of the diffracted beam is sent to a photodiode, which feeds an integrator controlling a variable-gain RF amplifier (VGA), which controls the amplitude of the AOM output. The integrator ensures the sum of the feedback signal from the photodiode and the control voltage (V_{cont}) is zero. LNA = Low-noise amplifier, VCO = Voltage-controlled oscillator, EDFA = Erbium-doped fibre amplifier.

where G is the gain of the photodiode transimpedence amplifier, e is the electronic charge, S is the sensitivity of the photodiode in A/W, P_{opt} is optical power incident on the photodiode, and $\langle V \rangle$ is the mean voltage of the signal due to the laser.

In hindsight, I should have measured with a photodiode outside of the feedback loop, i.e. directly measured the light in the beam going to the experiment. In Fig. 4.11 one can see that at low frequencies the electrical noise power is actually higher than the locked laser noise power. What is probably happening is that the feedback system is cancelling out the electrical noise in the photodiode signal by adding the opposite to the light intensity, which means that the data shown in Fig. 4.11 actually underestimates the noise power in the locked laser spectrum.

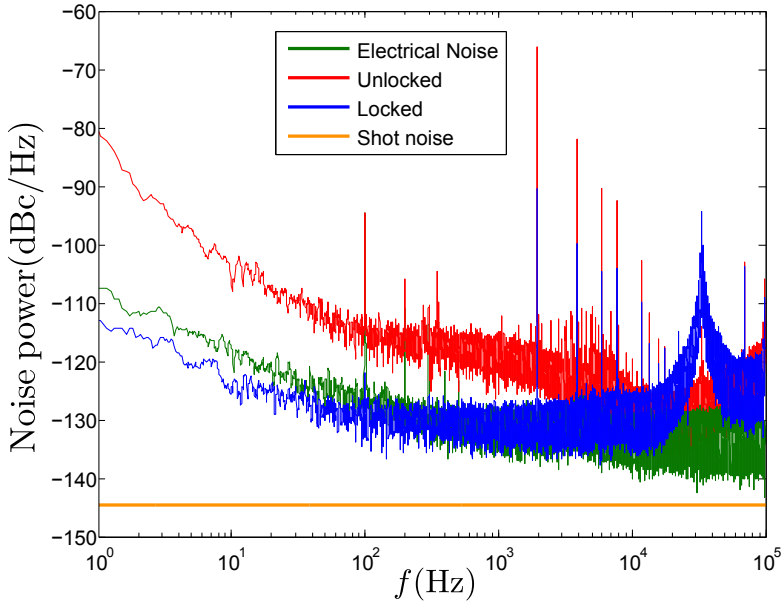

Figure 4.11. Relative intensity noise for different laser configurations in decibels-relative-to-carrier per Hz (dBc/Hz). At low frequencies the system is limited by electrical noise.

4.4.2 Atomic ensemble heating due to intensity noise

The authors of [56] use a simple model to describe how intensity noise on a dipole trap laser can heat trapped atoms. They go on to show that the heating rate Γ_ϵ of trapped atoms with trap frequency f_{tr} can be estimated from the noise spectrum of the laser as

$$\Gamma_\epsilon = \pi^2 f_{tr}^2 S_\epsilon(2f_{tr}) \tag{4.31}$$

where S_ϵ is the power spectrum of $\epsilon(t)$. We performed this calculation for the data shown in Fig. 4.11, to produce Fig. 4.12, which shows the estimated heating rate $1/\Gamma_\epsilon$ as a function of trap frequency. The heating rate is the time needed for the energy of the cloud of atoms to increase by a factor of e.

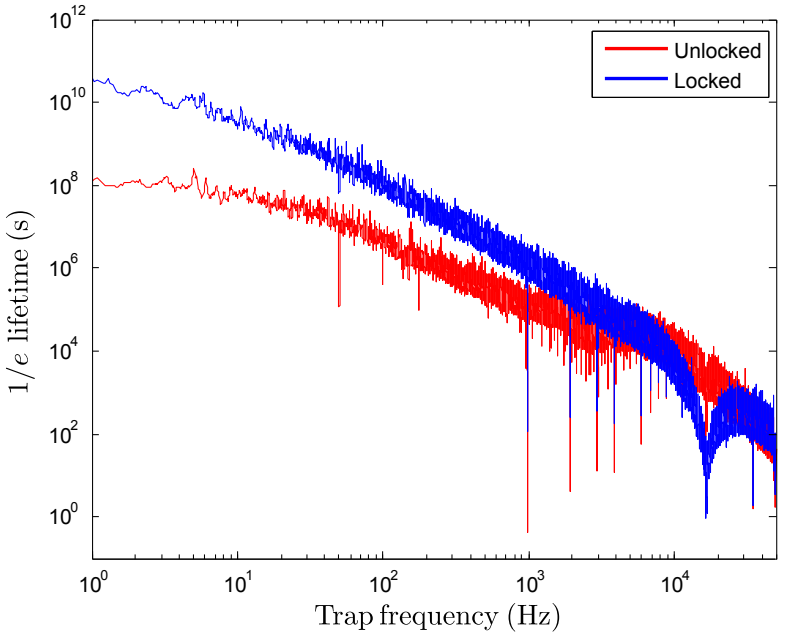

Figure 4.12. Estimated heating rate of atoms at a given trap frequency. The most important feature is that the feedback reduces the large negative peak at around 1 kHz from a lifetime of less than 1 second to over 100 seconds. At full power of our dipole trap laser we measured a trap frequency of around 1.3 kHz, so noise at frequencies above twice this is irrelevant for our system.

According to the analysis shown in Fig. 4.12, the lifetime limited by intensity noise should be on the order of hundreds of seconds. However, as mentioned in the previous section, this is an absolute upper bound as the measurement underestimated the noise power, especially at low frequencies. In the end, the lifetime of our dipole trap was found to be limited by background gas in the vacuum chamber, confirming the efficacy of the feedback system.

4.5 Microwave-assisted constant-depth optical evaporation

Usually, production of BECs in optical potentials requires lowering of the trap depth to force evaporation (e.g. [11, 57]). Techniques do exist to obtain an optical

BEC without lowering of the optical trap depth. For example using a combined optical-magnetic potential [58, 59], using a particular highly-asymmetric optical potential [60], using a combination of light shifts and atoms with narrow transitions [50], or using an optical lattice [49].

Here I'll briefly present an idea developed with Morgan Mitchell and Pau Gomez for performing optical evaporation without lowering the trap depth. The advantage of not lowering the trap depth would be that the ensemble should thermalise quickly and thus the duration of the evaporation should be short, increasing overall experiment repetition rate. To my knowledge the fastest BEC experiment at the moment is that of [49], where they obtain a BEC in 0.3 s with very low atom loss and without any evaporative cooling, although the scheme depends on the BEC forming in an optical lattice. Also in this reference the scheme is performed with very few atoms: the resulting BEC contains 1400 atoms, although the authors claim it is scalable to much larger atom numbers.

A schematic of the evaporation scheme is shown in Fig. 4.13 for ^{87}Rb-like atoms in a Gaussian potential. An applied magnetic field gradient induces a spatially-dependent Zeeman shift between the sublevels of the upper ground state. An applied rf field resonant with atoms at the edge of the trap but not at the centre transfers atoms relatively high in the potential into the higher-energy ground state. A laser resonant with a cycling optical transition from the upper ground state pushes any atom excited into the upper ground state out of the trap, thanks to the cycling transition. By lowering the frequency of the microwave field, atoms lower and lower in the trap can be selectively removed.

4.5.1 Number of transitions required to escape

To study this evaporation scheme a bit more quantitatively, I looked at how many photons an atom needs to scatter to escape the trap (in one dimension), which can be used to estimate heating from off-resonant transitions. The atoms excited to $F = 2$ by the microwave field are pushed out of the trap by photons in the push beam, which will transfer momentum to the atoms. The atoms will accelerate at a rate that depends on the balance between the force from the push beam and the restoring force from the dipole trap. The force from the dipole trap is the derivative of the dipole potential Eq. (4.5):

$$F_{trap} = -\nabla U_{dip} = -\frac{1}{2\epsilon_0 c}\mathrm{Re}(\alpha)\nabla I(x). \tag{4.32}$$

where $I(x)$ is calculated using Eq. (4.10) with $z = 0$. The force from the push beam is the rate of change of momentum, which is the momentum from one

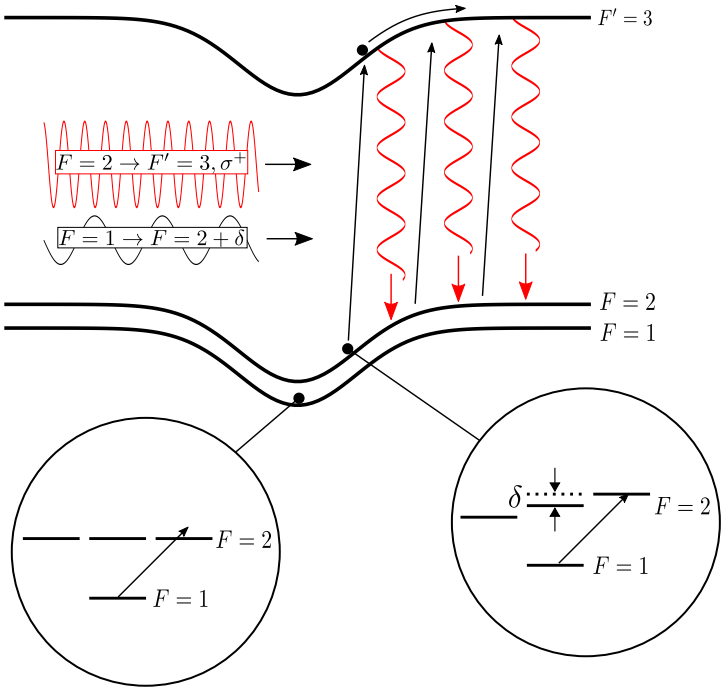

Figure 4.13. Representation of microwave-assisted optical evaporation. A magnetic field gradient induces spatially-dependent energy shift of the ground state levels, and an applied microwave field is resonant only with atoms near the edge of the trap. Atoms at the edge are transferred from $F = 1$ to $F = 2$, and are quickly pushed out of the trap by a laser resonant with the $F = 2 \rightarrow F' = 3$ cycling transition. Note some states are not represented for clarity.

photon times the scattering rate R_{sc}

$$F_{push} = R_{sc}\hbar k = R_{sc}\frac{h}{2\pi\lambda}. \tag{4.33}$$

The acceleration a of an atom is then:

$$a = \frac{d^2x}{dt^2} = \frac{1}{m}\left(F_{push} + F_{trap}(x)\right) \tag{4.34}$$

which is a second-order differential equation that can be solved numerically to find the position x of the atom at time t. Let's assume the worst-case scenario of a stationary atom starting from $\sigma/2$, which is the position of highest force

from the trap. The atom needs to be accelerated such that it has a total energy (kinetic + potential) equal to the trap depth to escape the trap. Fig. 4.14 shows the total energy of an atom starting from zero velocity at $x = \sigma/2$, with a push beam scattering photons at the rate given in the legend. The total energy of the atom is given by

$$E = U(x) + \frac{1}{2}mv^2 \tag{4.35}$$

where $U(x)$ is given by Eq. (4.5) and $v = dx/dt$ is the velocity of the atom from solving Eq. (4.34). This quantity is equal to zero when the atom has enough energy to escape the trap. Fig. 4.14 shows the expected behaviour: a high scattering rate kicks the atom out quickly, while lower scattering rates take longer to kick the atom out, until below a critical scattering rate the atom does not escape at all, and instead begins to oscillate inside the trap. To quantify this slowdown, Fig. 4.15a shows the number of scatters required for an initially stationary atom to escape from initial position $x_0 = \sigma/2$ as a function of scattering rate.

4.5.2 Differential light shift

The escaping atoms must be always on-resonance with the push beam as they are moving out of the trap, so I have not attempted to test this scheme in our experiment due to the strong differential light shift, which makes the resonance frequency position-dependent. In an ODT at, say, 1064 nm, this scheme would be much more feasible as at this wavelength and at typical intensities the differential light shift is negligible.

4.5.3 Off-resonant excitation of the $F = 2 \rightarrow F' = 1, 2$ transitions

To estimate off-resonant heating effects from the $F = 2$ ground state, I'll make two worst-case assumptions: 1) With a scattering rate equal to $\Gamma/4$, which is the case if the push beam intensity is equal to the saturation intensity, the most photons an atom needs to scatter to escape the trap is about 300 (see Fig. 4.15b). 2) Off-resonant excitation is much more likely in the case of an unpolarised or linearly polarised push beam, so in the following I'll assume a linearly polarised push beam.

Averaged across all sublevels, the on-resonant Rabi frequency of the $F = 2 \rightarrow F' = 2$ transition is $5/14$ of that of the $F = 2 \rightarrow F' = 3$ transition, and the $F = 2 \rightarrow F' = 3$ is $1/14$. Atoms excited to $F' = 2$ have a $1/2$ chance of decaying back to $F = 1$, and those excited to $F' = 1$ have a $5/6$ chance of decaying back to $F = 1$, returning their additional kinetic energy to the ensemble (relative

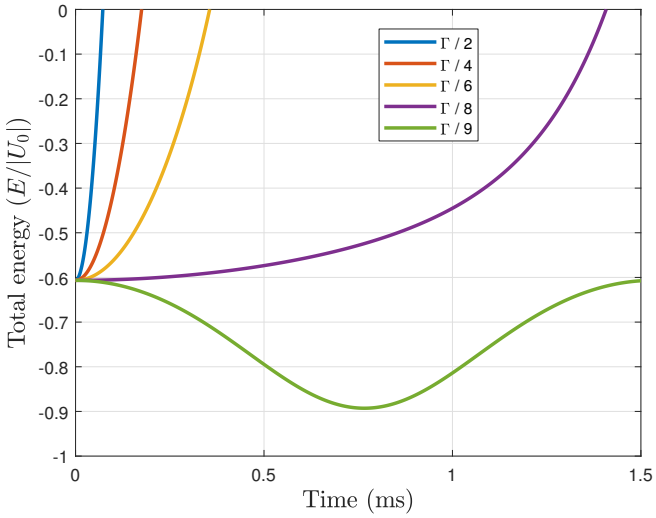

Figure 4.14. Total (kinetic + potential) energy of an atom pushed out of a dipole trap by a push beam. The atom starts with zero velocity at $x = \sigma/2$, and the scattering rate is given as a fraction of the natural linewidth Γ. $\Gamma/2$ is the scattering rate in the high-intensity limit. Below a critical scattering rate, about $\Gamma/8.11$ in this case, the atom does not escape the trap but instead begins to oscillate. Made by solving Eq. (4.34) with α calculated for the $5S_{1/2}$ ground state with light at 1560 nm, a peak intensity of $I_0 = 2.91 \times 10^9\,\mathrm{W\,m^{-2}}$, an ODT waist of $\sigma = 45\,\mu\mathrm{m}$ (i.e. a total beam power of about 10 W), a push beam at 780 nm, and $\Gamma = 6\,\mathrm{MHz}$.

transition strengths are shown in Fig. 4.16). If the push laser is resonant with the $F = 2 \to F' = 3$ transition, using Eq. 4.16, the relative scattering rate of the $F = 2 \to F' = 2$ transition is $1/(1 + 4(266/6)^2) \times 5/14 \approx 1/22,016$. So for every $22,016/300 \approx 73$ atoms that escape the trap, one is excited to the $F' = 2$ state. Half of those excited to $F' = 2$ (so 1 in 146) decay to the $F = 1$ ground state, going off-resonant with the push laser and returning their energy to the ensemble.

For the $F = 2 \to F' = 1$ transition, the relative scattering rate is $1/(1 + 4(266 + 157)^2/6^2) \times 1/14 \approx 1/278,348$. Taking into account the 5/6 probability of decay to $F = 1$, we find that one in every 1134 atoms decays into the $F = 1$ state through this transition, instead of being pushed out of the trap.

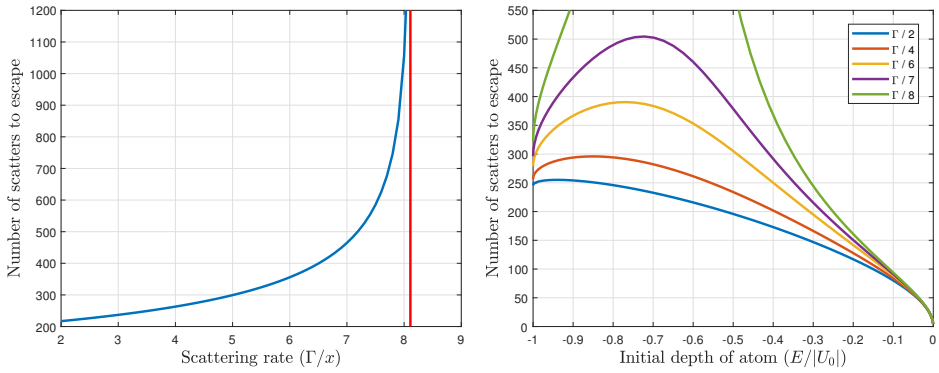

(a) (b)

Figure 4.15. (a) The number of photon scattering events required to escape the trap vs. the scattering rate for an atom starting from $x = \sigma/2$. The higher the scattering rate the less scattering events are required to escape the trap. Made using the same parameters as Fig. 4.14, and the number of scattering events was counted as $R_{sc} \times t_{esc}$, where t_{esc} is the time taken to reach 0 total energy. The red line shows the critical scattering rate. (b) Number of scattering events to escape as a function of the initial position of the stationary atom for a range of R_{sc}. All data was obtained by numerically solving Eq. (4.34).

In total, approximately 1 in 130 atoms will not escape the trap but will return to the ensemble with higher energy. Note that this is in the case of an atom starting from the "worst" possible trap depth. Atoms pushed from a higher or lower position in the trap will undergo fewer transitions, and be less likely to return their energy to the ensemble.

These numbers have been calculated assuming unpolarised or linearly polarised light. In the ideal case of a perfectly circularly polarised push beam, there is in principle *no* off-resonant excitation of any other transition from $F = 2$. While this is never the case in a real experiment, heating through these off-resonant transitions should be much less than this estimated value, which in any case does not appear to make this evaporation scheme unfeasible.

4.5.4 Off-resonant excitation of the $F = 1 \rightarrow F' = 0, 1, 2$ transitions

Off-resonant excitation from the $F = 1$ ground state would cause a background heating effect, as atoms everywhere in the trap are equally likely to be excited

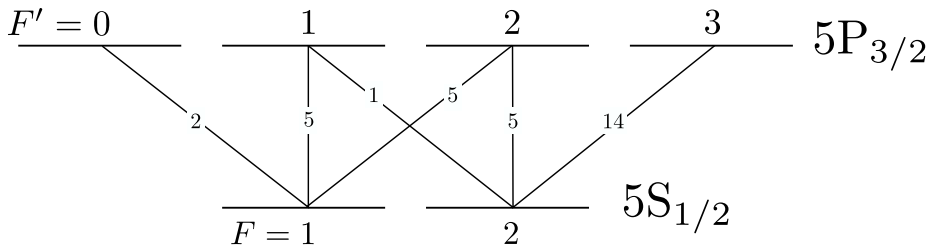

Figure 4.16. Relative transition strengths/on-resonance Rabi frequencies of different transitions between the $5S_{1/2}$ and $5P_{3/2}$ states of ^{87}Rb, averaged over π and $\sigma^{\pm}$ transitions. Data from Appendix D of [20].

on these transitions by the push laser. Table 4.1 shows the excitation rate of the different transitions calculated using Eq. (3.1) with $I/I_0 = 1$. The total excitation rate from the $F = 1$ state is about 0.55 Hz, meaning that for every second of evaporation, $0.55 \times N_{tot} k_B \cdot 0.36\,\mu\text{K}$ of energy is added to the ensemble, where N_{tot} is the total number of atoms. The total energy of the ensemble is $3N_{tot}k_BT$ [54]. T is of course a function of time, but if we take for an order of magnitude estimate a typical initial condition of $T = 30\,\mu\text{K}$, the background heating effect is about 0.2% of the total energy of the ensemble per second. This fraction would increase as the ensemble temperature decreases. The heating could be minimised by sweeping the microwave frequency faster to reduce the overall evaporation time, but sweeping the microwave too fast would mean the ensemble does not have time to thermalise and the evaporation would become inefficient. In any case this heating rate is again an overestimate. A circularly-polarised push beam would favour the $F = 1 \rightarrow F' = 2$ transition, reducing the rates of the other two.

Excitations on these transitions could also have a cooling effect, as some atoms will be transferred from the $F = 1$ to the $F = 2$ ground state and quickly pushed out of the trap. From Fig. 4.16, an atom excited from the $F = 1$ ground state has about a 28% chance of ending up in the $F = 2$ ground state. Once in the $F = 2$ ground state the atom is resonant with the push laser.

4.5.5 Selectivity of the microwave field

This evaporation scheme would need the microwave field to transfer atoms from $F = 1$ to $F = 2$ in a slice narrow relative to the size of the trap. If it were too wide too many atoms would be kicked out of the trap at once, resulting in inefficient evaporation. This could be controlled by the gradient of the magnetic field.

$F = 1 \rightarrow$	Ω (rel.)	Δ (MHz)	R (Hz)
$F' = 2$	5/14	6568	0.22
$F' = 1$	5/14	6412	0.23
$F' = 0$	1/7	6340	0.10
		Total	0.55

Table 4.1. Scattering rates of all the possible transitions from the $F = 1$ ground state with a push laser resonant with the $F = 2 \rightarrow F' = 3$ transition. Calculated using Eq. (3.1) with $I/I_0 = 1$ and scaling by the Rabi frequencies Ω relative to the $F = 2 \rightarrow F' = 3$ transition Rabi frequency, averaged over all possible π and $\sigma^{\pm}$ transitions.

The linewidth of the hyperfine ground-state transition in ^{87}Rb is 0 as the$F = 2$ ground state is metastable. This transition is subject to power broadening, and a power-broadened linewidth of, say, 1 kHz is reasonable. The Zeeman shift of these ground states is 700 kHz/G [35]. It is experimentally feasible to have a gradient of, say, 0.1 G across the width of the dipole trap, so a Zeeman shift of 70 kHz across the ensemble.

Another possibility is using optical Zeeman shifts to control the energy levels. One way of doing this would be to use an additional beam in some way, but possibly one could use a circularly-polarised dipole trap to provide both the trapping potential and energy level gradients used during the evaporation. This could maybe be done, for example, with ^{87}Rb in a circularly-polarised dipole trap at 790 nm, where the scalar light shift of the ground state is zero but the vector light shift is not.

4.5.6 Outlook

This scheme looks similar to evaporation with an rf knife in a magnetic trap but with much faster thermalisation and several additional heating mechanisms. The fast thermalisation means the evaporation could be more efficient than conventional optical evaporation, provided the additional heating is not too fast. The scheme works better for ODTs with high trap frequencies, as the thermalisation will be faster and thus the overall evaporation time will be shorter, reducing the background heating.

The above analysis has not identified any serious impediment to this evaporative cooling method, but more work should be done to study the thermalisation in this scheme as it is probably highly dependent on the shape of the optical potential, and this analysis might have missed a problem in the full dynamics of the situation. For example if the atomic ensemble becomes too dense the atom number could decay rapidly due to three-body collisions [61] [62] [52], or perhaps

the off-resonant heating is simply too great for this to work.

Chapter 5

Light shifts with Floquet's theorem

5.1 Introduction

Atomic energy level shifts due to an optical field are known as *light shifts* or *ac Stark shifts*, and are well known in physics. Light shifts can be exploited to determine atomic properties for fundamental physics [63, 64], in sensing applications such as optical magnetometry where they can be detrimental [65, 66] or beneficial [67], they can be used to characterise optical traps as explained in detail in Chapter 4 [43, 44], have recently been exploited for fine control and addressing of individual qubits in a trapped-ion quantum information processor [68], and even used to make a BEC without evaporative cooling [50]. Using light shifts to manipulate atomic spins for quantum information storage and manipulation is a growing field [69]. Light shifts due to both blackbody radiation and probe light are a limiting factor in the accuracy of modern optical atomic clocks [41, 70].

During the characterisation of the BEC experiment in Barcelona, we wanted to quantitatively describe the energy level shifts of atoms trapped in the ODT, as this affected loading dynamics. The ODT at 1560 nm induces strong light shifts of the $5P_{3/2}$ levels due to its proximity to the excited-state transitions to the 4D levels around 1529 nm (see Fig. 5.1). This experiment also has an additional laser at 1529 nm to compensate for these level shifts. The 1560 nm light is close enough to the excited-state resonance to produce a slight nonlinearity in the level shifts, and the 1529 nm light produces highly nonlinear level shifts.

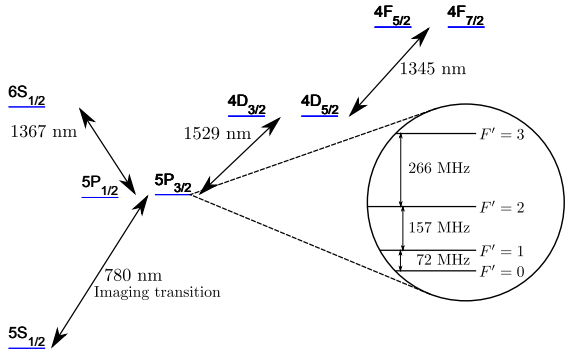

Figure 5.1. ^{87}Rb energy levels used for calculations presented in Chapters 5 and 6. We performed several representative calculations with many more matrix elements up to $n = 10$ and found that these made a < 1 MHz contribution to the calculated light shifts under our experimental conditions, which is less than the uncertainty in our measurement. The inset shows the hyperfine splitting of the $5P_{3/2}$ levels. We included hyperfine splitting for all levels except the 4F levels, for which we were unable to find hyperfine constants in the literature.

We found that the conventional description of light shifts was insufficient for our experiment. Light shifts are usually calculated using second-order perturbation theory (e.g. [68, 71–77]), but this is not adequate in situations with strong nonlinear light shifts and non-negligible mixing of different hyperfine energy levels, which can be the case if the light is sufficiently near-resonant with an atomic transition like in our experiment, especially in the case of moderate intensities of our 1529 nm beam.

In order to accurately describe the combined effect of both the 1560 nm and 1529 nm beams, we developed a calculation based on Floquet's theorem. The theory and experimental results have recently been published in *Optics Express* [78]. In this chapter I will describe the theory, which includes a section not in the paper about how to combine light shifts with magnetic fields, giving a "toolbox" for experimental manipulation of atomic energy levels.

There is nothing in the theory specific to any particular transition or atom, so it could be useful for calculating light shifts in any system involving optically trapped atoms. Indeed, it could greatly expand the range of experimental possibilties with conventional optically-trapped atoms, optically-trapped molecules [79], atoms in optical lattices [80], or atoms trapped close to optical fibers [81].

The theory can accurately describe light shifts in a regime analogous to the magnetic Paschen-Back regime, i.e. a regime where the light shifts are large, non-linear, and there is strong mixing of the hyperfine levels. It can describe light shifts due to multiple lasers of arbitrary polarization with wavelengths close to atomic resonances, with the limitation that the different wavelengths must be related by a rational fraction. At the same time, the mathematics is considerably simpler than in perturbative treatments [76, 77] and handles strong level mixing in a natural way, thus extending the possibilities of light-shift engineering, e.g. for state preparation [82], and light-shift compensation techniques such as that demonstrated in [83, 84].

The theory presented here could have a potential application in measuring excited-state electric-dipole matrix elements. Precise knowledge of dipole matrix elements is important for e.g. optical clocks, testing atomic structure calculations [85], and atomic parity non-conservation measurements [86, 87]. The idea of using light shifts to measure dipole matrix elements is not new [64, 88], but the theory here can be used in a regime of strong light shifts, where errors in electric-dipole transition matrix elements should manifest as a larger discrepancy between theory and experiment.

5.2 Floquet theory of light shifts

The basic idea of this theory is that light acts as a periodic potential for an atom, which is a situation amenable to solution using Floquet's theorem. There is a wealth of research describing quantum systems in time-periodic potentials, the first paper probably published by John Shirley in 1965 [89].

5.2.1 Solving a periodic Hamiltonian

Floquet's theorem states that the Schrödinger equation

$$i\hbar\frac{\partial}{\partial t}\psi(t) = H(t)\psi(t) \tag{5.1}$$

with time-periodic Hamiltonian $H(t) = H(t+T)$ has solutions of the form $\psi(t) = \phi(t)e^{-i\omega_F t}$, where $\phi(t) = \phi(t+T)$ has the same periodicity as $H(t)$. In the case of an atom in an oscillating external field, we have $H(t) = H_0 + V(t)$, where H_0 is the free-atom Hamiltonian and $V(t) = V(t+T)$ is a periodic potential [89]. $\psi(t)$ describes a dressed state of the Hamiltonian, with dressed energy $\hbar\omega_F$.

To find the dressed states, we just need to find $\mathscr{U}(T,0)$, the time-evolution operator for one period of the potential for which

$$\psi(t+T) = \mathscr{U}(t+T,t)\psi(t) = \psi(t)e^{-i\omega_F T}. \tag{5.2}$$

The eigenstates of this operator are thus the dressed states $\psi_i(t)$, with eigenvalues $\exp(-i\omega_{F,i}T)$. This determines $\omega_{F,i}$ up to additive multiples of $2\pi/T$. When $2\pi/T$ is large relative to fine- and hyperfine-structure splittings, $\hbar\omega_{F,i}$ can be unambiguously assigned by comparison against the bare energies.

To compute $\mathscr{U}(T,0)$, we use a numerical Euler method [90], although there is another popular method which involves diagonalising a truncated infinite matrix, described in Shirley's original paper [89] or for example [91]. In the technique described here, we first partition $\mathscr{U}(T,0)$ into N subintervals

$$\mathscr{U}(t_N,t_0) = \mathscr{U}(t_N,t_{N-1})...\mathscr{U}(t_2,t_1)\mathscr{U}(t_1,t_0). \tag{5.3}$$

then approximate $\mathscr{U}(t_1,t_0) \approx e^{-iH(t_0)(t_1-t_0)/\hbar}$ to find

$$\mathscr{U}(T,0) \approx \prod_{n=0}^{N-1} e^{-iH(t_n)T/(N\hbar)} \tag{5.4}$$

where $t_n = nT/N$, and the order of the product must be as in Eq. (5.3).

5.2.2 Hyperfine energy levels

Now we calculate the two terms in the Hamiltonian. We work in the basis $|nJFm_F\rangle$, in which the free-atom Hamiltonian H_0 is diagonal, with different m_F states degenerate

$$\begin{aligned}\langle nJFm_F|H_0|nJFm_F\rangle = \langle nJ|H_0|nJ\rangle &+ \frac{1}{2}\hbar A_{nJ}K \\ &+ \hbar B_{nJ}\frac{3K(K+1)/2 - 2I(I+1)J(J+1)}{2I(2I-1)2J(2J-1)}\end{aligned} \tag{5.5}$$

where $K \equiv F(F+1) - I(I+1) - J(J+1)$ and the hyperfine constants A_{nJ} and B_{nJ} for ^{87}Rb are taken from [85]. Fine-structure energies $\langle nJ|H_0|nJ\rangle$ are taken from the NIST atomic spectra database [92].

5.2.3 Atom-light interaction in the dipole approximation

We describe the interaction between the atoms and the light in the electric-dipole approximation, so

$$V(t) = -\mathbf{E}(t)\cdot\mathbf{d} \tag{5.6}$$

where $\mathbf{E}(t)$ is the electric field of a laser, and $\mathbf{d} = e\mathbf{r}$ is the electric-dipole operator. The electric dipole approximation effectively makes several approximations at the same time: only electric-dipole transitions are possible, the atom is only affected by the electric field of the laser beam, not the magnetic field, and only single-photon transitions are possible. These approximations are remarkably accurate most of the time, but in Chapter 6 I present some experimental data indicating a more sophisticated description is required in situations where the light is intense and very close to resonance.

To find the matrix elements of this interaction in our basis, it is convenient to work in Cartesian coordinates. Choosing z as the quantisation axis, we first find d_z, the z-component of $\mathbf{d}$, which describes $\Delta m_F = 0$ or π transitions.

$$\begin{aligned}\langle nJFm_F|d_z|n'J'F'm'_F\rangle = \langle nJ||e\mathbf{r}||n'J'\rangle(-1)^{m_F+J+I}\sqrt{(2F+1)(2F'+1)} \\ \times \begin{pmatrix} F' & 1 & F \\ m'_F & 0 & -m_F \end{pmatrix} \begin{Bmatrix} J & J' & 1 \\ F' & F & I \end{Bmatrix},\end{aligned} \tag{5.7}$$

where $(:::)$ and $\{:::\}$ are the Wigner 3-j and 6-j symbols, respectively, and the reduced matrix elements $\langle nJ||e\mathbf{r}||n'J'\rangle$ are known from the literature[1]. The d_z matrix can be rotated to find the d_x and d_y matrices:

$$\begin{aligned} d_x &= e^{iF_y\pi/2} d_z e^{-iF_y\pi/2} \\ d_y &= e^{-iF_x\pi/2} d_z e^{iF_x\pi/2} \end{aligned} \tag{5.8}$$

where $F_x = (F_+ + F_-)/2$ and $F_y = -i(F_+ - F_-)/2$ are total angular momentum components, given in terms of the ladder operators $F_\pm$ with matrix elements [94]

$$\langle nJFm_F|F_\pm|n'J'F'm'_F\rangle = \sqrt{(F \mp m_F + 1)(F \pm m_F)}\,\delta_{nJF,n'J'F'}\delta_{m_F,m_F'\pm 1}. \tag{5.9}$$

5.2.4 Electric field of a laser beam

The electric field is similarly described in Cartesian coordinates. As examples, if the incident optical field is monochromatic and polarized along $\hat{\mathbf{z}}$, the electric field is

$$\mathbf{E}_\pi(t) = \mathcal{E}\cos(\omega t)\hat{\mathbf{z}} \tag{5.10}$$

where $\mathcal{E}$ is the amplitude of the electric field, $\omega = 2\pi c/\lambda$ is the optical frequency, c is the speed of light, and λ is the wavelength. Circularly-polarized light has the

[1] We obtained all the matrix elements except three from [85], elements between the $4d$ and $4f$ states were obtained directly in a private communication from M. S. Safronova of U. Delaware. All the elements we used are available online [93].

field

$$\mathbf{E}_{\sigma^\pm}(t) = \frac{\mathcal{E}}{\sqrt{2}}\left[\cos(\omega t)\hat{\mathbf{x}} \pm \sin(\omega t)\hat{\mathbf{y}}\right]. \tag{5.11}$$

The electric field of two linearly polarized fields with amplitudes $\mathcal{E}_i$, polarizations $\mathbf{n}_i$ frequencies ω_i, $i \in \{1, 2\}$, can be written

$$\mathbf{E}(t) = \mathcal{E}_1 \cos(\omega_1 t)\hat{\mathbf{n}}_1 + \mathcal{E}_2 \cos(\omega_2 t)\hat{\mathbf{n}}_2. \tag{5.12}$$

It is important to note that the period T in Eq. (5.4) refers to one period of the *total* electric field, so we can calculate the light shifts due to multiple wavelengths as long as they are related by rational fractions. E.g. if $\lambda_1/\lambda_2 = a/b$, where a and b are positive integers, the period of the total electric field is the lowest common multiple of T_1 and T_2, where $T_i = 2\pi/\omega_i = \lambda_i/c$ is the optical period.

5.2.5 Extending beyond the electric dipole effect

In this formulation H_0 can be readily extended to include static electric and/or magnetic fields (this is described in Section 5.3), and V can be adapted to include magnetic and higher electric multipole transitions, provided the matrix elements are known. Note that we neglect any possible additional vacuum field, relaxation, continuum, or relativistic effects. As we neglect relaxation/excitation effects we effectively calculate only the real part of the polarisability and not the imaginary part (see Section 4.1.1).

5.2.6 Convergence of the numerical calculation

For the calculations presented in Chapter 6, we used only the energy levels shown in Fig. 5.1, comprising 136 distinct states. We performed several representative calculations with levels up to $n = 10$ and found these extra states contributed less than 1 MHz to the calculated light shifts which is below the resolution of our experiment, as explained below. We computed $\mathscr{U}$ numerically with Eq. (5.4) and cut off N at some finite value, but making sure it is sufficiently high such that the result has converged. For calculations with our 1560 nm beam only we used $N = 200$. All calculations were performed in MATLAB and our code is available online [93].

5.3 Combining light shifts and magnetic fields

With the inclusion of magnetic fields in the light shift calculation we can describe the level shifts of an atom in arbitrary static magnetic and ac electric/light fields, thus providing a "toolbox" to manipulate atomic energy levels using the

two most common techniques of doing so. This could be useful for, for example, calculating what magnetic field is required to compensate for some particular vector light shift (aka "fictitious magnetic field" [95]), or vice versa.

In the presence of an external magnetic field, and assuming the resulting shifts are small compared to the fine-structure splitting, the Zeeman interaction can be written as [35]

$$\begin{aligned} H_B &= (\mu_B/\hbar)(g_J\hat{\mathbf{J}} + g_I\hat{\mathbf{I}}) \cdot \mathbf{B} \\ &= (\mu_B/\hbar)(g_J\hat{J}_z + g_I\hat{I}_z)B_z \end{aligned} \tag{5.13}$$

However the $|F, m_F\rangle$ states are not eigenstates with an applied magnetic field, as m_J and m_I are not independently defined in this basis. We need to find a new basis where these quantum numbers are defined. We can change basis by finding each $|F, m_F\rangle$ state as a sum of $|J, m_J, I, m_I\rangle$ states, which form a complete set.

$$|Fm_F\rangle = \sum_{m_J=-J}^{J} \sum_{m_I=-I}^{I} |Jm_JIm_I\rangle\langle Jm_JIm_I|Fm_F\rangle \tag{5.14}$$

where $\langle Jm_JIm_I|Fm_F\rangle$ is the corresponding Clebsch-Gordan coefficient given by

$$\langle Jm_JIm_I|Fm_F\rangle = (-1)^{J-I+F}\sqrt{2F+1}\begin{pmatrix} J & I & F \\ m_J & m_I & -m_F \end{pmatrix} \tag{5.15}$$

Then the new eigenstates can be written as superpositions of the $|Fm_F\rangle$ states by diagonalising the total Hamiltonian in the new basis

$$\langle Jm_JIm_I|H_0 + H_B|J'm'_JI'm'_I\rangle, \tag{5.16}$$

To include magnetic fields in a light shift calculation, we need to write the entire Hamiltonian in the $|Jm_JIm_I\rangle$ basis, including the periodic term $V(t)$, which effectively means finding the dipole operator d_z and the rotation matrices F_x and F_y in the new basis. This can be done by writing eq. (5.14) as a matrix C and changing basis as e.g. $d'_z = Cd_zC^T$.

Figures 5.2 and 5.3 show example calculations of the energy shifts of the $5P_{3/2}$ levels in ^{87}Rb as a function of magnetic field, with and without additional light shifts, and as a function of light intensity at 1529.282 nm, with and without an applied magnetic field of 10 Gauss.

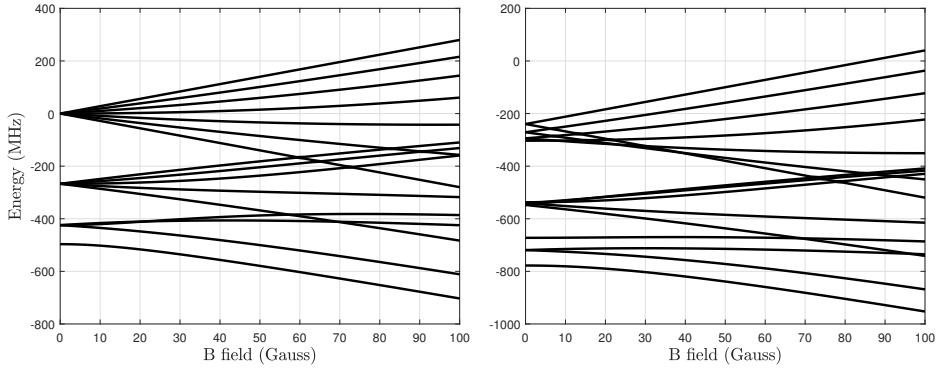

(a) (b)

Figure 5.2. Energy shifts of the $5P_{3/2}$ levels in ^{87}Rb as a function of magnetic field (a) without and (b) with an additional light shift from $3 \times 10^9\,\mathrm{Wm}^{-2}$ of linearly polarised light at 1560.0 nm. Note the shifted y-axes.

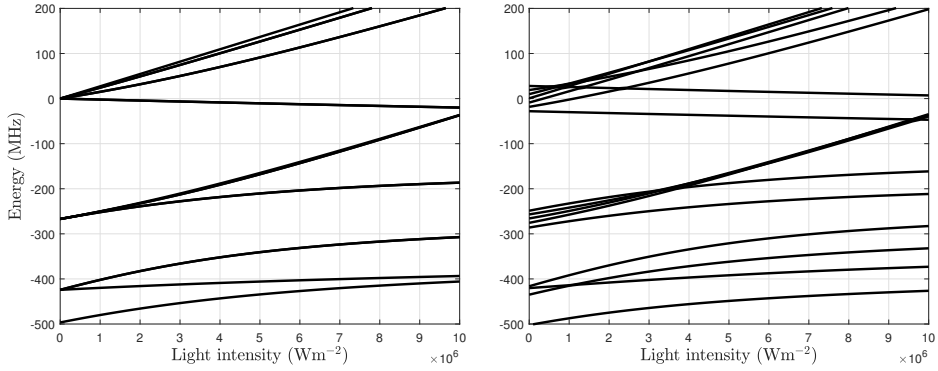

(a) (b)

Figure 5.3. Energy shifts of the $5P_{3/2}$ levels in ^{87}Rb as a function of light intensity at 1529.282 nm (a) without and (b) with an applied magnetic field of 10 Gauss.

5.4 Conclusion

This chapter presented a theory for the calculation of strong atomic light shifts due to multiple wavelengths of light which can be close to an atomic resonance.

The shifts can be nonlinear and larger than the hyperfine splitting. While no single part of the calculation is new, as far as we know this is the first such calculation of light shifts outside of the linear perturbative regime. Moreover, our results are not specific to any particular transition or atom, and should be widely applicable in any system involving optical trapping.

Chapter 6

Measurement of strong nonlinear light shifts

The light shift theory of Chapter 5 was tested by performing absorption spectroscopy on the light-shifted D_2 transition in optically trapped ^{87}Rb. The experiment can resolve light shifts of individual magnetic sublevels, and shows that there is good agreement between the measured and predicted positions of atomic energy levels after calibration of the in-situ light intensity and polarization, although a careful measurement finds a small unexplained discrepancy. We use the simple model of atoms in a dipole trap derived in Chapter 4 to explain the observed spectra. The spectra are sensitive to both the trapping light intensity and polarization and can be used for calibration of both.

This chapter describes the setups and results of measurements in three different configurations:

- The first experiment, and preliminary test of the theory, measured the absorption of atoms trapped in the ODT characterised in Chapter 4. This ODT has a wavelength of 1560.492 nm, a total power of about 10 W and a peak intensity of about $3 \times 10^9\,\mathrm{W\,m^{-2}}$. The light shifts of ^{87}Rb in this environment are almost linear, so this experiment constituted a test of the theory in a regime that agrees with perturbation theory within experimental error. The results are compared to a calculation using the Floquet-based theory. This experiment was also useful to calibrate the intensity and polarisation of the 1560 nm laser, parameters which were used for calculating light shifts in the second experiment.

- The second experiment added a beam at 1529 nm which was mode-matched to the 1560 nm beam. Light at 1529 nm induces very strong light shifts

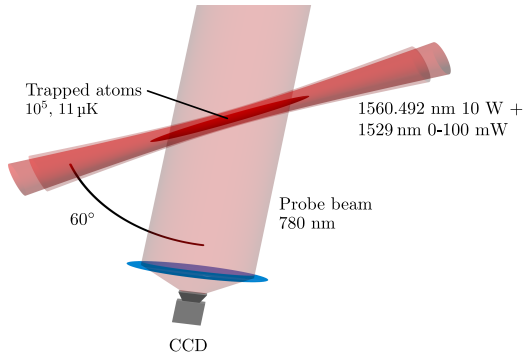

Figure 6.1. Experimental setup of first and second light shift measurement. The high-power ODT at 1560.492 nm was used to hold the atoms and induce a medium-strength light shift, while the second mode-matched beam at 1529 nm is used to induce strong light shifts without strongly affecting the potential experienced by the ground state of the atoms. Absorption of a probe beam at 780 nm is measured on a CCD camera.

in rubidium, so this experiment tested the theory well beyond the linear regime, as well as testing calculations of light shifts due to multiple wavelengths. In this and the previous experiment the measurements agreed with the theory to within the experimental uncertainty. The precision of this experiment was limited by the 1529 nm laser not being frequency-locked.

- The final experiment used a different experimental sequence to measure with a much denser cloud than in the previous two measurements which reduced the signal broadening, and also a higher intensity of the 1529 nm light, resulting in larger shifts of some levels. I also constructed a system to stabilise the 1529 nm laser which was limiting the precision of the previous measurement. The results of this measurement show an as-yet unexplained deviation from theory.

6.1 Light shifts @ 1560 nm + 1529 nm

A schematic of the configuration of the first and second experiments is shown in Fig. 6.1. To trap the atoms we used an optical dipole trap consisting of a single linearly polarized 10 W ($\sim 3 \times 10^9\,\mathrm{W\,m^{-2}}$) beam locked with < 100 kHz stability to 1560.492 nm (the second harmonic of which is locked to a transition of the ^{87}Rb D_2 line at 780.246 nm), and focused to a spot size of $\sim 44\,\mu$m. A second

beam near 1529 nm was mode-matched to the 1560 nm beam, with a controllable power from 0-100 mW (0-3.3 $\times 10^7\,\mathrm{W\,m^{-2}}$). The two beams were combined on a polarizing beamsplitter, with the 1560 nm light reflected and the 1529 nm light transmitted, so the nominal polarisations are linear vertical and linear horizontal, respectively. The 1560 nm beam is not perfectly linear before the beamsplitter, and the polarization is not perfectly cleaned on reflection from the cube, so there is some residual ellipticity. The 1529 nm beam could be scanned across the $5P_{3/2} \rightarrow 4D_{3/2(5/2)}$ excited-state resonances at 1529.26 (1529.36) nm (see Fig. 5.1), so we could induce strong light shifts in the $5P_{3/2}$ states with relatively low intensities. Initially, we measured three datasets: one with no 1529 nm light present, another with the 1529 laser at 1529.282 nm and another at 1529.269 nm. The 1529 laser was not frequency-stabilised, and the wavelength was measured with a calibrated wavemeter to drift by ± 0.001 nm from the nominal wavelength over the duration of the measurements. Measurements of the 1529 nm laser wavelength were limited by the resolution of the wavemeter, but the observed fluctuations of ± 0.001 nm (approximately ± 100 MHz at this wavelength) were corroborated by the measured data. For the absorption signal, a probe beam at 780 nm propagates at an angle of 60° relative to the trap axis, to reduce the chance of producing states that are "dark" to the probe light. Absorption by the atoms was measured using a PCO Pixelfly CCD camera and a standard absorption imaging technique (see Chapter 3 for more information about our image processing). The probe laser was stable to less than 100 kHz, and could be scanned up to 1 GHz to the red side of the D_2 transition.

The experimental sequence was as follows: We trapped approximately 3 $\times 10^6$ atoms in the $F = 1$ ground state in the 1560 nm optical dipole trap. Initially the trap depth was about 270 µK and the atoms had a temperature of about 40 µK. To ensure the atoms experienced as homogeneous a light intensity as possible, we reduced the temperature and therefore the spatial extent of the cloud by performing an evaporation sequence followed by adiabatic increase of the trap depth back up to about 270 µK, obtaining $\sim 10^5$ atoms at 11 µK. We then pumped the atoms into the $F = 2$ ground state and measured absorption of the probe laser as a function of the frequency of the probe beam and intensity of the 1529 nm beam.

6.1.1 Results @ 1560 nm only

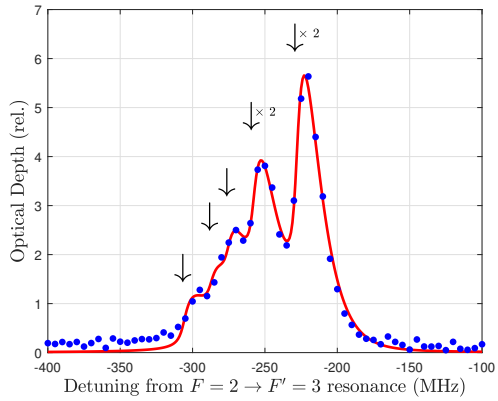

Figure 6.2. Relative optical depth of atoms in the dipole trap around the light-shifted $F = 2 \rightarrow F' = 3$ transition with only 1560 nm light. Blue dots show measured optical depth in a small transverse slice of the dipole trap, extracted from absorption images. Each point is from a single experiment run. The red line is a fit using Eq. (6.1). The x-axis is relative to the free-space $5S_{1/2}, F = 2 \rightarrow 5P_{3/2}, F = 3$ transition. Free parameters in the fit were peak amplitudes, trap depth, and the ellipticity of trap light. Arrows show positions of resonances at maximum trap depth. The finite temperature of the atoms systematically shifts the measured peaks relative to the arrows. "×2" indicates 2 resonances within the width of the arrow.

The first measurement was the absorption spectrum of atoms in the trap with just the 1560.492 nm trap itself, i.e. with zero intensity of the 1529 nm beam. Fig. 6.2 shows relative optical depth as function of probe beam frequency at zero 1529 nm beam intensity. We say "relative" as our image processing was calibrated for measuring the density of atoms in free space, correcting for saturation as described in Chapter 3.

This experiment measured absorption on the $5S_{1/2}, F = 2 \rightarrow 5P_{3_2}, F = 3$ transition. In the conditions of this experiment, the five magnetic sublevels in the lower state have the same polarisability to within experimental resolution, while each of the seven magnetic sublevels in the upper state has a unique polarisability that depends on the wavelength, intensity, and polarisation of the trapping light. Thus we used a modified version of Eq. (4.27) to model the signal:

$$A(\delta) = \sum_{i=1}^{7} C_i \int_0^\infty \frac{u^2 e^{-u^2} du}{1 + 4(\delta + \nu_i - t_i u^2)^2} \tag{6.1}$$

where i indicates the i^{th} state, and C_i is a fitting parameter depending on the number of atoms measured and the absorption cross-section of the i^{th} level for the probe beam.

To fit Eq. (6.1) to the data shown in Fig. 6.2 we modelled the electric field of the 1560 nm laser as

$$\mathbf{E}_1(t) = \frac{\mathcal{E}_1}{\sqrt{2}}(\cos(\omega_1 t)\hat{\mathbf{x}} + \cos(\omega_1 t + \phi)\hat{\mathbf{y}}), \tag{6.2}$$

and calculated the light shifts as described in Section 5.2, to obtain the differential light shift and consequently the differential polarisability α_e/α_g, as this quantity is equal to $\Delta f_e/\Delta f_g$, where $\Delta f_{e(g)}$ is the light shift of the excited (ground) state. We included the quadrature phase ϕ to account for a slight ellipticity of the 1560 nm light after reflection at a polarizing beamsplitter as discussed in above. If $\phi = 0$ this simply describes a linearly polarized electric field oscillating in the $\hat{\mathbf{x}} + \hat{\mathbf{y}}$ plane. The coefficients C_i, electric field E_1, and quadrature phase ϕ were free parameters in the fit[1]. The light intensity is related to the electric field by

$$I = \frac{\epsilon_0 c}{2}|E|^2 \tag{6.3}$$

where ϵ_0 is the permittivity of free space and c is the speed of light. From the fit we extracted $I_{1560} = 2.91 \pm 0.01 \times 10^9\,\mathrm{Wm}^{-2}$, which agrees well with power meter measurements, and $\phi = 0.133 \pm 0.009$. By using colder atoms and/or a deeper trap, these quantities could be known more accurately. The trap depth U is equal to the light shift of the ground state at peak light intensity at the center of the trap. We obtained $U = h \cdot 5.623 \pm 0.004\,\mathrm{MHz}$ ($= k_B \cdot 270.0 \pm 0.2\,\mu\mathrm{K}$). We can compare the U obtained from the fit to U_{calc} calculated from the measured trap oscillation frequency $f_{osc} = 1.22\,\mathrm{kHz}$ and the beam waist measured with a beam profiler $w = 44\,\mu\mathrm{m}$ as $U_{calc} = (2\pi w f_{osc})^2 m/4 = h \cdot 6.2\,\mathrm{MHz}$. The difference between the two can be explained with an error in the measurement of the beam waist of 2 µm, which is entirely feasible.

The arrows in Fig. 6.2 show calculated light shifts of atomic transitions at the bottom of the trap, i.e. $\Delta f_{e,i} - \Delta f_g$ at peak light intensity. The data peaks are slightly offset from the theoretical peaks due to the finite temperature of the atoms: atomic density peaks above the bottom of the trap.

[1] Quantitative prediction of C_i is feasible but would require use of the optical Bloch equations to solve for atomic dynamics in the presence of the 1560 nm beam, the single probe beam at 780 nm, and repump light also at 780 nm which is emitted from six directions toward the centre of the trap.

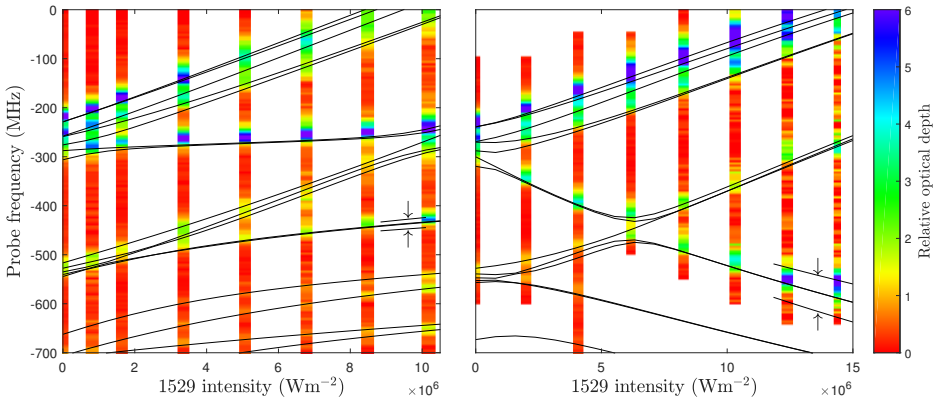

(a) $\lambda_2 = 1529.282$ nm. (b) $\lambda_2 = 1529.269$ nm.

Figure 6.3. Probe absorption with $\lambda_1 = 1560.492$ nm and λ_2 given in the respective subcaption.The probe frequency is indicated relative to the free-space $5S_{1/2}, F = 2 \rightarrow 5P_{3/2}, F = 3$ transition. The black lines show calculated energy levels of dressed states at peak light intensity, these are offset from the data due to the finite temperature of the atoms. Shading shows measured optical depth of the atomic cloud in arbitrary units with the scale shown in the colour bar on the right. Each column is scaled to have the same maximum value. After using the data shown in Fig. 6.2 as a calibration of the experimental parameters, the only fitting parameter here is the 1529 nm beam power. The arrows point to lines showing the calculated light shifts for a change in wavelength of the 1529 nm laser by ± 0.001 nm, for a particular level.

6.1.2 Bichromatic light shifts @ 1560 nm + 1529 nm

Figs. 6.3a and 6.3b show absorption of the probe beam as a function of probe frequency and 1529 beam intensity. The black lines are calculated transition frequencies relative to the free-space $5S_{1/2}, F = 2 \rightarrow 5P_{3/2}, F = 3$ transition. We used the data shown in Fig. 6.2 as a calibration of the parameters of the 1560 nm beam, to then perform the calculation of energy level shifts as a function of 1529 nm beam intensity, so the only fitting parameter here is the calibration of the 1529 nm beam intensity. The left-most column in Fig. 6.3a shows the same data as that shown in Fig. 6.2, while that shown in the left-most column of Fig. 6.3b is a different data set but measured under the same conditions.

For calculating light shifts with both the 1560 nm and 1529 nm beams present we model the electric field as

$$\mathbf{E}(t) = \mathbf{E}_1(t) + \frac{\mathcal{E}_2}{\sqrt{2}}[\cos(\omega_2 t)\hat{\mathbf{x}} - \cos(\omega_2 t)\hat{\mathbf{y}}] \tag{6.4}$$

which describes the electric field of the 1560 beam added to the linearly polarized 1529 beam. The two fields have linear orthogonal polarisations if $\phi = 0$. The wavelength of the 1560 nm trapping beam was $\lambda_1 = 1560.492\,\text{nm}$, so for one measurement we set the wavelength of the 1529 nm beam to be $\lambda_2 = \frac{49}{50}\lambda_1 = 1529.282\,\text{nm}$. For the data shown in Fig. 6.3b, at 1529.269 nm λ_2 is closer to a resonance so the nonlinearity is clearer, including avoided and non-avoided crossings. Because the ratio of experimental wavelengths does not form a simple rational fraction, black theory curves are calculated with $\lambda_1 = 1559.854\,\text{nm}$ (i.e. $\lambda_1 = \frac{51}{50}\lambda_2$). We mostly compensate for this mismatch between the real and assumed wavelength of the 1560 nm light by reducing the intensity of light in the calculation by 2.6%. There is still an estimated error of up to 150 kHz in the calculated light shifts, however this is below the uncertainty introduced by the drift of the 1529 nm laser, which was not frequency-stabilised.

The arrows in Figs. 6.3a and 6.3b point to lines representing the light shifts for a representative level given a change in the 1529 nm laser wavelength of ± 0.001 nm, showing that data and theory agree to within experimental error given the uncertainty of the laser wavelength.

6.2 Higher precision measurements @ 1529 nm

While the measurements in the previous section agree with the theory to within experimental uncertainty, I was interested in testing the limits of the Floquet theory more accurately. For this reason I built a "transfer lock" using a fibre-based Mach-Zehnder interferometer to stabilise the 1529 nm laser, which was the main source of uncertainty in the previous measurements. The interferometer works by using the 1560 nm laser as a sensitive thermometer to stabilise the temperature of the apparatus, then the 1529 nm laser can be locked using the output signal of the interferometer. This effectively transfers stability from the atomic-referenced 1560 nm laser. The interferometer was measured to stabilise the frequency of the 1529 nm laser to $< \pm 250\,\text{kHz}$ ($\pm 2 \times 10^{-6}\,\text{nm}$) over 16 hours, down from a drift rate of around 100 MHz ($\sim 1 \times 10^{-3}\,\text{nm}$) in one hour. The interferometer itself is described in Appendix A. I also developed a new experimental sequence to measure light shifts at the highest available intensity of just the 1529 nm laser, i.e. without the 1560 nm laser.

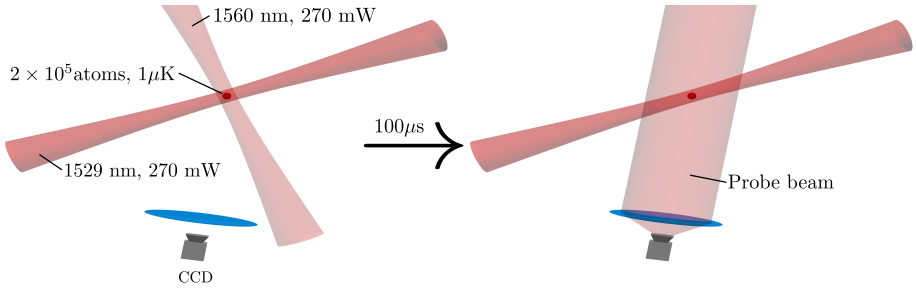

Figure 6.4. Schematic of the experimental sequence for measuring light shifts due to just the 1529 nm beam. The atoms are trapped in a crossed-beam trap consisting of the 1560 nm beam in one direction and the 1529 nm beam in the other. This crossed-beam trap is used to efficiently evaporate the atoms down to 1 µK, then the 1560 nm beam is switched off, and the absorption is quickly measured before the atoms have time to move.

6.2.1 Experimental sequence to produce a higher-density ensemble

The experimental sequence presented in the previous section measured the light shifts over a wide range of intensities of the 1529 nm laser. The potential for the atoms was mainly due to the 1560 nm laser which did not change, while the light shifts of the 5P levels were mainly due to the 1529 nm laser which could be varied in wavelength and intensity without affecting the preparation of the atoms. The results of this measurement agreed with the calculations to within experimental uncertainty, however with the insight from this first experiment I was able develop a new experimental sequence with a decreased measurement uncertainty and larger-magnitude light shifts. I was able to reduce the experimental uncertainty in two ways: 1) Stabilise the 1529 nm frequency with the interferometer, and 2) develop a new sequence to produce an ensemble of atoms with decreased temperature to reduce the asymmetric temperature-dependent broadening of the absorption peaks.

The new experimental sequence consisted of trapping atoms in the crossing of the 1529 nm beam and an orthogonal 1560 nm beam, and then measuring light shifts due to just the 1529 nm beam. The polarisability of the ground state of rubidium is approximately the same at both of these wavelengths, so at equal intensity the two beams provide a near-spherical-shaped potential for atoms in the crossing. Using the two beams I could produce a sample of 2×10^5 atoms at 1 µK in a dense sphere at the crossing. The measurement then consisted of switching off the 1560 nm beam and measuring the absorption of the probe beam

within 100 µs before the atoms had time to move, thus measuring the light shifts due to just the 1529 nm beam. This measurement produced much narrower peaks than the previous measurement. The sequence is represented in Fig. 6.4.

I was able to obtain an estimated peak intensity of $4.5 \times 10^7\,\mathrm{W\,m^{-2}}$ of the 1529 nm laser. This value was obtained by fitting to the data, and does not agree well with power meter measurements. I measured about 270 mW next to the vacuum chamber, which corresponds to a peak intensity of $8.5 \times 10^7\,\mathrm{W\,m^{-2}}$ when focused down to 45 µm. I am not sure of the reason for this discrepancy, especially as the fitted light intensity resulting from the light shift measurement with just the 1560 nm laser corresponds well with the measured light power outside the vacuum chamber. Possibly it is simply due to an error in the measurement of the size of the beam waist.

The interferometer includes a fringe-counting system which enables precise control of the laser frequency by counting interferometer fringes and locking to a particular one. Instead of measuring light shifts as a function of intensity, I measured as a function of wavelength. This way the experimental sequence was exactly the same every run except for the wavelength of the 1529 nm laser which was controlled by a separate system (see Appendix A). The wavelength of the 1529 nm laser did not appear to affect the preparation of the atoms unless it was exactly resonant with one of the excited-state transistions, in which case it prevented the MOT from forming (the mechanism for this is unknown at this time).

6.2.2 Results

Figure 6.5 shows the calculated light shifts for light close to the excited-state transitions around 1529 nm. Due to technical limitations of our experiment[2], I was only able to measure with a probe frequency between 0 and about −1200 MHz, as such I was limited to measuring in the regions indicated by the blue boxes (a) and (b) in Fig. 6.5. The straight lines located in the region between the two blue boxes, labelled (c), appear to be an artifact of the calculation and are not completely understood at this time. Note that in this region there are 4 pairs of two lines with equal energies, or 8 lines in total. I attempted with several experiments but was unable to measure absorption of the probe beam in this region.

[2]The probe laser is offset-locked to a spectroscopically-referenced master laser, and at present this system is made in such a way it is only possible to blue-detune the probe laser about 40 MHz above resonance with the $F = 2 \rightarrow F' = 3$ transition. This is explained further in Appendix C.

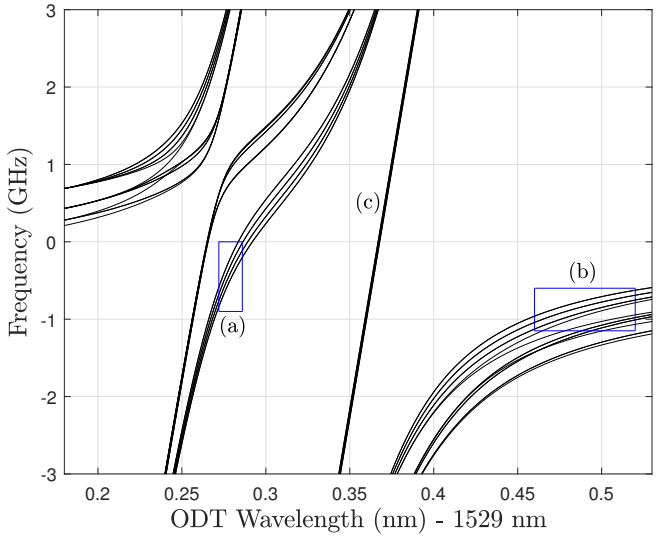

Figure 6.5. Predicted shifts of ^{87}Rb $5P_{3/2}$ energy levels due to light around 1529 nm, at an intensity of $4.5 \times 10^7\,\mathrm{W m^{-2}}$. The blue boxes show regions measured to compare the theory to experiment. Zero on the y-axis is the free-space energy of the $F = 3$ levels. The labels (a) and (b) indicate regions where the shifts were measured experimentally. (c) is explained in the text.

Data from the measurement corresponding to the box (a) in Fig. 6.5 is shown in Fig. 6.6. Four theory lines are shown in the figure, roughly corresponding to the $F' = 3, 2, 1, 0$ levels, in that order, from the top. There is good agreement between the $F' = 3$ line and the data, but with decreasing F' the absorption peaks become increasingly red (low frequency) relative to theory. The theory curves were calculated with $I = 4.5 \times 10^7\,\mathrm{W\,m^{-2}}$, because this intensity provides the best fit to the experimental data. The fitting was done "by hand", i.e. I observed by eye the difference between the data and theory, and adjusted the intensity of the light in the calculation such that the theory lines best match the data. The effect of changing the intensity of the light in the calculation is as follows: a higher intensity increases the gradient of the theory lines, and lower intensity decreases it. $4.5 \times 10^7\,\mathrm{W\,m^{-2}}$ is the best compromise between these two situations such that the gradients of the theory curves are as close as possible to those of the data curves, and the only intensity where any of the theory lines appears to match all of a particular row of data points. The uncertainty on this value of $4.5 \times 10^7\,\mathrm{W\,m^{-2}}$ is $\pm 0.2 \times 10^7\,\mathrm{W\,m^{-2}}$. This uncertainty was judged by changing the intensity of light in the calculation until the $F' = 3$ theory curve

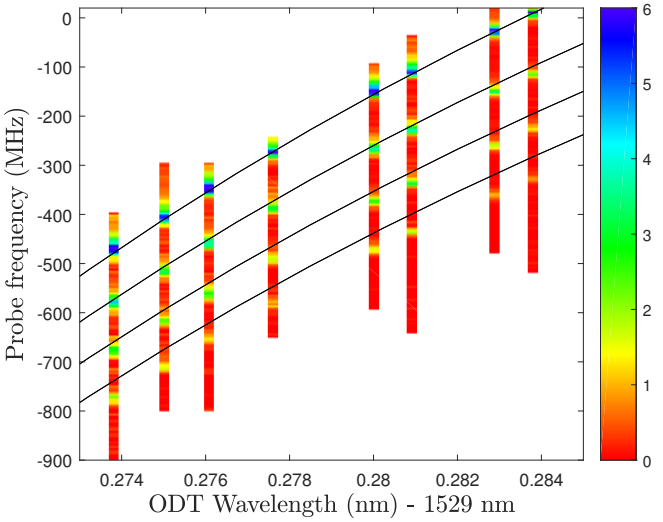

Figure 6.6. Absorption of the probe beam vs. frequency of the probe beam and frequency of trapping light, around 1529 nm. The uncertainty in wavelength ($\pm 2 \times 10^{-6}$ nm) is much narrower than the width of each column, which are shown wider for clarity. Theory curves are calculated for $I = 4.5 \times 10^7\,\mathrm{W\,m^{-2}}$. The shift of the ground states is about 100 kHz.

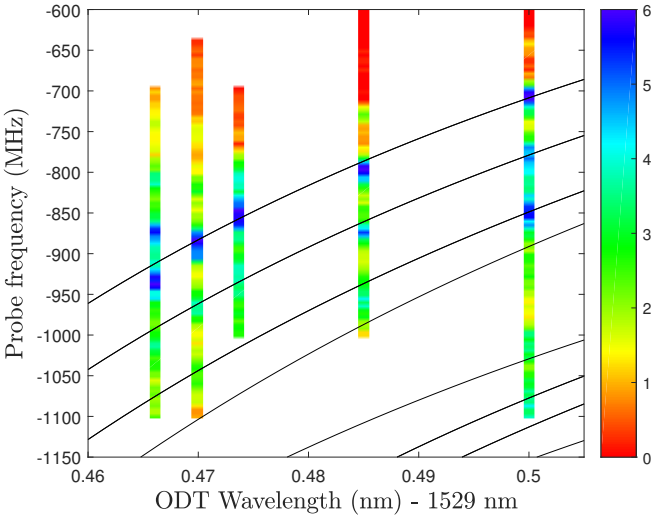

Figure 6.7. Absorption of the probe beam vs. frequency of the probe beam and frequency of trapping light, around 1529 nm.

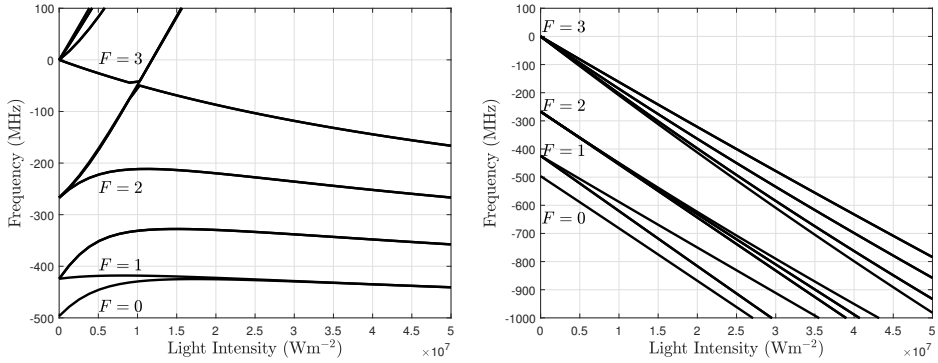

(a) $\lambda_2 = 1529.280$ nm. (b) $\lambda_2 = 1529.50$ nm.

Figure 6.8. Predicted shifts of ^{87}Rb $5P_{3/2}$ energy levels as a function of light intensity at the wavelength indicated in the respective caption. The shifts in (a) show a relatively weak dependence on intensity at 4.5×10^7 Wm^{-2}, compared to those in (b). Note the difference in scale on the y-axes. The text labels identify the eigenstates at zero intensity.

obviously no longer fit any of the data.

Data from the measurement corresponding to the box (b) in Fig. 6.5 is shown in Fig. 6.7. These data show larger and less systematic deviations from the theory than the data from the measurement corresponding to box (a), and the peaks appear to be broadened. The reason for this can be seen by looking at Fig. 6.8, which shows the light shifts vs. intensity at two different wavelengths corresponding to the two measurements described in this section. Fig. 6.8a shows that around 1529.280 nm (i.e. in the middle of Fig. 6.6) at the light intensity corresponding to the measurement the shifts have only a weak dependence on intensity, which is not the case for Fig. 6.8b. In other words, the measurement shown in Fig. 6.7 is much more sensitive to beam-pointing noise and finite-temperature effects. A given change in the position of the 1560 nm beam relative to the 1529 nm beam would change the equilibrium position of the atomic cloud, and have a bigger effect on the light shifts in Fig. 6.7 than the light shifts in Fig. 6.6, due to the stronger dependence of light shifts on light intensity in this wavelength region in Fig. 6.8b. The strong intensity-dependence also means the finite temperature of the atoms broadens the signal.

Uncertainty in calculated light shifts

Here I consider the effect of three factors which introduce uncertainty to the position of the calculated theory lines in Fig. 6.6: errors in the electric dipole matrix elements, inclusion of a limited number of atomic transitions, and a finite number of time steps in the calculation.

The calculation was performed using the electric dipole matrix elements of all the transitions shown in Fig. 5.1. However, using only the elements associated with the $5P_{3/2} \rightarrow 4D_{3/2,5/2}$ transitions makes a $\sim 100\,\mathrm{kHz}$ difference to the resulting calculated light shifts, and including levels up to $n = 10$ makes an even smaller difference, so the use of a finite number of transitions is thought to contribute at maximum a 100 kHz uncertainty to the calculation. The laser is so close to these transitions that these electric dipole matrix elements are the only ones to make a significant contribution to the light shifts. The number of time steps used was 200, as discussed in Section 5.2.6.

The electric dipole matrix elements are estimated to have an uncertainty of 0.5%, due to approximations made in their calculation [85]. Here I estimate errors in the calculated light shifts by assuming "worst-case" errors in the values of the electric dipole matrix elements. In the wavelength region of Fig. 6.6, the two nearby transitions "pull" the levels in opposite directions, so changing both of the corresponding matrix elements by $\pm 0.5\%$ (i.e. in the same direction by 0.5%) has very little effect on the positions of the theory lines. However changing one by $+0.5\%$ and the other by -0.5% makes the biggest possible difference to the calculation within the bounds of the uncertainty of the values of the matrix elements. Calculating the light shifts with this worst-case error in the dipole matrix elements shifts the theory curves by up to $\pm 14\,\mathrm{MHz}$. In any case changing the values of the matrix elements shifts all the theory curves by approximately the same amount, and does not change their relative positions. Changing the matrix elements by up to about 3% made it possible to fit any one of the theory curves to the data, but as far as I was able to determine never all four simultaneously.

Uncertainty in measured light shifts

Here I estimate the effect of two factors that might contribute to errors in the measured light shifts: An error in the probe beam frequency, or an external uncontrolled magnetic field.

Errors in the probe beam frequency are thought to be $< 1\,\mathrm{MHz}$. It was calibrated by measuring the frequencies of the $F = 2 \rightarrow F' = 3, 2, 1$ transitions in free space. Relative to the y-axis of Fig. 6.6 these occur at 0, -266, and -424 MHz, respectively. So the probe beam was demonstrated to be accurate to less

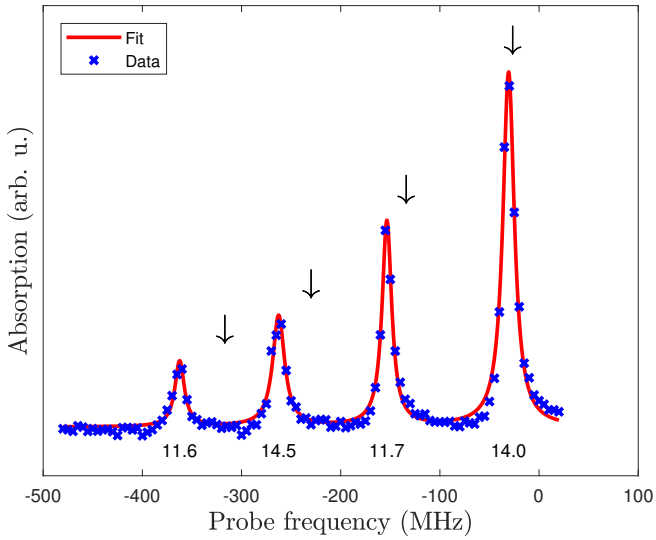

Figure 6.9. Probe absorption data with atoms subject to $4.5 \times 10^7\,\mathrm{W\,m^{-2}}$ of light at 1529.2829 nm (i.e. second column from the right in Fig. 6.6). The blue crosses are the mean of 4 measurements. The red line shows a sum of four Lorentzians fitted to the data. The numbers show the fitted FWHM of each peak in MHz. The arrows show the predicted position of each peak, after calibrating the light intensity to fit the largest peak.

than 1 MHz up to a detuning of -424 MHz. Beyond this, the frequency was not calibrated directly, but measurements were performed only when the laser frequency was stable, indicating that it was at the correct frequency (more about this in Appendix C).

Regarding the external magnetic field, after measuring these data it was realised an external field of at most 1 Gauss was accidentally applied during the measurement, at an angle of 45° relative to the polarisation of the 1529 nm light. This is enough to shift the atomic energy levels by ±2 MHz.

Agreement between data and theory

The combined total of estimated experimental and theoretical uncertainties is no more than 20 MHz. However, the measured difference between theory and experiment is up to about 45 MHz (see Fig. 6.9). This suggests that there is some effect occurring which is not accounted for by the theory.

Beyond electric dipole transitions

This section discusses some known effects which have been neglected by the theory of Chapter 5, and speculates whether or not they might be responsible for the theory-experiment discrepancy.

- **Imaginary part of polarisability**
  The calculation of Chapter 5 effectively calculates the real part of the polarisability of the atoms (associated with the phase shift of the applied light), and neglects the imaginary part (associated with scattering of the applied light, see e.g. Eq. (4.6)). This means we are ignoring the effect of atoms scattering light during the measurement. However, if this were the cause one would expect the error to depend strongly on wavelength, as the detuning of the 1529 nm laser spans one octave from the nearest transition, whereas the error appears to be constant as a function of wavelength.

- **Two-photon transitions**
  Two-photon transitions connect states of the same parity, so there is no nearby transition for two 1529 nm photons (1529 nm / 2 = 764.5 nm). However, the $5S_{1/2} \rightarrow 4D_{3/2}$ transition at 516.6 nm is very close to the energy of a 780 nm photon + a 1529 nm photon = 516.5 nm, and this transition is allowed under two-photon transition selection rules [96]. This could be checked by measuring the data/theory discrepancy as a function of the intensity of the 780 nm light.

- **Magnetic dipole transitions**
  The magnetic field of the light can interact with the magnetic dipole moment of the atom to induce magnetic dipole transitions [97] [98]. The selection rules for magnetic dipole transitions are that $\Delta n = 0$, $\Delta F = \pm 1, 0$, and $\Delta L = 0$. All such transitions in Rb are on the order of GHz or less, so the light is very far off-resonant for this kind of transition.

- **Electric quadrupole transitions**
  Electric quadrupole transitions connect states of the same parity [48], but there are no transitions between states of the same parity close to 1529 nm, so it seems unlikely the discrepancy is caused by quadrupole transitions. Ref. [99] describes how to calculate electric quadrupole matrix elements.

6.3 Conclusion

I have experimentally validated the light shift theory of Chapter 5 by predicting and measuring light shifts of the D_2 transition in ^{87}Rb caused by incident light nearly resonant with the $5P_{3/2} \rightarrow 4D_{3/2,5/2}$ transitions around 1529 nm.

An initial experiment agreed well with theory well beyond the regime of light shifts linear in light intensity, where there was strong mixing of the hyperfine energy levels and some levels were shifted more than 300 MHz from their unperturbed values, which is larger than the largest hyperfine splitting in the $5P_{3/2}$ manifold in ^{87}Rb. However due to an unstable trapping laser frequency, the precision of the measurement was limited to about ± 50 MHz.

A more precise measurement with larger light shifts showed a small but systematic discrepancy between theory and experiment. In this experiment some levels were shifted up to 1 GHz from their unperturbed values. The imprecision of the measurement is thought to be no more than ± 2 MHz, while there is a discrepancy of up to 45 MHz between the measured data and the theoretical energy levels. There are mainly two electric-dipole matrix elements contributing to the calculated light shifts in this regime, and each element has an estimated uncertainty of $\pm 0.5\%$. Assuming the absolute worst-case within the bounds of the uncertainties, i.e. that one element is wrong by $+0.5\%$ and the other is wrong by -0.5%, can explain up to 20 MHz of this discrepancy but no more.

Chapter 7

Bimodal Bose-Einstein condensate with tunable interactions

This chapter describes some theory and results from my time working at LENS in Florence. For one year from October 2014 I joined the group of Marco Fattori and spent one year with his group on their ^{39}K BEC experiment. My work during this year contributed to the publication of two papers, one in *Nature Physics* [100] and another in *Physical Review Letters* [101].

7.1 Introduction

The Florence ^{39}K BEC experiment was originally designed to study the potential of quantum effects for metrology (e.g. as described in [102] [103]). With this application in mind, the experiment was constructed with two interesting features: One feature is an optical potential that can split a single BEC between two coupled potential wells, with the barrier between them tunable, and the other feature is that the inter-atomic interaction strength (i.e. the atom-atom scattering length) can be scanned through zero. This interaction tuning is done with an external magnetic field. ^{39}K has accessible and wide Feshbach resonances which enable precise tuning of inter-atomic interactions with a relatively low magnetic field of around 350 G [104]. This ability to dynamically tune the interaction strength meant that this experiment was the first to condense ^{39}K without sympathetic cooling by exploiting control of the atomic scattering length during evaporation (for an example using sympathetic cooling see e.g.

[105]). The apparatus and procedure to reach BEC is already well-described in the PhD thesis of Giulia Semeghini [106] and summarised in [107].

The system presented here exhibits several interesting phenomena such as a quantum phase transition with metastability and hysteresis, and a macroscopic self-trapped phase. Similar two-mode many-body quantum systems have been published previously (for example in a spatially bimodal rudibium BEC [108] and in a system that couples two magnetic sublevels of a single rubidium BEC in [109]), but this is the first system to demonstrate full control over all of the relevant experimental variables. These are coupling between the two modes, the relative energy of the two modes, and interactions between the atoms.

Experiments with a tunable scattering length have been used for other interesting many-body physics such as the observation of bright solitons [110], the observation of non-equilibrium many-body phases in cesium [111], and the study of Anderson localisation [112].

7.2 Theory a of coherent two-mode quantum system

Here I derive a Hamiltonian describing the behaviour of a general two-mode quantum system with interactions. Despite the simplicity of the model it turns out to be very useful for describing phenomena observed in this experiment. Note this section follows [103] and some unpublished notes by Manuele Landini.

We can write the many-body Hamiltonian of interacting bosons in a potential as

$$H = \int \Psi^\dagger H_s \Psi d^3r + \frac{g}{2} \int \Psi^\dagger \Psi^\dagger \Psi \Psi d^3r \tag{7.1}$$

where the first term is the single-particle energy of the Hamiltonian, and the second term describes inter-particle interactions. g is a function of the s-wave scattering length a

$$\begin{aligned} H_s &= -\frac{\hbar^2}{2m}\nabla^2 + V \\ g &= \frac{4\pi\hbar^2 a}{m} \end{aligned} \tag{7.2}$$

and V is the external potential experienced by the atoms.

Now we make the two-mode approximation, where we assume that there are only two states available to the (noninteracting) atoms, a ground state ψ_g and an excited state ψ_e. The many-body wavefunction can now be written

$$\Psi = \psi_g a_g + \psi_e a_e \tag{7.3}$$

where a_g (a_e) is the annihilation operator for an atom in the ground (excited) state. The Hamiltonian can now be written

$$\begin{aligned} H = & \tfrac{1}{2}(\epsilon_e + \epsilon_g)(a_e^\dagger a_e + a_g^\dagger a_g) \\ & + \tfrac{1}{2}(\epsilon_e - \epsilon_g)(a_e^\dagger a_e - a_g^\dagger a_g) \\ & + \kappa_{ee} a_e^\dagger a_e^\dagger a_e a_e + \kappa_{gg} a_g^\dagger a_g^\dagger a_g a_g \\ & + \kappa_{eg}(a_e^\dagger a_e^\dagger a_g a_g + a_g^\dagger a_g^\dagger a_e a_e \\ & + 4 a_e^\dagger a_g^\dagger a_e a_g) \end{aligned} \tag{7.4}$$

where

$$\begin{aligned} \epsilon_a &= \int \psi_a H_s \psi_a, \\ \kappa_{ab} &= \frac{g}{2} \int |\psi_a|^2 |\psi_b|^2 \end{aligned} \tag{7.5}$$

for $a, b \in \{g, e\}$. One important parameter in this system is the energy difference between the ground and excited states. We define

$$\epsilon = \epsilon_e - \epsilon_g. \tag{7.6}$$

If we assume our potential V is one-dimensional with two local minima, we can define left- and right-hand states

$$\psi_{l,r} = \tfrac{1}{\sqrt{2}}(\psi_g \pm \psi_e) \tag{7.7}$$

with corresponding operators

$$a_{l,r} = \tfrac{1}{\sqrt{2}}(a_g \pm a_e). \tag{7.8}$$

With sufficiently small overlap between these states, the absolute squares of the even and odd wave functions

$$|\psi_{g,e}|^2 = \tfrac{1}{2}(|\psi_l|^2 + |\psi_r|^2 \pm \psi_l \psi_r) \tag{7.9}$$

are approximately equal, i.e. the overlap $\psi_l \psi_r$ can be ignored. This means we can write

$$\kappa_{ee} \approx \kappa_{gg} \approx \kappa_{eg} \equiv \kappa \tag{7.10}$$

We are interested in the dynamics of the system, so we can ignore terms that are a function of the conserved total atom number ($\hat{N} = a_e^\dagger a_e + a_g^\dagger a_g$). With these substitutions and simplifications, the Hamiltonian 7.4 becomes

$$H = -\frac{\epsilon}{2}(a_l^\dagger a_r + a_r^\dagger a_l) - 4\kappa(a_l^\dagger a_l a_r^\dagger a_r). \tag{7.11}$$

We can make another approximation to the Hamiltonian to more easily understand the behaviour of this system. The quantity $\langle a_l^\dagger a_l \rangle$ is equal to the mean number of atoms in the left well. We can make a mean-field approximation and say $a_l \approx \sqrt{N_l} e^{i\phi_l}$, where N_l is the number of atoms in the left well, and ϕ_l the phase (equivalently for the right well). Letting $\phi = \phi_l - \phi_r$, $\Lambda = N\kappa/\epsilon$, and parameterising the imbalance as $z = (N_l - N_r)/N$, where $N = N_l + N_r$, the Hamiltonian 7.11 becomes

$$H_{MF} = \frac{H}{\epsilon N} = -\sqrt{1-z^2}\cos\phi - \frac{\Lambda}{2}z^2, \tag{7.12}$$

where the system is normalised by the number of atoms and energy is scaled relative to ϵ, the difference between the ground and first excited state. To simulate the system dynamics we can solve Hamilton's equations

$$\begin{aligned} \frac{\partial \phi}{\partial t} &= -\frac{\partial H_{MF}}{\partial z} = -\frac{z}{\sqrt{1-z^2}}\cos\phi + z\Lambda \\ \frac{\partial z}{\partial t} &= \frac{\partial H_{MF}}{\partial \phi} = \sqrt{1-z^2}\sin\phi \end{aligned} \tag{7.13}$$

for z and ϕ, both observables we can also measure. Despite all the simplifications, this Hamiltonian turns out to be remarkably accurate in predicting much of the possible behaviour of the double well.

7.3 Experimental apparatus

Now I describe the experimental apparatus used to create a system well-approximated by the theory in the previous section. The laser beam configuration used to create the double-well potential is shown in Fig. 7.1. There are two interfering pairs of lasers at 1064 nm and 532 nm, both propagating nearly vertically but at an angle of ± 0.05 radians relative to vertical. The interference of the four beams creates two collinear one-dimensional optical lattices in the horizontal x-direction, the depth of which can be independently controlled. The lasers are arranged in this way to make the lattice have a large period, and the number of atoms in each well can be more easily resolved than if the lattice beams

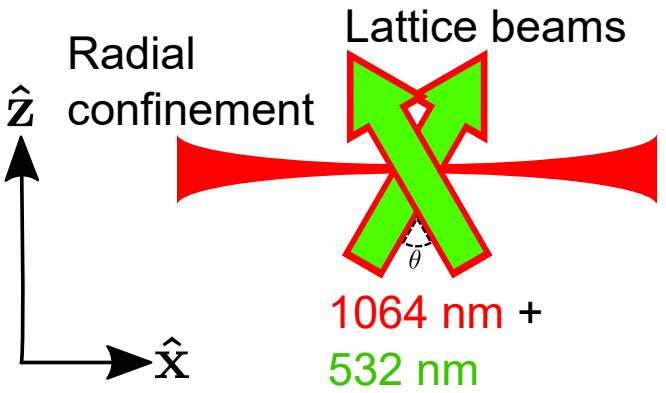

Figure 7.1. Diagram showing the 5 of the 6 optical beams used to create the tuneable 1D lattice potential. Not shown is an additional "cross" beam perpendicular to the radial confinement beam, propagating into the page in the $\hat{\mathbf{y}}$-direction, which is used to load a single site in the lattice.

were counter-propagating. The system can be used as an interferometer, and the large period increases the sensitivity of the interferometer to potential energy gradients such as gravity gradients, magnetic field gradients, etc. The infrared "primary" lattice at 1064 nm has a period of 10 µm, and the green "secondary" lattice at 532 nm has a period of 5 µm. The height of the central barrier is controlled by changing the power of the secondary lattice. An orthogonal beam provides radial confinement perpendicular to the x-direction, and another "cross" beam used during evaporation to BEC allows us to load atoms into a single site of the primary lattice.

Fig. 7.2 shows one site of the lattice and the wavefunctions of the ground and first excited states of a trapped atom. From this diagram we can see that the normal (no interactions) ground state is a wavefunction with equal amplitude on each side of the double well.

We can also control the relative phase of the two lattices, which enables us to control the relative depths of the two sites of the double-well as shown in Fig. 7.3. This was used to load with a non-zero difference between the atom number in each well: we can load with imbalanced depths of the two wells, then quickly switch the phase between the lattices back to zero, such that the well depths are the same but with unequal atom number.

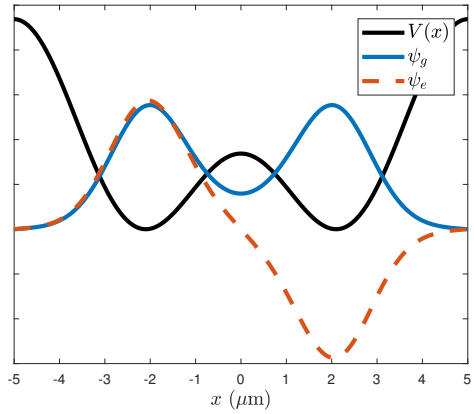

Figure 7.2. Representation of the double-well potential, which is the sum of the primary and secondary lattices (black), and wavefunctions of the ground state (blue) and first excited state (green dashes).

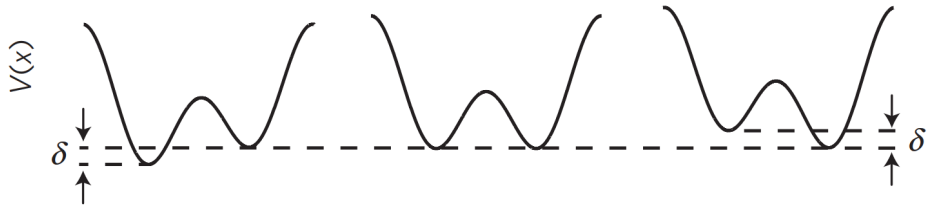

Figure 7.3. Lattice potential as a function of phase difference between the lattice beams. We can change the relative phase of the lattice beams to induce a small imbalance δ in the depth of the two wells.

Fig. 7.4 shows the lowest three eigenenergies of the potential for different heights of the barrier, or intensities of the green lattice. For sufficiently low excitation and sufficiently high barrier, this justifies the two-mode approximation made in the previous section.

7.4 Observables

To perform measurements in this experiment we used standard absorption imaging, as explained in Chapter 3, with which we could destructively measure two observables: the population imbalance between the two BECs z and their relative phase ϕ.

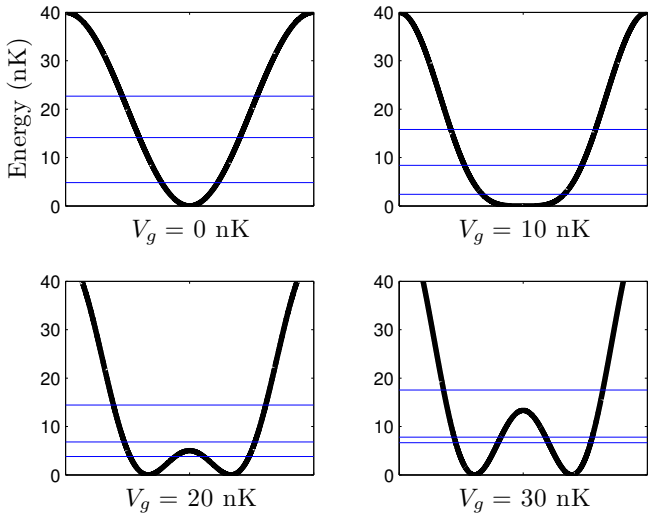

Figure 7.4. The lowest three eigenenergies (blue) for a non-interacting atom in a potential (black). The amplitude of the primary lattice is constant, while the amplitude of the secondary lattice V_g is given below each subfigure. The lowest two eigenenergies approach degeneracy as the amplitude of the secondary lattice becomes higher.

7.4.1 Imbalance z

A typical experimental sequence involves loading the double-well and then waiting some time for the system to evolve, the amount of time depending on the experiment. At the end of the experimental sequence, we increase the power of the green lattice to effectively switch off tunneling between the two well sites, and then turn off the radial confining potential but leave the lattice on, such that the atom clouds expand radially but the imbalance stays the same. The purpose of the expansion is to reduce the density of the clouds, otherwise the density would be too high to quantitatively measure the number of atoms in each well. After the expansion we perform a standard absorption image sequence.

To measure z we integrate images of the expanded cloud in the radial direction, and then fit a double Gaussian function to the two peaks in the one-dimensional data, as shown in Fig. 7.5. The lattice is one-dimensional, so in the direction perpendicular to the k-vector of the lattice the clouds are Gaussian-shaped due to the harmonic confinement of the radial dipole trap, thus integrating in this direction does not lose any information.

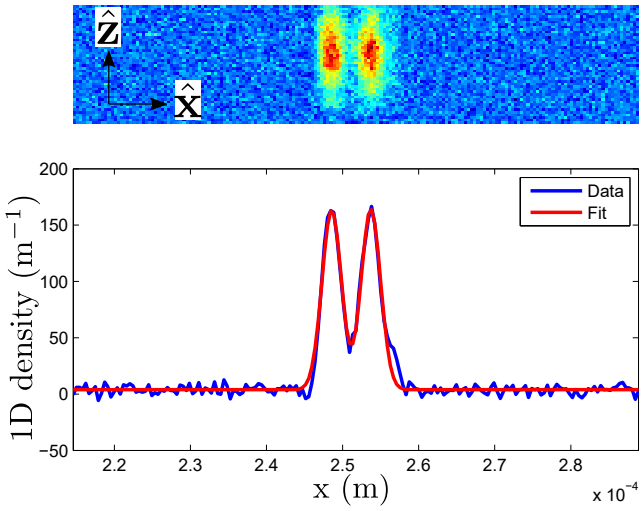

Figure 7.5. Data and fit of a measurement of population imbalance z. The top figure shows a typical absorption image of the bimodal BEC after the radial expansion, with the experiment axes labelled. The bottom figure shows data (blue) resulting from integrating the top image in the $\hat{\mathbf{z}}$-direction. The red line is a fit of a double-Gaussian function to the data.

7.4.2 Phase ϕ

For measuring the phase difference between the two trapped clouds, rather than letting the clouds expand in the lattice after an experiment we simply switch all the optical beams off simultaneously. This lets the two atom clouds freely expand and interfere. We then integrate the data to one dimension, and then fit the data to a function to extract the phase. Here I will derive the function which we fit to the interfering clouds to measure the phase.

There is a BEC in each well, and the wavefunction of each individual cloud is approximately that of a particle in the ground state of a harmonic oscillator. In the case of non-interacting atoms, the wavefunction of each cloud is given by

$$\begin{aligned} \psi_i &= C_i \times \exp(-x^2/4\sigma_i^2) \\ C_i &= \sqrt{\frac{N_i}{\sqrt{2\pi}\sigma_i}} \end{aligned} \tag{7.14}$$

where N_i is the number of atoms in the i^{th} well (i.e. so $\int_{-\infty}^{\infty} |\psi_i|^2 dx = N_i$, not 1), σ is the Gaussian half-width of the cloud (given by the trap depth), and x is

position. The wavefunction for the total system before the expansion is

$$\psi_{total}(x, t = 0) = \psi_1(x + d) + \psi_2(x - d)e^{i\phi} \tag{7.15}$$

where $2d$ is the distance between the well centres, the numerical subscript is an index for each well, and ϕ is the phase that we want to measure. First of all we Fourier transform (the spatial coordinate)

$$\Psi(k, t = 0) = \mathcal{F}[\psi(x)] = \sqrt{2}C \times \exp(-k^2\sigma^2) \tag{7.16}$$

where k is the spatial frequency coordinate. Then apply the time evolution operator (with the free-space Hamiltonian)

$$\begin{aligned}\Psi(k, t) &= \Psi(k, 0) \times \exp\left(-\frac{i}{\hbar}Ht\right) \\ &= \sqrt{2}C \times \exp\left(-k^2\sigma^2\right) \times \exp\left(-\frac{i}{\hbar}\frac{\hbar^2k^2}{2m}t\right)\end{aligned} \tag{7.17}$$

where m is the mass of one atom. Then inverse Fourier transform back to real space

$$\psi(x, t) = \frac{\sigma C}{\sqrt{i\alpha + \sigma^2}} \times \exp\left(-\frac{x^2}{4(i\alpha + \sigma^2)}\right) \tag{7.18}$$

where $\alpha = \hbar t/2m$. Plugging this into eq. 7.15, and taking the modulus squared to get density, which is what is actually measured, we get

$$\begin{aligned}\rho(x, t) &= |\psi_{total}(x, t)|^2 \\ &= \exp\left(-\frac{\sigma^2(x^2 + d^2)}{2(\sigma^4 + \alpha^2)}\right) \times \\ &\Bigg[(C_1^2 + C_2^2)\cosh\left(\frac{xd\sigma^2}{\sigma^4 + \alpha^2}\right) + \\ &(C_1^2 - C_2^2)\sinh\left(\frac{xd\sigma^2}{\sigma^4 + \alpha^2}\right) + \\ &2C_1C_2\cos\left(\phi - \frac{xd\alpha}{2(\sigma^4 + \alpha^2)}\right)\Bigg]\end{aligned} \tag{7.19}$$

This function is fitted to some example data in Fig. 7.6.

Rather than thinking of the number of atoms in each well, we can instead parameterise the system with the total atom number $N = N_1 + N_2$, and the imbalance $z = \frac{N_1 - N_2}{N_1 + N_2}$. This means

$$\begin{aligned}C_1^2 &= \frac{N(1 + z)}{2\sigma\sqrt{2\pi}} \\ C_2^2 &= \frac{N(1 - z)}{2\sigma\sqrt{2\pi}}\end{aligned} \tag{7.20}$$

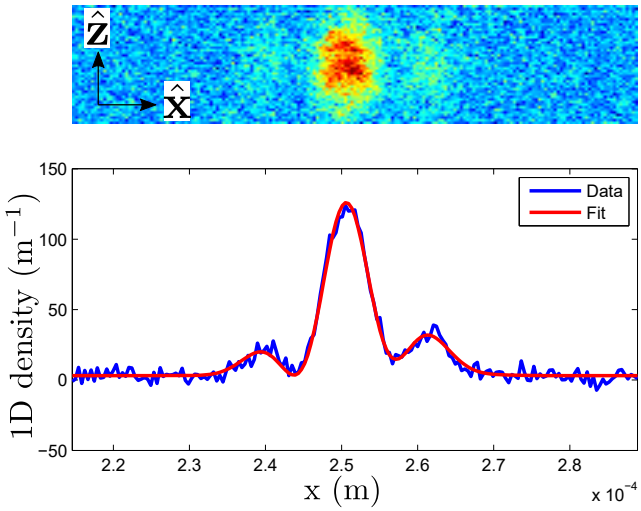

Figure 7.6. Data and fit of interfering clouds used for a phase measurement. The top figure shows a typical absorption image of two interfering BECs after release from the optical potential. The bottom figure shows the top figure integrated in the $\hat{\mathbf{z}}$-direction. The blue line is the data, and the red line a fit of Eq. (7.19) to the data.

We can then fit eq. 7.19 to data to find N, z, and ϕ. The other parameters t, d, and σ are known. Although we can in principle simultaneously obtain both z and ϕ from this measurement, it tended to not work so well for $z \sim \pm 1$ as the cloud is more dilute than in the measurement procedure for z, so a small peak is more easily buried in the noise.

7.5 Dynamics of the double well

Now I will describe the three regimes of behaviour of the double-well BEC, defined by the value of Λ in Eq. (7.12), which in practice is controlled by changing the scattering length of the atoms with an external magnetic field. In the phase plots that follow, shown trajectories were calculated by numerically solving Eq. (7.13) with initial condition $z = z_0$ (shown in each figure) and $\phi = 0$.

7.5.1 $\Lambda = 0$ Rabi oscillations

Figure 7.7 shows predicted and measured Rabi oscillations of z and ϕ in the double well. That is, oscillations with no inter-atomic interactions. For low

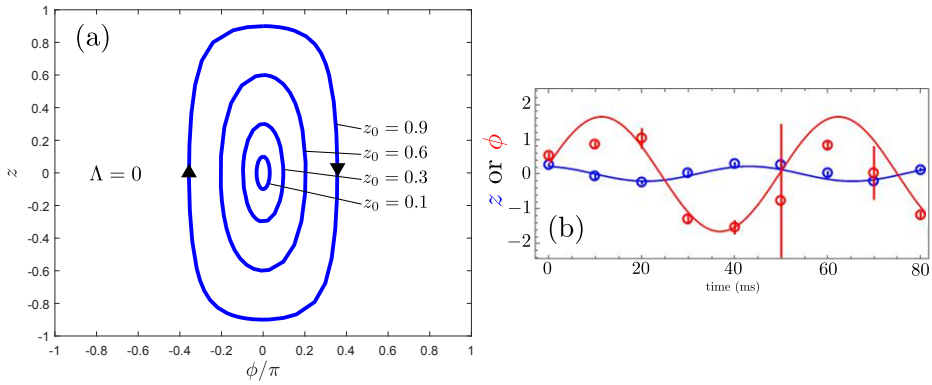

Figure 7.7. (a) Phase plots of the double well with $\Lambda = 0$. z_0 indicates the initial imbalance. For small initial z the system undergoes harmonic oscillations, however for large initial z the oscillations become less harmonic. Obtained by numerically solving Eq. (7.13). (b) Experimental data. The points show measurements with error bars representing the uncertainty in each measurement, and the lines are fits to the data points.

initial z the oscillations of both variables are harmonic, while for larger initial z, the oscillations of ϕ become anharmonic. For every initial z the system still undergoes periodic oscillations in both z and ϕ.

7.5.2 $\Lambda < -1$ Parity-symmetry-breaking quantum phase transition

This section is a summary of results published in [100].

For sufficiently strong negative (attractive) interactions the double well undergoes a fundamental change in the symmetry of the ground state. An example of this is shown in Fig. 7.8, which shows phase plots calculated with Eq. (7.12) for $\Lambda = -1.1$. In this case, if the initial imbalance z_0 is around ± 0.4 there is no dynamics, i.e. no evolution of z or ϕ. This means the ground state is no longer uniquely that with $z = 0$, but there are now two degenerate ground states with $z \approx \pm 0.4$.

The transition from a symmetric to two degenerate asymmetric ground states as a function of the interaction strength is a second-order parity-symmetry-breaking quantum phase transition (QPT). It is second-order as the first deriva-

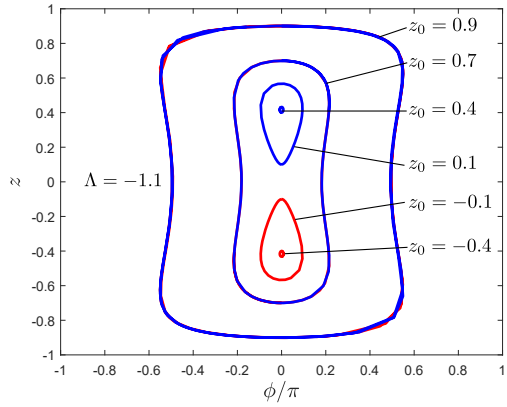

Figure 7.8. Phase plot of Eq. (7.12) with $\Lambda = -1.1$. Notice that for $z_0 \approx \pm 0.4$ there is no dynamics, meaning these are now ground states.

tive of the "order parameter" (z in the ground state) is discontinuous as a function of the "control parameter" (Λ in this case). A first-order phase transition is discontinuous in the order parameter directly [113]. The symmetry-breaking comes from the fact that with an interaction strength above the critical value the system has parity-symmetry, i.e. the ground state is symmetric. This symmetry is lost below the critical interaction strength, and the system must 'choose' one side or the other as the ground state. Which side it chooses depends on small random imbalances of the optical potential. As this transition occurs at zero temperature as a result of varying a non-thermal parameter, it is a quantum phase transition [114].

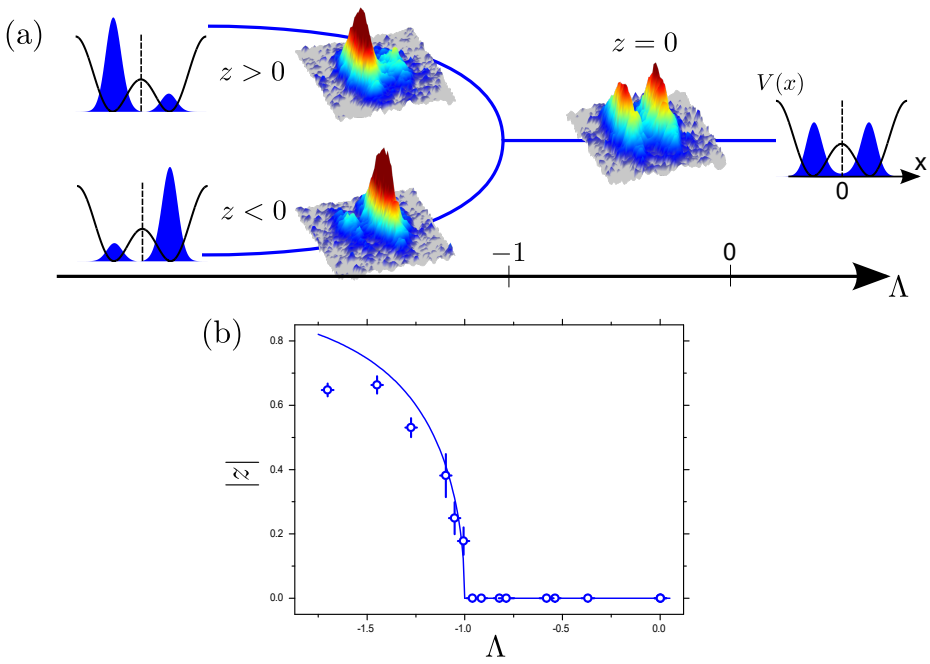

Figure 7.9. (a) The ultracold atomic gas (ground state density indicated by blue Gaussians) is trapped in a double-well potential (black line). Tuning the interatomic interaction strength Λ to large negative values, the ground state of the system goes from a symmetric state to two degenerate asymmetric states. The system undergoes a second-order QPT where the spatial parity symmetry, that is, reflection with respect to the vertical dotted line (symmetry axis), is broken. (b) Measured absolute value of the order parameter z in the ground state as a function of the control parameter Λ in a balanced double well. Error bars are three times the standard deviation. The solid line is the fitting function (see supplementary material of [100]).

Fig. 7.9a demonstrates the behaviour of this system as a function of $\Lambda < 0$. Above the critical value of Λ the ground state is a symmetric state, with an equal number of atoms on either side of the central barrier. Below the critical value, the ground state is one of two degenerate asymmetric states. Fig. 7.9b shows experimental measurements, which agree with theory within experimental error down to about $\Lambda = -1.2$. These data were measured by loading just the primary optical lattice with interaction strength Λ, i.e. loading the double well with zero barrier/zero intensity of the secondary lattice, then slowly raising the barrier so as minimise excitations, then finally measuring z as described above.

In this regime of strong attactive interactions the system exhibits further interesting behaviour. Below the critical interaction strength, the asymmetric ground states are metastable. To demonstrate this, we control the relative height of the two sides of the double well (recall Fig. 7.3). By changing the phase between the two lattices, one side of the double well can be raised above the other, the energy difference between the two minima is labelled as δ.

The hysteresis is shown in Fig. 7.10. These data were obtained by loading atoms in the absolute ground state with a non-zero δ, where the majority of atoms are in the lower-energy well. The lattice was then shifted so that this well becomes the higher-energy well. For interactions below the critical value, the atoms stay in this same well up to some δ with opposite sign from the initial δ, showing that the system is in a metastable state.

7.5.3 $\Lambda > 0$ Plasma oscillations and macroscopic quantum self-trapping

This section is a summary of results published in [101].

The third studied regime of behaviour of the double well is that with $\Lambda > 0$, i.e. positive or repulsive interactions. For sufficiently high Λ two distinct behaviours are possible depending on the initial imbalance z_0. A phase plot of dynamics with $\Lambda = 12$ is shown in Fig. 7.11a. For small z_0, the system undergoes periodic oscillations in z and ϕ, but with the frequency decreasing as z_0 increases. As z_0 crosses some critical value the nature of the oscillations changes suddenly, and the system becomes trapped in a metastable state with a monotonically increasing phase and a z that oscillates around some non-zero value. This phenomenon is known as macroscopic quantum self-trapping (MQST) [115]. Figures 7.11b and 7.11c show measured experimental data in the so-called plasma oscillation and MQST regimes, respectively.

Figure 7.12 shows the frequency of oscillation vs. z_0 for $\Lambda \approx 18$. The blue and red dots are fits to experimental data, and the black line a fit using Eq. (7.12). The frequency of the oscillations decreases to zero with increasing z_0, then the system suddenly changes to the MQST regime, where the oscillation frequency increases quickly with increasing z_0. Note that this is not a phase transition, as the ground state is still the state with $z = 0$.

The double well system with positive (repulsive) interactions is a kind of generalised Josephson junction (a 'Bosonic Josephson junction' (BJJ)), able to access dynamic regimes not possible with the analogous superconducting Josephson

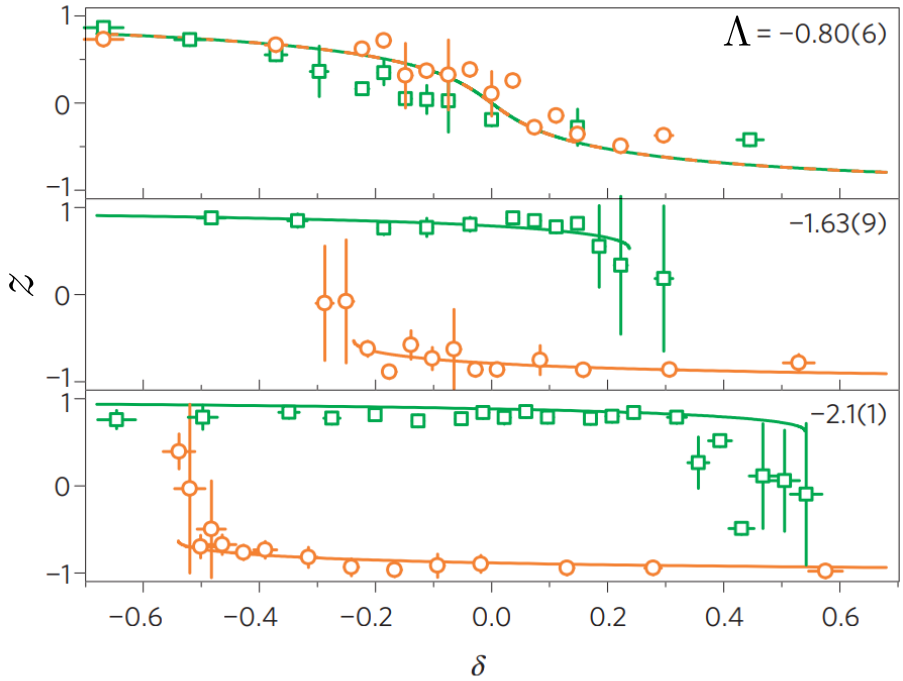

Figure 7.10. Atomic imbalance z as a function of well imbalance δ. Green squares (orange dots) are obtained by cooling the gas to its ground state at negative (positive) δ and then increasing (decreasing) δ to the indicated value in 500 ms and waiting 10 ms before the measuring of the imbalance. Lines are theoretical predictions for the imbalance of the ground and the metastable states using a Ginzburg–Landau model (see Supplementary Information of [100]).

junction (SJJ). For example, the symmetrical oscillations in this regime, so-called plasma oscillations, are analogous to the ac Josephson effect in the SJJ [116], and applying a differential energy between the wells δ is equivalent to applying a dc voltage to the SJJ. The MQST oscillations have no such analogue [115]. With the BJJ it is possible to control variables that are not controllable in the SJJ. For example in the BJJ the coupling between the wells can be changed, which would amount to dynamic control of the separation between the two superconducting bulks in the SJJ.

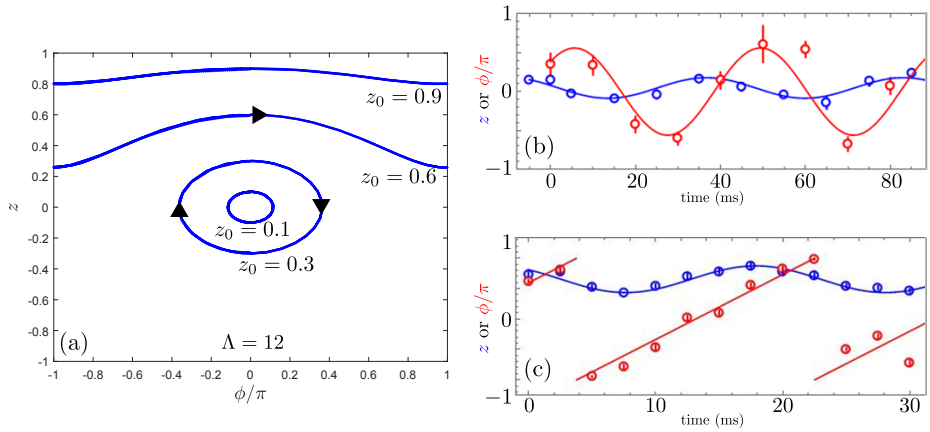

Figure 7.11. (a) Phase plot with $\Lambda = 12$ for different z_0, calculated using Eq. (7.13). (b) Experimental data in the plasma oscillation regime. (c) Experimental data in the MQST regime, note how z oscillates about some non-zero value while ϕ increases linearly.

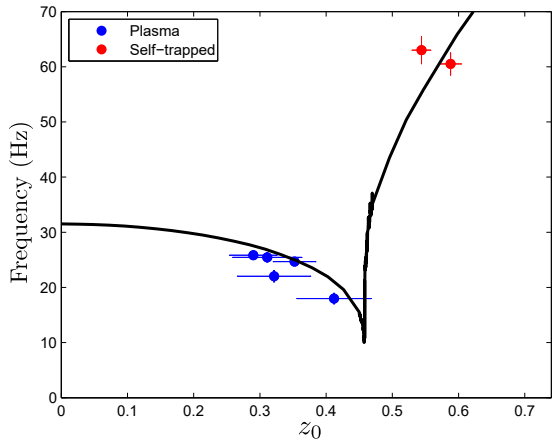

Figure 7.12. Experimental data with $\Lambda \approx 18$ showing the two kinds of behaviour possible in this regime, depending on the initial value of z. Plasma oscillations are where z and ϕ oscillate symmetrically about 0. Self-trapping refers to the system being "trapped" in a non-equilibrium state where z undergoes fast oscillations about a non-zero mean value, while ϕ increases linearly. The black line is a fit using Eq. (7.13) with Λ as a fitting parameter. The noise around $z_0 \approx 0.5$ is due to the numerical fitting procedure.

Chapter 8

Conclusion & outlook

8.1 Conclusion

This thesis presented a theoretical and experimental study of some physical phenomena observable with ultracold atoms in optical dipole traps. The experiments were performed in two cold atom laboratories, one at ICFO in Barcelona and the other at LENS in Florence. There is background material describing the most common techniques for laser cooling of neutral atoms, and a description of optical dipole traps, including some techniques exploiting light shifts to characterise them.

The main result of the thesis is a theoretical framework that exploits Floquet's theorem to calculate atomic light shifts, and an experiment demonstrating that the theory is valid for large light shifts well beyond the range of the usual perturbation theory-based approach. Intriguingly, at very large shifts there is a small but systematic disagreement between the theory and experimental data. This disagreement is outside the range of known uncertainties and was not able to be explained for this thesis.

A secondary result of the thesis is the theory and experimental characterisation of a two-mode Bose-Einstein condensate with tunable interactions. The behaviour of this system is explored in three distinct regimes: with attractive, zero, or repulsive inter-atomic interactions. With attractive interactions the system exhibits a second-order quantum phase transition, with some interesting hysteretic properties. With repulsive interactions the system shows behaviour analogous to a superconducting Josephson junction.

In four appendices the thesis presents background technical details of the two experiments. There is a description and characterisation of a Mach-Zehnder interferometer used as a laser frequency stability transfer lock, a block diagram-level description of the control system developed for the Barcelona experiment, an overview of phase-contrast imaging, and finally a description of a numerical model developed to understand the detection limits of the absorption imaging in the Florence experiment.

8.2 Outlook

While this thesis presented a method to calculate light shifts beyond the standard perturbation theory-based method, it also presented data showing a small discrepancy between the theory and a measurement. This calculation method is potentially useful for measuring ratios of electric-dipole transition matrix elements. Accurate measurement of these matrix elements would be useful for many areas of physics, so it would be interesting to find the reason for this discrepancy. Further experiments could be performed to determine whether the discrepancy is due to an experimental error or due to the theory not including some effect that becomes significant at these large light shifts. Further experiments could measure the shifts as a function of more parameters, to see if the discrepancy can be amplified or decreased, for example measuring as a function of probe beam power could eliminate the probe beam as the source; measuring as a function of trapping light intensity could determine if there is a linear or quadratic dependence of the discrepancy on light intensity, which could give a clue as to its origin. Other parameters not checked during my experiments were the ellipticity of the trapping light, and the light shifts measured with a positively detuned probe beam. Changing the sign of the probe beam could find some systematic experimental errors, for example if the discrepancy changes sign with the detuning this might indicate some technical problem with the probe beam tuning.

In the case that the discrepancy is real, and the theory of Chapter 5 is insufficient to explain the experimental data, it would be interesting to perform more theoretical work to determine (a) what is the physical mechanism causing the discrepancy, and (b) whether or not this can be included in the calculation. As mentioned earlier, if for example the cause is quadrupole transitions, this should be easy enough to include in the calculation, and perhaps could even serve as a technique to measure the matrix elements of these transitions. However if the cause is something like scattering on the excited-state transition, this might be more complicated to include in the theory, as it is dissipative and might require a master equation approach.

Appendix A

Laser stability transfer with a temperature-controlled fibre interferometer

The main source of experimental uncertainty in the initial light shift experiments of Chapter 6 was the frequency instability of the 1529 nm laser. Using the spectroscopic lock system developed in the group [117], we could lock this laser 80 MHz from an excited state resonance, but to perform the light shift experiments I needed to scan the laser from being resonant with an excited-state transition to being a few GHz away with high accuracy and resolution. To perform this broadband stabilisation I built a Mach-Zehnder interferometer (MZI) to act as a "transfer lock." That is, to transfer stability from a spectroscopically-referenced 1560 nm laser to the 1529 nm laser. The interferometer consists of a temperature-stabilised unequal arm length all-fibre optical MZI. The two wavelengths are in-coupled on different sides of the first beamsplitter, and each wavelength is amplitude-modulated at a different frequency to enable separation of the respective signals at the output. The 1560 nm laser is frequency-stabilised spectroscopically, so the output signal is in principle limited by the frequency stabilisation and the stability of the relative arm lengths of the interferometer. So long as the interferometer is vibration-isolated, the relative arm length only changes if the temperature changes. Thus the signal from the 1560 nm laser can be used as a precise thermometer of the fibre, and a PI feedback system controls a resistive heater to control the temperature of the fibre. Once the temperature of the fibre is stable, the output of the 1529 nm signal will only change due to a change in frequency of this laser and thus this signal can be used to control

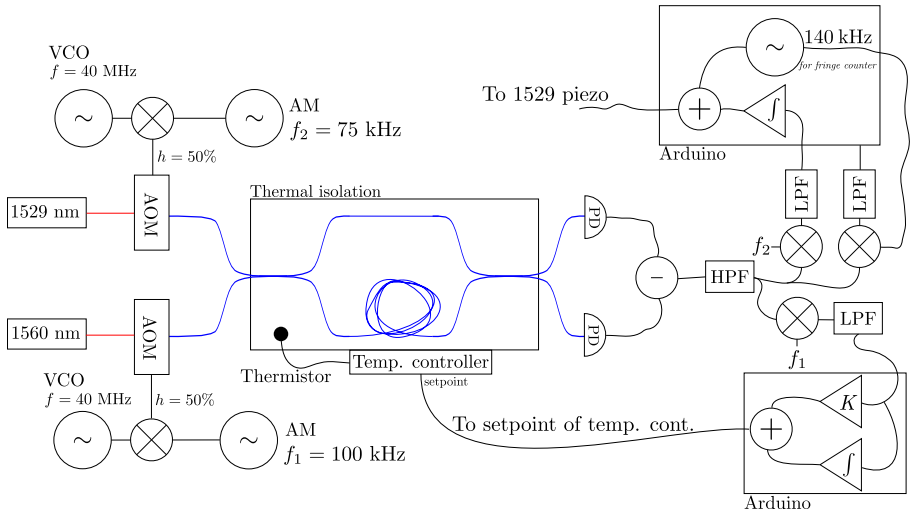

Figure A.1. Schematic of MZI used to control the frequency of the 1529 nm laser. Red lines indicate free-space light, blue lines fibre-coupled light, and black lines electronic signals. Both the 1560 nm and 1529 nm laser are amplitude-modulated by AOMs and then enter at the first beamsplitter. Both outputs are detected and subtracted to obtain a differential signal. The signals are separated by demodulation at their respective modulation frequencies. The 1560 nm signal is used to control the temperature of everything inside the thermal isolation, and the 1529 nm signal is used to measure and control the frequency of that laser. AM = amplitude modulation. HPF/LPF = high-pass/low-pass filter. VCO = voltage-controlled oscillator. PD = photodiode. All filters are active third-order filters with the multiple feedback architecture and a cutoff/cuton frequency of 1 kHz.

the laser frequency. I also implemented a system to scan the laser frequency and digitally count interferometer fringes. In this way the frequency of the laser can be scanned an integer number of fringes and locked on any particular fringe. A schematic of the interferometer is shown in Fig. A.1.

This idea was based on a simliar device built in the group [118]. A very similar system to the interferometer presented here has been published [119], but the interferometer described here is at least twice as stable and demonstrates integration of a fringe counter. The stability of the two systems is compared in Fig. A.6.

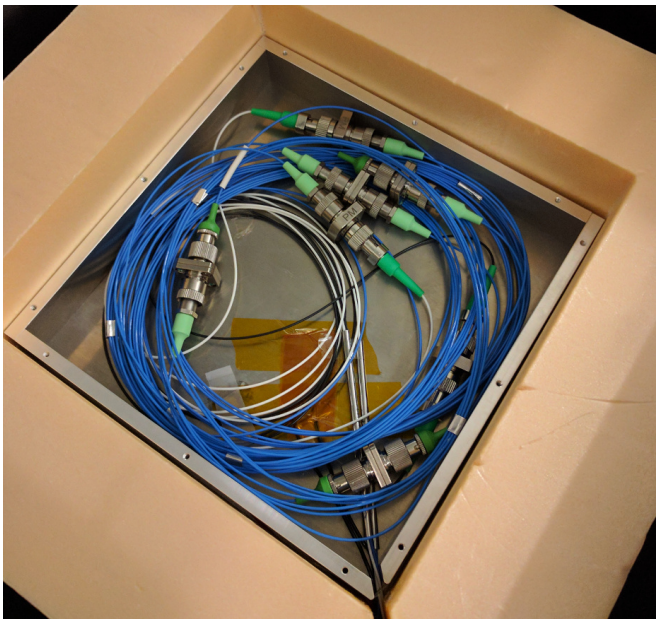

Figure A.2. Photo of inside the thermal isolation. The resistive heater is underneath the aluminium base, and the thermistor is taped to the top side of the base. The aluminium box evenly distributes heat around the fibre, and the foam insulates the aluminium from the outside environment. The small opening in the corner closest to the camera allows entry of fibres and wires. Completely blocking this opening would probably improve performance of the interferometer by eliminating air currents.

A.1 Temperature control with an Arduino

The temperature of the interferometer is controlled in two ways: there is rough control using an HTC-1500 temperature controller that uses a thermistor as a sensor and a resistive heater as an actuator. Fine control of the temperature is done using the interferometer output signal from the 1560 nm laser. This signal is fed to an Arduino which is programmed to act as a PI feedback controller. An Arduino was used instead of analogue electronics as the gain of the feedback needed to be very low to achieve stability. The output from the Arduino is then added to the setpoint of the HTC controller, with the correct polarity such that it opposes changes in temperature. Signal I/O is performed using a Digilent Analog Shield, a 16-bit 100 kS/s analog-digital interface made especially for use with Arduino Unos [120]. The modulation frequency of the 1560 nm laser amplitude

is 100 kHz.

A.2 Frequency control and fringe counting with an Arduino

Frequency control of the 1529 nm laser (an NKT Photonics Koheras Adjustik low-noise laser diode) was done by feeding the interferometer signal to a pure integrator implemented in firmware in an Arduino (with the same Analog Shield I/O interface), and feeding that to the piezo controller of the laser. Also implemented in the Arduino is a digital fringe counter (the method is described in [121]) to count interferometer fringes and keep track of the laser frequency. The Arduino can switch between these two functions on command. The fringe counter can lock the laser to a particular fringe - which can be manually set to, for example, an atomic resonance - and then programmed to count and lock an exact number of fringes away. The fringe counter can be used to quickly scan the laser over at least 20 GHz with precise knowledge of the number of fringes from fringe zero. The frequency of fringe zero could be known with a few MHz accuracy using atomic spectroscopy, described below. The modulation frequency of the 1529 nm laser amplitude was 75 kHz.

The piezo could be used to scan the laser over about 1 GHz only, so larger frequency changes were performed by tuning the temperature of the laser diode and keeping track of the number of fringes while the temperature of the laser changed. This process takes about 30 seconds to accurately scan the laser up to 20 GHz (about 1000 fringes). No mode-hops were ever observed during this scanning.

The fringe-counting method requires a small frequency-modulation of the laser to be converted to an amplitude modulation by the interferometer. The frequency-modulation was performed by turning off the integrator function of the Arduino, and instead outputting a small sine wave at 140 kHz. This oscillates the laser piezo and thus modulates the laser frequency.

A.3 Calibration of the interferometer

To use the MZI output as an accurate measurement of the laser frequency, it first needed to be calibrated so that the frequency change of one fringe is known. This calibration was done in three ways.

A.3.1 Calibration by path-length-difference

The first calibration was done by using the physical properties of the interferometer. The phase difference of the interfering signals at either output is given by

$$\Delta\phi = nk\Delta L \tag{A.1}$$

where n is the refractive index of the fiber, $k = 2\pi/\lambda$, and ΔL is the path-length difference of the interferometer arms. This interferometer was made using Corning SMF-28 fibre with a refractive index of n = 1.4682 at 1550 nm [122], and has a path-length difference of $\Delta L = 10.4$ m. This can be rearranged to find what change in frequency (proportional to k) gives a 2π phase difference.

$$\Delta f = \frac{kc}{2\pi} = \frac{c}{n\Delta L} \approx 19.634\,\mathrm{MHz} \tag{A.2}$$

This value is only a rough estimate as the fibre lengths are known only from the package labels which may not be accurate.

A.3.2 Calibration with DROP spectroscopy

Another way of calibrating the interferometer was to use the excited-state transitions as a frequency reference. This was done in two ways, the first using double-resonance optical pumping (DROP). DROP is explained in Fig. A.3. It involves pumping atoms from one ground state to another via an excited-state transition. The atoms are initially driven on a closed transition (in this case the $5S_{1/2}, F = 2 \rightarrow 5P_{3/2}, F' = 3$ transition), the excited state of which can only decay to the same state the atom started from. Addition of a laser resonant with an open excited-state transition excites the atoms to an even higher state, which has a finite probability of decaying to a different ground state. Thus the addition of the second laser enables pumping from one ground state to another, an effect which can be observed by measuring ground state populations.

DROP was used to calibrate the interferometer by measuring the absorption of a laser at 780 nm in a rubidium vapour cell. The 780 nm laser is locked on-resonance with the $5S_{1/2}, F = 2 \rightarrow 5P_{3/2}, F' = 3$ transition. The 1529 nm laser counter-propagates through the vapour cell, mode-matched to the 780 nm laser. The frequency of the 1529 nm laser is scanned periodically by applying a sawtooth wave to the laser piezo controller, and the absorption of the 780 nm signal is captured on an oscilloscope along with the interferometer signal from the 1529 nm laser. The resulting data is shown in Fig. A.4. There are two absorption peaks visible, these peaks occur as a result of the 1529 nm laser crossing the two excited-state transitions from the $5P_{3/2}, F = 3$ state to the $4D_{3/2}, F = 2, 3$

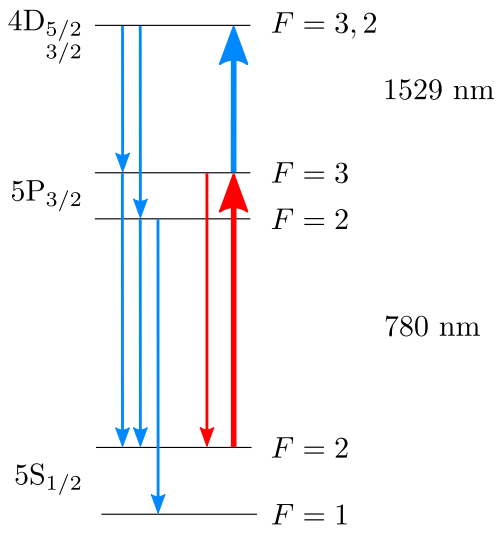

Figure A.3. Simplified level diagram of ^{87}Rb showing relevant levels for DROP spectroscopy. The red lines show excitation and decay paths available with just a 780 nm laser resonant with the $F = 2 \rightarrow F' = 3$ transition. The blue arrows show the additional excitation and decay paths introduced with the inclusion of a laser at 1529 nm.

states, which changes the relative population of the two $5S_{1/2}$ levels, changing the absorption of the 780 nm light. These two excited-state transitions have been measured to high accuracy (e.g. [123]), and the frequency difference is known to be 77.44 MHz. The two absorption peaks are thus used to calibrate the frequency scale by fitting two Lorentzian lineshapes to the absorption peaks. A sine wave is fitted to the interferometer signal to get the calibration, which is 18.86 MHz per fringe. This method is compromised by there being a large DC offset on the absorption signal. Shown in the figure is the AC-coupled oscilloscope trace, but the AC coupling distorts the signal, limiting the accuracy of this measurement.

A.3.3 Calibration with non-degenerate MTS

The final and most accurate method of calibrating the interferometer uses a form of AC spectroscopy called modulation transfer spectroscopy (MTS). This method is used to lock lasers in our lab (our setup is published and characterised in [117], a good description of the theory of MTS can be found in [124]). In MTS there are two laser beams counter-propagating through a vapour cell. One of the beams is frequency-modulated, and if both beams are close to an atomic

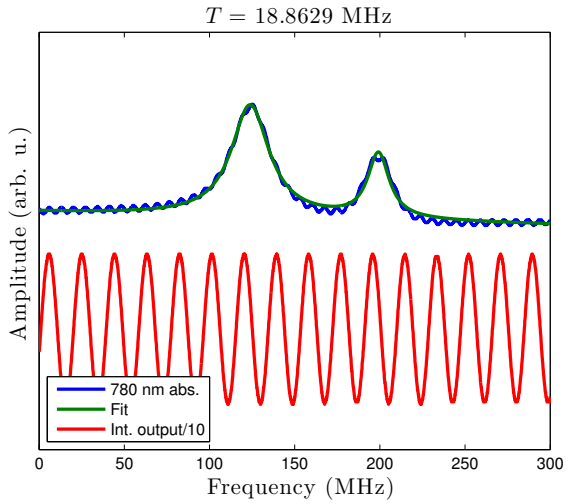

Figure A.4. Rough calibration of the interferometer period. The peaks show increased transmission of a laser at 780 nm as the 1529 nm laser crosses the $5P_{3/2}, F = 3 \rightarrow 4D_{3/2}$ resonances.

resonance, this creates an oscillating refractive index for the other beam. This oscillating refractive index effectively transfers the modulation to this other beam, which can then be demodulated to obtain an error signal. MTS provides error signals with high signal-to-noise ratio and no DC offset. This can be done in a degenerate (both beams address the same transition) or non-degenerate (the two beams address different but connected transitions) manner.

For calibration of the interferometer I used the non-degenerate technique where one laser was locked at 780 nm, addressing the $5\mathrm{S}_{1/2}, F = 2 \rightarrow 5\mathrm{P}_{3/2}, F' = 3$ transition. The second laser is at 1529 nm and scanned across the excited-state $5\mathrm{P}_{3/2} \rightarrow 4\mathrm{D}$ transitions. The demodulated MTS signal observed when the 1529 nm laser is scanned across the $5\mathrm{P}_{3/2}, F' = 3 \rightarrow 4\mathrm{D}_{5/2}, F'' = 4$ transition is shown by the green line in Fig. A.5. For the calibration I then simply counted the number of fringes between the $4\mathrm{D}_{5/2}, F'' = 4$ and $4\mathrm{D}_{3/2}, F'' = 3$ resonances, which produce the largest MTS signals. The energies of these states are known very accurately, and the difference is 13478.506 MHz [125]. The number of fringes between these resonances was counted to be 697 fringes with an uncertainty of $\pm$ half a fringe, resulting in a calibration of 19.338 ± 0.028 MHz per fringe.

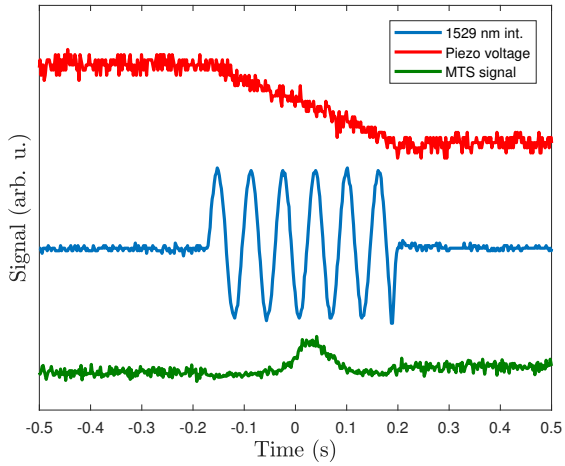

Figure A.5. The fringe counter counting 6 fringes across the excited-state $5P_{3/2}, F' = 3 \rightarrow 4D_{5/2}, F'' = 4$ resonance. The noise decreases on the 1529 nm MTS signal (green line) while the fringe counter is counting as it frequency-modulates the laser, moving noise to higher frequencies that are filtered out of the signal.

A.3.4 Temperature and frequency stabiliity

A measurement of the stability of the 1529 nm laser locked with the interferometer also used nondegenerate MTS. With the temperature of the interferometer locked with the 1560 nm laser signal, the 1529 nm laser frequency was scanned at about 10 Hz across an excited-state resonance, producing an MTS signal like in Fig. A.5 (and simultaneously producing a DROP signal like in Fig. A.4). An oscilloscope trace was recorded every minute, and fit a Lorentzian to the MTS signal, and a sine wave to the oscillatory interferometer signal (e.g. blue line in Fig. A.5). The phase of the sine wave was then compared to the peak of the Lorentzian. Allan deviation from a typical dataset is shown in Fig. A.6. The MTS signal comes from an atomic reference, so in principle this should be very stable. The phase of the interferometer signal relative to the MTS signal is a measurement of where the 1529 nm laser would lock to, if it were locked. The measurement here showed an RMS frequency drift of 225 kHz over 15 hours.

Note that this is an upper bound in the inteferometer instability. The MTS signal is highly dependent on the phase of the demodulation (see [117]), and it was empirically observed that the measured stability of the interferometer was much worse just after the MTS electronics was powered on compared to a few

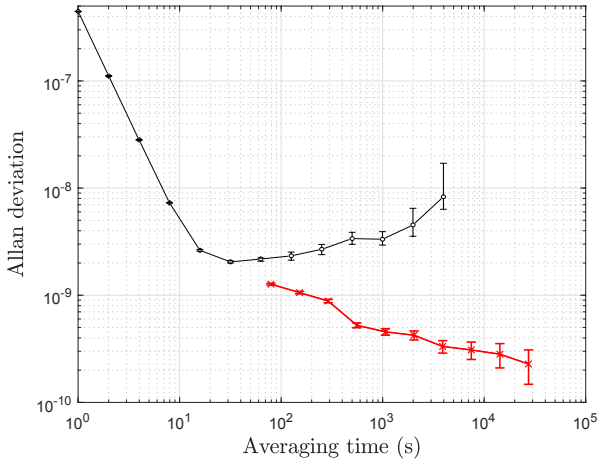

Figure A.6. Allan deviation of the 1529 nm laser frequency stabilised with the interferometer (red crosses). Black circles show data from ref. [119] for comparison. Red crosses correspond to a 15-hour measurement, over which the laser frequency had an RMS stability of 225 kHz. Red error bars were calculated as the value of the data point divided by the square root of the number of intervals for that averaging time.

hours later, despite the interferometer having been locked for several days. This suggests that at least some of the measured instability is due to temperature drifts in the MTS electronics, and not the interferometer.

Figure A.7 shows a calibration of the temperature stability of the interferometer, note that the y-axis is half-fringes. The temperature of the interferometer was measured with a thermistor while the fringe counter was running and the heating was turned off. By counting fringes as the interferometer cooled down from its nominal temperature I could obtain an estimated conversion from fringes to temperature of 646 half-fringes per Kelvin, or 323 fringes per Kelvin. The earlier frequency calibration measurement gave a conversion from frequency to fringes of 19.38 MHz per fringe. Knowing that the RMS frequency stability of the inteferometer is 225 kHz over 15 hours, we can convert this to an estimated RMS temperature stability of 36 µK over 15 hours.

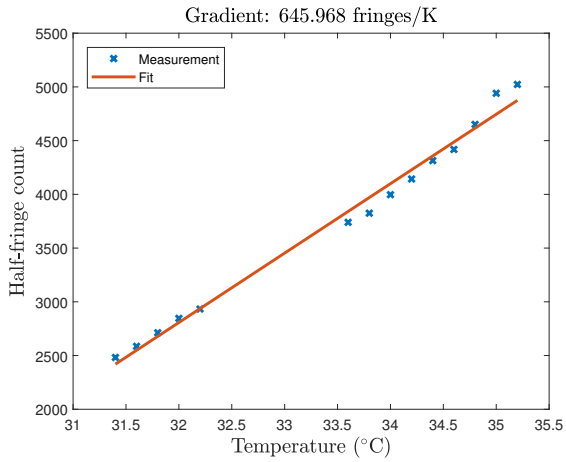

Figure A.7. Temperature sensitivity of the interferometer. This measurement was performed by counting fringes as the interferometer cooled down, temperature was measured using a thermistor.

Appendix B

Phase-contrast imaging system for the experiment in Florence

B.1 Introduction

Towards the end of my time in Florence I started working on a phase-contrast imaging (PCI) system to provide the capability of performing non-destructive measurements of the two-mode BEC. This appendix summarises the progress made. Note that this appendix is a summary of information specific to the Florence experiment. A more general and comprehensive reference on PCI is the Master's thesis of Maxime Joos of the University of Heidelberg [126].

PCI is a technique that exploits the phase shift of probe light by a cloud of cold atoms, rather than the absorption as in standard absorption imaging. Cold atoms can non-destructively imprint a phase shift on off-resonant probe light, giving a signal that is a function of the column density of atoms. This has several advantages compared to conventional absorption imaging: For example if the atomic cloud is an optically-trapped BEC, the atoms can be imaged without losing coherence and without being heated out of the shallow optical trap, which enables several images to be taken of the same BEC for studies of quantum dynamics etc.

To see the phase shift signal from the atoms, the light that is phase-shifted must be interfered with some reference light. The reference beam and the signal

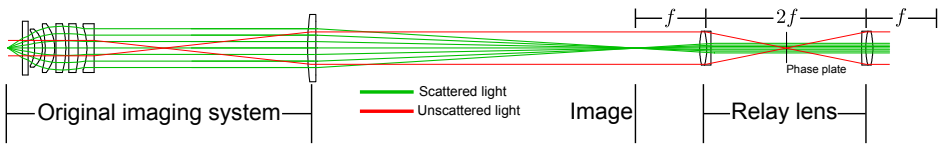

Figure B.1. Optical system for phase contrast imaging on the Florence experiment. The "original imaging system" is what is currently installed on the experiment. The focal plane of the objective is too close to the objective for the phase spot to be placed there, so a relay lens must be used. The phase plate is placed exactly between the two elements of the relay lens. The green lines show the path of light scattered from the atom cloud, and the red lines show the path of the probe beam, which is collimated at the input. f is the focal length of the lenses used for the relay lens.

beam can be the same beam if one employs a "phase spot": a clear flat piece of glass with a small ($\sim 50\,\mu$m) circle of slightly different thickness cut into the centre. Light that passes through this central spot then experiences a different phase shift compared to light that passes around the spot (i.e. light with large k-vectors due to being phase-shifted by the atoms). The phase spot is placed in the focal plane of the lens so that the probe light is selectively phase shifted relative to light that has been phase-shifted by the atoms. This light is then interfered on the camera, giving a signal related to the phase shift from the atoms. This process is shown in Fig. B.1.

B.2 Basic theory of PCI

This section calculates the signal observed on a camera placed in the image plane of the imaging system shown in Fig. B.1. Note that there are two image planes: one before and one after the relay lens.

Assuming no absorption of the probe light and that the atomic cloud is small compared to the probe beam size, the light reaching the camera can be written as the sum of the probe light and the light phase-shifted by the atoms

$$E = E_{probe} + E_{atoms} = E_{probe} + E_{probe}(e^{i\phi} - 1) \tag{B.1}$$

where ϕ is the spatially-dependent phase shift of the light due to the atoms. The phase spot can be placed at the focal plane of the relay lens, selectively phase shifting the probe light relative to the scattered light.

$$E = E_{probe}e^{i\theta} + E_{probe}(e^{i\phi} - 1) \tag{B.2}$$

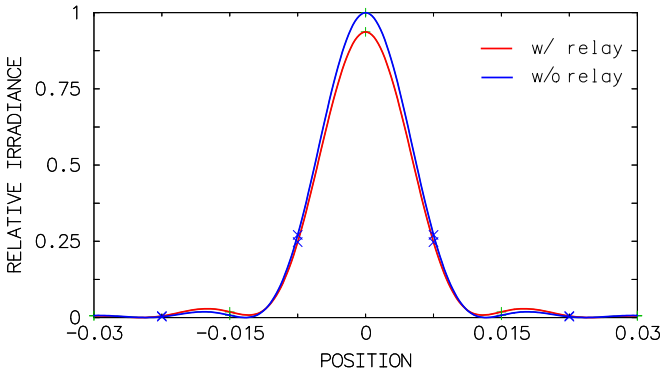

Figure B.2. Comparison of the point-spread functions of the optical system with and without the relay lens. The lenses used were doublets with f = 100 mm and clear aperture of 21 mm diameter (i.e. 1 inch lenses). Units on the x-axis are mm.

The intensity on the camera is given by:

$$I = \frac{c\epsilon_0}{2}|E|^2 = I_0(3 - 2\cos\theta + 2\cos(\theta - \phi) - 2\cos\phi) \tag{B.3}$$

and with $\theta = \pi/2$, the resulting intensity on the camera is

$$I = I_0(3 + 2(\sin\phi - \cos\phi)) \tag{B.4}$$

The phase shift from the atoms can then be extracted numerically. In Section B.4 I estimate the phase shift as a function of density.

B.3 Optical performance of the relay lens

The experiment will require a relay lens to implement the PCI, as the focal plane of the experiment objective lens is physically located too close to the lens body. OSLO optical design software was used to analyse the effect of the relay lens on image quality. Fig. B.2 shows the point-spread functions of the imaging system in the image planes before and after the relay lens. The relay lens is assumed to be constructed of two realistic doublet lenses, with a focal length of 100 mm, and a clear aperture of 21 mm diameter (i.e. 1 inch lenses).

B.4 Calculation of light propagation in an atomic cloud

This section derives an expression for the phase shift of the light as a function of the density of the atoms.

Atomic susceptibility We can calculate the effect of an atomic medium on light using the susceptibility. Ref. [127] gives the complex susceptibility as

$$\begin{aligned}\chi_{eg} &= \frac{\rho|D_{eg}|^2}{\epsilon_0\hbar}\frac{(-\Delta+i\Gamma/2)}{\Delta^2+\Gamma^2/4+\Omega^2/2} \\ &= \frac{\rho|D_{eg}|^2}{\epsilon_0\hbar}\frac{4}{\Gamma^2}\frac{(-\Delta+i\Gamma/2)}{1+4\left(\Delta/\Gamma\right)^2+2\left(\Omega/\Gamma\right)^2} \\ &= \frac{\rho|D_{eg}|^2}{\epsilon_0\hbar}\frac{4}{\Gamma^2}\frac{(-\Delta+i\Gamma/2)}{1+I/I_s+4\left(\Delta/\Gamma\right)^2}\end{aligned} \tag{B.5}$$

where ρ is atomic density in ground state $|g\rangle$ and D_{eg} is the dipole matrix element coupling ground state $|g\rangle$ with excited state $|e\rangle$, Ω is the atomic Rabi frequency (a function of the electric field amplitude), Δ is the laser detuning from resonance, and Γ is the atomic linewidth, I is the light intensity and I_s is the saturation intensity for the transition (the intensity at which the scattering rate is half the maximum scattering rate on-resonance), and $2|\Omega|^2/\Gamma^2 = I/I_s$.

Scattering rate Ref. [20] gives the photon scattering rate of a single two-level atom as

$$R = \frac{\Gamma}{2}\frac{I/I_s}{1+I/I_s+4\left(\Delta/\Gamma\right)^2} \tag{B.6}$$

Light propagation using the Helmholtz equation We can calculate the effect of the atomic medium on a laser beam with $k = 2\pi/\lambda$, and electric field E. The Helmholtz equation in a three-dimensional medium with susceptibility χ is [128]

$$\nabla^2 E(\mathbf{r}) + k^2[1+\chi(\mathbf{r})]E(\mathbf{r}) = 0 \tag{B.7}$$

If we let $E(\mathbf{r}) = E_0(\mathbf{r})e^{ikz}$, and make the paraxial approximation that the electric field envelope E_0 is slowly varying in the z-direction (such that $\partial^2 E_0/\partial dz^2 = 0$), we get

$$-2ik\frac{\partial E_0(\mathbf{r})}{\partial z} = \nabla_\perp^2 E_0 + k^2\chi E_0 \tag{B.8}$$

Now say the medium and propagrating wave are flat in the $x-$ and $y-$directions

$$-2ik\frac{\partial E_0(z)}{\partial z} = k^2\chi(z)E_0(z) \tag{B.9}$$

The solution to this is

$$E_0(z_0+\delta z) = \exp\left(\frac{ik}{2}\int_{z_0}^{\delta z}\chi(z)dz\right)E_0(z_0) \tag{B.10}$$

and we can see that the phase shift ϕ of the light is

$$\phi = \frac{k}{2}\int_{z}^{\delta z}\mathrm{Re}\{\chi(z)\}dz. \tag{B.11}$$

Phase shift signal as a function of trap parameters The spatial distribution of a BEC can be well-defined as a function of trap parameters.

First of all we estimate the atomic density. Non-interacting atoms trapped in the ground state of a quantum harmonic oscillator (i.e. an optical dipole trap) have a Gaussian spatial distribution, the size of which depends only on the trapping frequency.

$$\psi_0(x,y,z) = \sqrt{\rho_0}\times\exp(-\frac{m}{2\hbar}(\omega_x x^2+\omega_y y^2+\omega_z z^2)) \tag{B.12}$$

where w_r is the trap frequency in dimension r, and ρ_0 is the peak atom density at the centre of the cloud. We can find ρ_0 by integrating in all three dimensions:

$$\begin{aligned} N &= \int_{-\infty}^{\infty}\int_{-\infty}^{\infty}\int_{-\infty}^{\infty}|\psi_0|^2dxdydz \\ &= \rho_0\left(\frac{\pi\hbar}{m}\right)^{\frac{3}{2}}\frac{1}{\sqrt{\omega_x\omega_y\omega_z}} \\ \therefore \rho_0 &= N\left(\frac{m}{\pi\hbar}\right)^{\frac{3}{2}}\sqrt{\omega_x\omega_y\omega_z} \end{aligned} \tag{B.13}$$

where N is the total number of atoms. We estimate the frequencies in our experiment to be $(w_x, w_y, w_z) = 2\pi\times(200, 200, 300)$ Hz, giving a peak density of $\rho_0 = 1.5\times10^{14}$ cm^{-3}. We can estimate the column density by integrating the atom density in the $z-$direction.

$$\begin{aligned} \rho_{col}(x,y) &= \int_{-\infty}^{\infty}|\psi_0(x,y,z)|^2dz \\ &= \sqrt{\frac{\pi\hbar}{m\omega_z}}|\psi_0(x,y)|^2 \end{aligned} \tag{B.14}$$

at $(x, y) = (0, 0)$ this is

$$\begin{aligned}\rho_{col}(0,0) &= \sqrt{\frac{\pi\hbar}{m\omega_z}}\rho_0 \\ &= N\sqrt{\frac{\pi\hbar}{m\omega_z}} \times \left(\frac{m}{\pi\hbar}\right)^{\frac{3}{2}} \sqrt{\omega_x\omega_y\omega_z} \\ &= N\frac{m}{\pi\hbar}\sqrt{\omega_x\omega_y}\end{aligned} \tag{B.15}$$

Now we can estimate the total phase shift of a laser passing through the centre of the cloud using Eq. B.11. The atomic density is the only part of the susceptibility that depends on position, and the integral was already performed in Eqs. B.14 & B.15. Combining everything

$$\begin{aligned}\phi &= \frac{k}{2}\int_{-\infty}^{\infty} \rho dz \frac{\mathrm{Re}\{\chi\}}{\rho} \\ &= \frac{k}{2} N \frac{m}{\pi\hbar}\sqrt{\omega_x\omega_y}\frac{\mathrm{Re}\{\chi\}}{\rho}\end{aligned} \tag{B.16}$$

Phase shift under 'typical' experimental conditions Fig. B.3 shows the estimated phase shift and scattering rate for light passing through the densest part of the ^{39}K BEC in Florence under 'typical' conditions of the experiment. These plots were calculated using potassium data from [129], and 'typical' experiment conditions are given in Table B.1.

We simultaneously want a visible phase shift and minimal excitation of the atoms. Close to resonance the shift is quite large (~ 100 rad one linewidth away), but the scattering of photons is non-negligible. A typical absorption image probe pulse is 10 μs. If we want to excite, say, 1 in every 100 atoms, we want a scattering rate of 10^{-2} photons per atom/10^{-5} s = 1000 photons/s, so we want to work at laser frequencies where the scattering rate is less than 1000 Hz (see Fig. B.4)

Number of atoms	1000
$\|F, m_F\rangle$	$\|1, -1\rangle$ (absolute ground state)
B-field	350 Gauss
I/I_{sat}	~ 1
λ	767 nm
ρ_0	1.5×10^{14} cm^{-3}
(w_x, w_y, w_z)	$2\pi \times (200, 200, 300)$ Hz

Table B.1. Typical experiment parameters used to calculate the phase shift and scattering rate shown in Figs. B.3 and B.4.

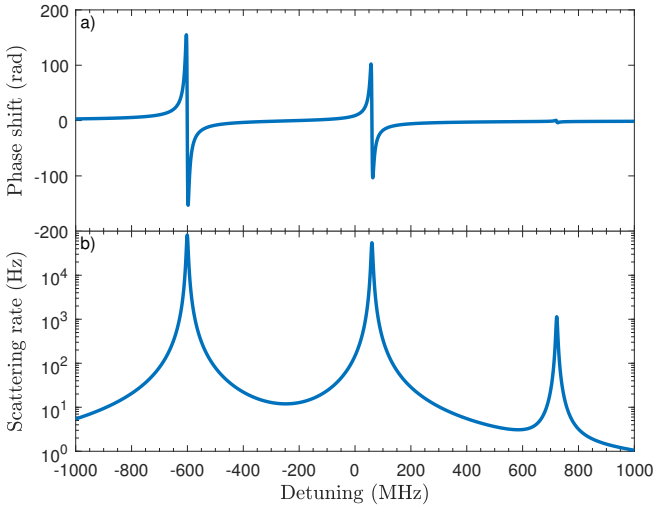

Figure B.3. Estimated phase (a) of a beam passing through the densest part of the BEC as a function of frequency, and scattering rate (b) of an atom. Both curves were calculated using the parameters in Table B.1. The frequency axis is relative to the $F = 2 \rightarrow F' = 3$ transition in the D_2 manifold in ^{39}K.

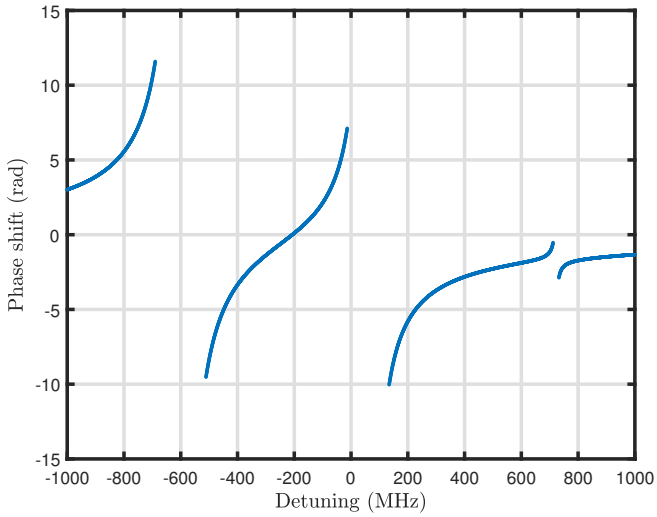

Figure B.4. Phase shift under 'typical' experimental conditions, at frequencies where the scattering rate is less than 1000 Hz. Again the frequency axis is relative to the $F = 2 \rightarrow F' = 3$ transition in the D_2 manifold in ^{39}K.

Appendix C

Experiment control system

Ultracold gas physics experiments require precise control and synchronisation (timing accurate to $\sim 1\,\mu s$) of a large number of active optical and electronic hardware components. This appendix is an overview of the control system developed for the Barcelona experiment. An overview of the control system is shown in Fig. C.2. In the following text each component is briefly described.

C.1 Software

Every experiment uses a unique combination of hardware and has a unique set of requirements for the experiment sequences. Software to control these experiments usually needs to be custom, at least to some degree, as no commercially available software suitable for controlling an atomic physics experiment yet exists (to my knowledge).

C.1.1 Cicero & Atticus

Given that laser cooling experiments are now reasonably mature, a few groups have developed versatile software systems appropriate for distribution. Rather than develop our own software from scratch, we decided to use a system called Cicero, developed in the group of Wolfgang Ketterle at MIT [130]. This software provides a way of designing experiment sequences through a visual interface (some systems use a text-based interface). A screenshot is shown in Fig. C.1. An "experiment sequence" is a description of the output value of a number of hardware channels as a function of time. These can be digital channels, which can be on or off, or analogue channels which can output a range of values.

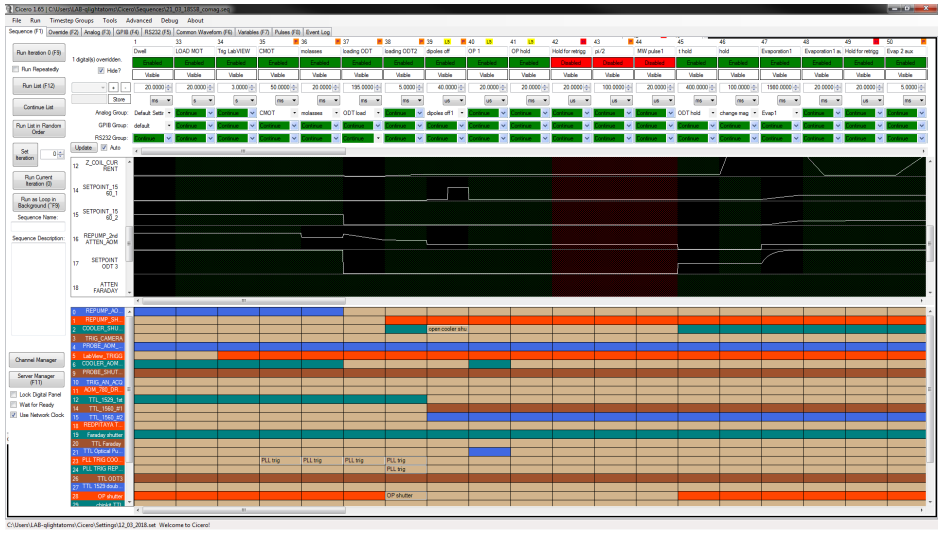

Figure C.1. Screenshot of Cicero. An experimental sequence is divided into timesteps horizontally, and channels vertically. Analogue channels are represented by the white lines on the black/green background, and digital channels by the coloured boxes.

Cicero works with a program called Atticus in a client-server configuration. Cicero generates the experiment sequences, then sends them to the Atticus server, which translates the sequence into instructions for the hardware, then sends these instructions to the hardware to output. Cicero and Atticus are made to work mainly with National Instruments (NI) input/output (I/O) hardware.

Cicero can also be used to control serial and GPIB devices. However as these communication protocols are not real-time, we used these interfaces to preprogram devices, such as Arduinos, before starting the sequence which were later triggered using a digital signal. For example one Arduino was pre-programmed over a serial interface with a queue of laser frequencies, which could then be triggered in real-time at specific points in the sequence to change the laser frequency to the next frequency in the queue.

C.1.2 LabVIEW for data acquisition, data storage, and experiment monitoring

While the Cicero/Atticus system is supposed to have functionality for recording data, we were never able to make it work. Instead, we wrote a LabVIEW program to record data and monitor the status of the experiment. LabVIEW was chosen for the ease of making graphical user interfaces (GUIs) with this language, and it naturally works well with NI hardware. The LabVIEW program has two parts: a background loop constantly recording and displaying various signals to monitor the 'health' of the experiment, and another real-time triggered component that records analogue signals from the experiment at points in the experiment sequence dictated by Cicero.

The default state of the experiment is with a loaded MOT. While this is a static state, many instruments must be stably operating within a strict parameter range for atoms to be observable inside the MOT. The monitor part of the LabVIEW program records and displays as many of these parameters as possible to check the experiment is functioning correctly. For example, we measure the ion pump current to check the vacuum level is stable, the error signals from the laser locks to check the laser frequencies are stable, and a photodiode records the power of the cooling lasers to check this is stable, and we also monitor the current in the MOT magnetic field coils. The most important signal we monitor, however, is fluorescence from the MOT itself. This is measured with a photodiode looking through a telescope pointing at the centre of the vacuum chamber. The MOT fluorescence is sensitive to the majority of parameters in the experiment, so observing a time-domain graph of this signal alone can often be enough to diagnose technical problems (although this takes some practice).

For the most part, scientific data is acquired with the experiment camera. However, some data can be in the form of a time-dependent voltage, and for diagnosis of technical problems it can be useful to observe the dynamic behaviour of signals from many experiment instruments. For this reason part of the LabVIEW program records analogue signals at a time dictated by a trigger from the Cicero experiment sequence. This can be useful for checking, for example, how long the magnetic field coils take to switch off, how long the dipole trap lasers take to switch on or off, or checking the behaviour of the dipole trap laser during evaporation.

C.1.3 HDF5 data storage

The final job of the LabVIEW program was to collate and store all the experiment data in a recoverable form. For every experiment run we saved a copy of the experiment sequence, analogue data, and camera data to an HDF file (Hierarchichal Data Format), which can contain all the data in a single file and provides efficient retrieval of a specific subset of the data.

C.1.4 MATLAB GUI for real-time data monitoring

Most experimental data was in the form of absorption images, with one image taken each experiment run. We used MATLAB to make a GUI to process the data and display the image as fast as possible immediately after the experiment run was finished. MATLAB also performed rudimentary analysis of the data, giving parameters such as the estimated number of atoms in the image and the cloud size.

C.2 Hardware

Like the experiment software, there is no single hardware system suitable for an atomic physics experiment. Instead, many components from disparate sources must be integrated and made to reliably work together. This section just mentions the two main parts: an atomic clock-based timing source and a National Instruments PXI rack for analogue and digital input and output.

C.2.1 Timing

All clocked hardware in the experiment is referenced to a 10 MHz clock signal from a Stanford Research Systems CG635 synthesised clock generator (SCG) with a rubidium timebase, which provides a stable low-jitter clock signal.

Cicero and Atticus provide the option of using an FPGA to generate a variable-rate clock signal. Long experimental sequences would require an impractically large number of samples if the entire sequence were clocked at the maximum required sampling rate of the sequence. To mitigate this effect, Atticus generates a variable-rate clock signal for every experiment sequence that clocks the sequence only at the sampling rate required for that part of the sequence. For example a fast-changing analogue signal requires a fast clock, while there are several parts of the sequence where no output changes for several hundred milliseconds, which does not require any clock at all. The generated clock sequence is sent to an

FPGA referenced to the SCG, the FPGA is pre-programmed with firmware which outputs a clock signal at the appropriate rate throughout the sequence.

Cold atomic clouds are sensitive to external magnetic fields, especially during state preparation procedures. The main uncontrolled external source of magnetic fields in a laboratory is mains electricity powering the lab equipment and in cables running through the walls. The 50 Hz oscillation frequency of mains electricity is slow on the timescale of processes in the experiment, so depending on the phase of the mains when the experiment sequence is started, the background magnetic field can be significantly different at a given point of the sequence. To mitigate this we implemented a system to trigger the experiment on a zero-crossing of the mains electricity, significantly reducing the variation in background magnetic field.

C.2.2 Input/Output

Our system uses a NI PXI rack with a mixture of 16-bit and 12-bit analogue I/O channels, a range of ±10 V, and a maximum sample rate of about 500 kS/s, although we were limited by Cicero to an output rate of 50 kS/s (i.e. timesteps of 20 µs). In the rare cases where we needed higher input sampling rates, we used Cicero to trigger an external device. For example in some experiments we used a high-speed analogue aquisition board called a Red Pitaya, which has analogue sampling rates of up to 125 MS/s.

C.3 Laser frequency stabilisation and control

The experiment has a main "master" laser which is used as a reference for all the other lasers in the experiment. The master laser is locked using modulation-transfer spectroscopy, and is well-described elsewhere [117]. Relevant here is that this master laser provides a stable frequency source 160 MHz blue of the $5S_{1/2}, F = 2 \rightarrow 5P_{3/2}, F' = 3$ transition.

C.3.1 Slave lasers with digitally programmable offset locks

The cooling and repump lasers used for the MOT and optical molasses phases of the experiment are locked relative to the master laser by measuring and controlling the beatnote of the interference of the lasers on a fast photodiode. This technique was published in [131]. The basic idea of this technique is that a high-speed digital phase-locked loop frequency synthesiser (PLL) is used to compare the beatnote of the interference of the master and slave lasers to a stable reference

signal. The PLL divides the frequency of the beatnote using a programmable digital counter, and then outputs an error signal proportional to the phase difference between the two signals. This error signal can be fed to a controller which acts on the slave laser frequency.

Our original implementation of this PLL system used the frequency of the reference signal as the control variable: A voltage-controlled oscillator (VCO) provided a variable-frequency source which was compared to the divided beatnote signal. Changing the VCO frequency with an analogue voltage output from Cicero changes the lock frequency of the slave laser. This method is prone to long-term drifts, however, as the VCO output frequency is temperature-dependent. Rather than change the reference signal frequency, we realised we could instead reprogram the divider settings on the PLL. This can be done by setting a 24-bit register on the PLL over an SPI interface, which can be done in a few tens of microseconds with a microcontroller. For the reference signal, we used the 10 MHz SCG. To lock the cooling and/or probe laser on resonance, we set the PLL to lock the laser with a beatnote of 160 MHz. To tune the laser to the blue of resonance, we decreased the frequency of the PLL. The PLL used is an ADF4110, which is supposed to work down to 80 MHz, but we found the lock became unstable at around 120 MHz (i.e. with the laser 40 MHz blue-detuned from resonance), limiting the blue-detuning range of the cooling and/or probe laser.

The error signal from the PLL can be used as a measurement of whether or not the laser frequency is stable: If the beatnote between the master and slave lasers is at the programmed frequency, the error signal is zero. If the slave laser frequency is changing or unstable, this can be diagnosed by looking at the error signal as a function of time.

C.4 Camera

The camera used in the experiment is a PCO Pixelfly. This is a black-and-white scientific USB camera. The feature important for our experiments is "double-framing", where the camera can take two photos in quick succession (within a few hundred microseconds of each other). This is important for proper absorption imaging, as described in Chapter 3.

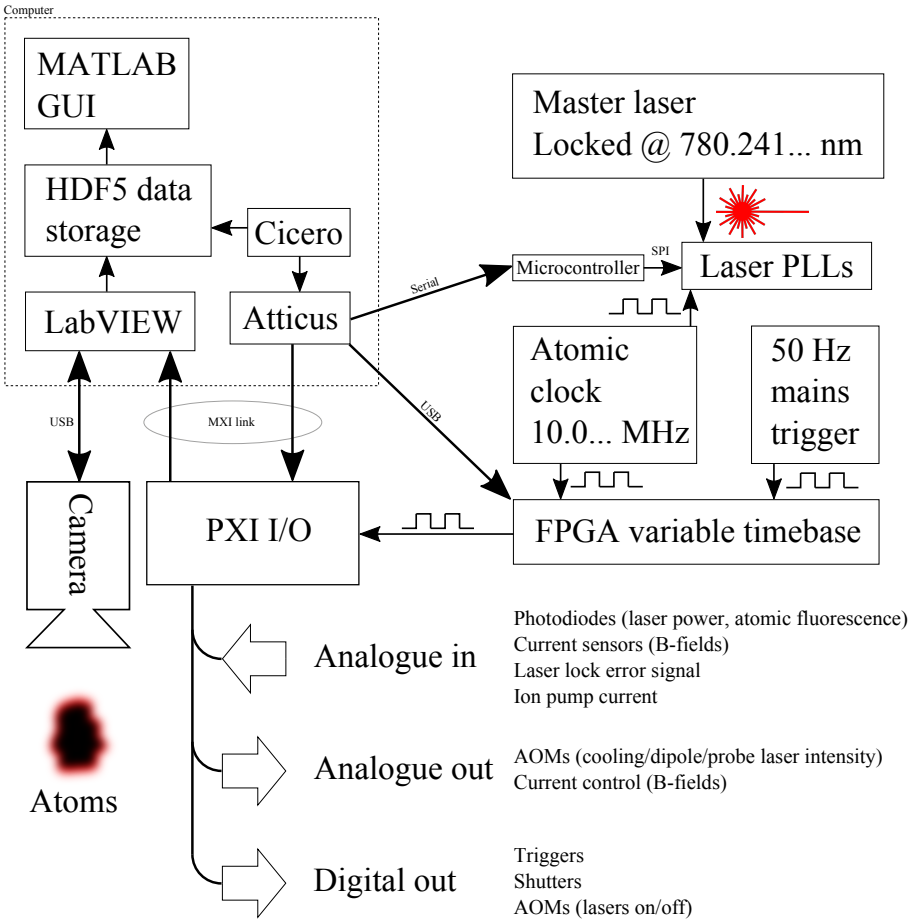

Figure C.2. Diagram showing logical blocks of the control system developed to run the experiment. The individual components are briefly explained in the text. The labels next to each connection indicate the format of that connection. The square wave means a digital clock signal, and the laser symbol indicates light in an optical fibre.

Appendix D

Absorption imaging model for determining detection limits

One of the goals of the experiment in Florence was to measure atom numbers with high enough resolution to detect atom number squeezing in the double-well system (see Chapter 7). By increasing the strength of inter-atomic interactions, the fluctuation in the atom number in each well should decrease to zero. In order to measure this we would need to image the atomic cloud in each well with high enough resolution in atom number to see if the fluctuations decrease below that expected in the standard quantum limit. To this end, I developed a model of the imaging system to estimate the best atom number resolution possible with our experiment under the best possible imaging parameters.

For a given number of atoms, we want to find the optimum cloud density, probe light intensity, and probe pulse length to minimise errors in the detection of the atom number in the double-well potential. With too high an atom density, too few photons propagate completely through the centre of the cloud and so information is lost about the density. With too low an atom density the atomic signal becomes buried in photon shot noise and camera electronic noise. Regarding the light intensity, higher light intensity means more signal, up to the point where the atoms become saturated. After this point, photon shot noise increases but atomic signal stays the same so the signal-to-noise ratio (SNR) decreases. Atomic saturation is nonlinear so the optimum light intensity is not obvious.

D.1 Noise sources

The first step in making the model was to characterise noise sources in the imaging system. There are three primary noise sources identified: shot noise in the probe beam, detection noise (the quantum efficiency of the camera is 0.95, so each photon incident on the camera has a 95% chance of being absorbed), and camera electronic noise (the readout noise and dark noise cannot be measured independently, so are treated as a single source of noise).

The camera used in this experiment is an Andor iKon M934 with a CCD sensor cooled to -70°C. The pixels are 13 µm square, and the imaging system has a magnification of 31.5×, resulting in a pixel size in image space of 0.4127 µm on each side.

Probe beam noise The probe beam was assumed to be shot noise limited, so was simulated as a Poisson distribution with the mean corresponding to a given probe intensity. One effect I was not able to simulate well was fringes in the probe beam. They constitute local variations in intensity (see Fig. D.1), which means local variations in atomic saturation.

Detection Every photon incident on the CCD has a 95% chance of being detected. Photon detection events are in principal uncorrelated and random, so detection events are modelled with a binomial distribution with the number of trials being the incident number of photons and the chance of "success" (i.e. being detected) 0.95.

Electronic noise The electronic readout and dark noise was directly measured by analysing CCD images with no incident light. This noise was found to be well-approximated by a Gaussian distribution, and was assumed to be additive to the other noise.

Fig. D.1 compares statistics of a typical measurement of a probe beam image with a simulation. The difference between the measured distribution and simulated distribution is thought to originate from local variations in the probe beam intensity, or fringes.

D.2 Atom distribution

For the simulations the atomic density distribution used was a two-dimensional Gaussian, with $1/e$ widths σ_x and σ_y. In the Florence experiment it is possible

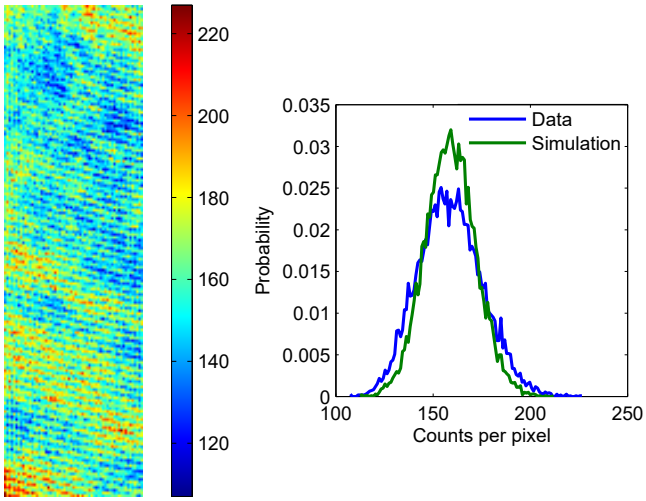

Figure D.1. The left figure shows a typical measurement of the probe laser without atoms. The colouring shows the photon count at each pixel. The right figure shows a histogram of the data in the left figure, and a simulated measurement of the probe with all noise sources taken into account. The broader width of the measured data is thought to be due to fringes, which are correlated between images.

to hold the atomic cloud in an optical potential and let it expand in one direction but not the other (more about this in Chapter 7), so the width σ_y of this Gaussian is changed to simulate different expansion times.

D.3 Simulating a real measurement

The absorption and background images were generated as follows: The atom number N, atomic distribution, and the probe light intensity are specified, then 2 matrices of Poisson-distributed random numbers representing the two probe beam pulses are generated. One of these matrices is used to generate the absorption image by numerically solving Eq. (3.6) for I_f with a known density distribution, the other matrix represents the background image. We now have the two probe beam pulses I_f and I_i. Detection is simulated as described above, and then a Gaussian distribution representing the electronic noise is added to each image. The data is then analysed exactly as we would analyse experimental data. The measured parameters are compared to the input parameters to see under what

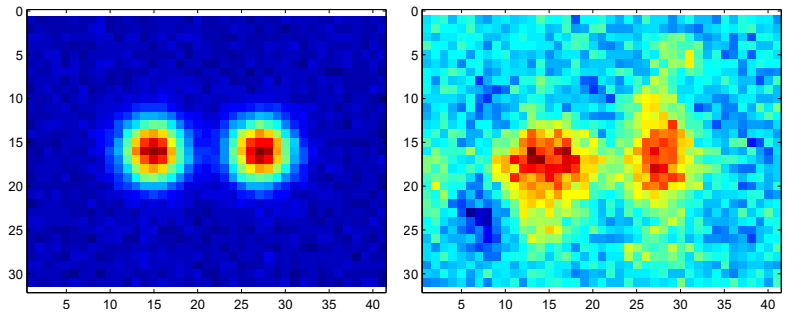

Figure D.2. (a) shows a simulated image of a balanced double-well in-situ. (b) shows an in-situ absorption image with the probe beam about 1 linewidth below resonance. The dimensions of the two images are the same. The purpose of these images is just to indicate the dimensions of the simulation are correct. The noisy background of (b) is because the probe laser was detuned for the measurement which results in strong lensing of the beam. Also because there was a frequency difference of the probe beam between the two absorption images the fringes are more apparent.

conditions we can make the most accurate measurements.

D.4 Comparison with real data

Figure D.3 shows a comparison of simulated data with real measured experimental data. The experiment performed in this case consisted of loading an optical dipole trap and then letting the atomic cloud expand in one direction for different amounts of time. The simulation was performed under the optimum light intensity. The optimum light intensity was found by measuring the variance of the number of atoms as a function of light intensity, which in this case was found to be minimal at 500 photons. In the simulation the total atom number was always exactly 5000, while this parameter could not be precisely controlled in the real experiment. The two graphs show the same behaviour as a function of density: at high density the error bars are small but the mean atom number is too low, and at lower density the mean approaches the correct value but the error bars get bigger.

Figure D.2a shows a simulated image of a balanced double-well in-situ, and D.2b shows experimental data under the same conditions. For the second image

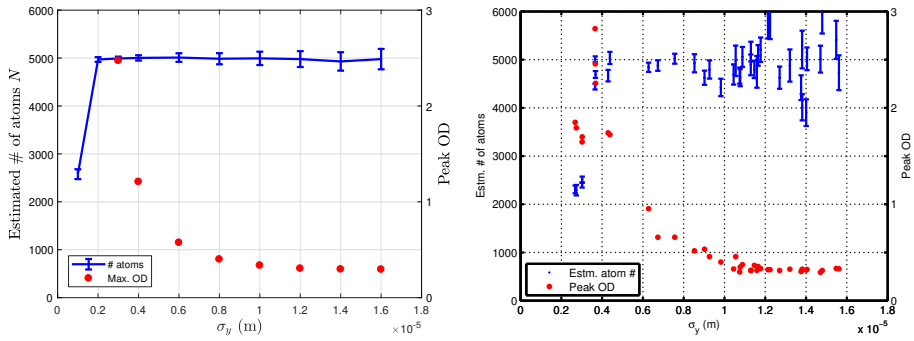

(a) Simulation (b) Experimental data

Figure D.3. Comparison of a simulation of a single Gaussian cloud with variable size against experimental data. The simulation was performed always with $N = 5000$, and the mean number of photons was 500, which was empirically found to give the smallest variance on the measured number of atoms in this situation.

the probe beam was detuned about 1 linewidth below resonance, to reduce the optical depth of the atomic clouds. This led to increased visibility of fringes in the image. These two images show that the resolution and dimensions of the simulation are realistic.

D.5 Atom-number fluctuations in the double-well

Here I derive an expression for the variance of a non-squeezed two-mode quantum state. This describes the noise expected in the atom number difference of the two wells for a coherent, or non-squeezed, state.

Classically, the observable is the difference in atom number between the two wells Z

$$Z = N_L - N_R \tag{D.1}$$

A single atom could be in the left well $|L\rangle$, the right well $|R\rangle$, or a superposition of both. So the operator z for a single atom in the double-well is

$$\hat{z} = |L\rangle\langle L| - |R\rangle\langle R| \tag{D.2}$$

So

$$\hat{Z} = \sum_{i=1}^{N} \hat{z}_i \tag{D.3}$$

where i is a label for the i^{th} atom, and N is the total atom number (which is also a random number, as it varies from shot-to-shot in an uncontrolled manner). We want to find the variance of $\hat{Z}$ to find the quantum-limited noise in the system for a non-squeezed state.

$$\begin{aligned} \mathrm{var}(\hat{Z}) &= \langle \hat{Z}^2 \rangle - \langle \hat{Z} \rangle^2 \\ &= \left\langle \sum_{i,j} \hat{z}_i \hat{z}_j \right\rangle - \left\langle \sum_i \hat{z}_i \right\rangle^2 \end{aligned} \tag{D.4}$$

If the atoms in the ensemble are uncorrelated, then the mean z of every atom is the same. So the last term of Eq. (D.4) is:

$$\begin{aligned} \left\langle \sum_i \hat{z}_i \right\rangle^2 &= \langle N \langle z \rangle \rangle^2 \\ &= \langle N \rangle^2 \langle z \rangle^2 \end{aligned} \tag{D.5}$$

and the first term is:

$$\left\langle \sum_{i,j} \hat{z}_i \hat{z}_j \right\rangle = \left\langle \sum_{i=j} \hat{z}_i \hat{z}_j \right\rangle + \left\langle \sum_{i \neq j} \hat{z}_i \hat{z}_j \right\rangle \tag{D.6}$$

From Eq. (D.2), $\hat{z}^2 = \hat{I}$, so

$$\begin{aligned} \left\langle \sum_{i=j} \hat{z}_i \hat{z}_j \right\rangle &= \sum_i \left\langle \hat{z}_i^2 \right\rangle \\ &= \langle N \rangle \end{aligned} \tag{D.7}$$

When $i \neq j$, z_i and z_j are independent random variables with the same mean, so

$$\begin{aligned} \langle \hat{z}_i \hat{z}_j \rangle &= \langle (\langle \hat{z} \rangle + \delta \hat{z}_i)(\langle \hat{z} \rangle + \delta \hat{z}_j) \rangle \\ \langle \delta \hat{z}_i \delta \hat{z}_j \rangle &= \delta_{ij} \end{aligned} \tag{D.8}$$

Substituting these into the second term of Eq. (D.6)

$$\begin{aligned}\left\langle \sum_{i\neq j} \hat{z}_i \hat{z}_j \right\rangle &= \left\langle N(N-1)\langle\hat{z}\rangle^2 \right\rangle \\ &= \langle N^2\rangle\langle\hat{z}\rangle^2 - \langle N\rangle\langle\hat{z}\rangle^2\end{aligned} \tag{D.9}$$

Summing Eqs. (D.5), (D.7), and (D.9)

$$\begin{aligned}\mathrm{var}(\hat{Z}) &= \langle N\rangle + \langle N^2\rangle\langle\hat{z}\rangle^2 - \langle N\rangle\langle\hat{z}\rangle^2 - \langle N\rangle^2\langle z\rangle^2 \\ &= \langle N\rangle\left(1-\langle\hat{z}\rangle^2\right) + \langle\hat{z}\rangle^2\left(\langle N^2\rangle - \langle N\rangle^2\right)\end{aligned} \tag{D.10}$$

note that the second term is $\langle\hat{z}\rangle^2 \times \mathrm{var}(N)$. In the case of a balanced double-well with $\langle\hat{z}\rangle = 0$, the variance of the atom number difference is simply $\langle N\rangle$, which is consistent with [132].

D.6 Feasibility of sub-shot-noise resolution

To see if Florence imaging system is capable of measuring squeezing, I ran some simulations of to measure $\mathrm{var}(\hat{Z})$ of a balanced double-well with 5000 atoms. $\mathrm{var}(\hat{Z})$ was measured for 50 different simulations for a range of "expansion times", i.e. images of a double-well with constant σ_x but variable σ_y. The simulations had a constant separation of 5 µm between the two clouds, and each cloud had a constant width of $\sigma_x = 1\,\mu\mathrm{m}$. A typical simulated image is shown in Fig. D.4a (compare with Fig. 7.5). Results of the simulation are shown in Fig. D.4b. Error bars show the standard deviation of 50 runs, with a minimum value of about 40, which is less than the standard deviation of a coherent state with 5000 atoms, for which one would expect a standard deviation of $\sqrt{5000} \approx 71$. This indicates that with this imaging system it should be possible to measure squeezing.

D.7 Conclusion

As well as estimating that this experiment should be able to observe number squeezing, the model provided two useful insights to absorption imaging in general. In all the simulations I performed both of the following were true:

- The optimum light intensity is about 2-3 times the atomic saturation intensity.
- The optimum density of the atom cloud is such that the maximum optical depth is ~ 2.

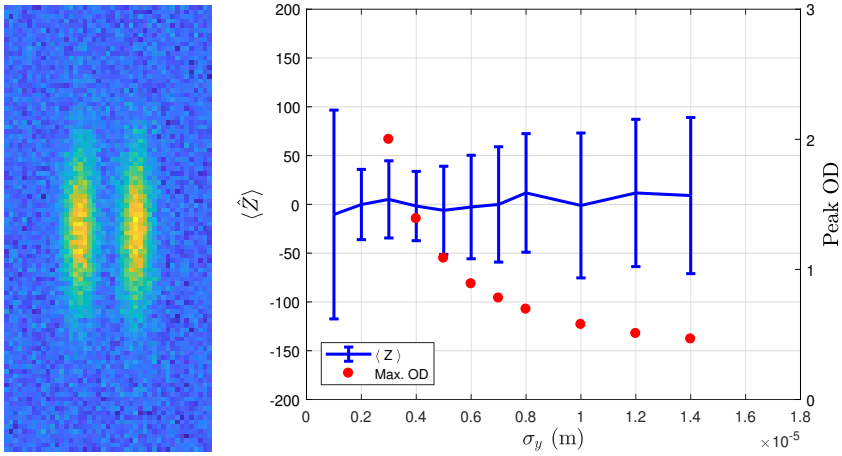

(a) (b)

Figure D.4. (a) shows a typical simulated image of the expanded double-well atom clouds. In this case $N = 5000, \sigma_x = 1\,\mu\text{m}, \sigma_y = 5\,\mu\text{m}$, the separation between clouds is $5\,\mu\text{m}$, and the mean number of photons was 500. For comparison, Fig. 7.5 shows experimental data. (b) shows simulation results from measuring $\langle \hat{Z} \rangle$ for different values of σ_y. Error bars show standard deviation over 50 measurements. Measurements with $2\,\mu\text{m} < \sigma_y < 8\,\mu\text{m}$ appear to show sub-shot-noise resolution (i.e. std. dev.$(\hat{Z}) < 71$).

Bibliography

[1] E. Schrödinger, "Are there quantum jumps? Part II," The British Journal for the Philosophy of Science **3**, 233–242 (1952).

[2] H. Tamura, T. Unakami, J. He, Y. Miyamoto, and K. Nakagawa, "Highly uniform holographic microtrap arrays for single atom trapping using a feedback optimization of in-trap fluorescence measurements," Opt. Express **24**, 8132–8141 (2016).

[3] V. Leong, M. A. Seidler, M. Steiner, A. Cerè, and C. Kurtsiefer, "Time-resolved scattering of a single photon by a single atom," Nature Communications **7**, 13716 (2016).

[4] T. Wilk, S. C. Webster, A. Kuhn, and G. Rempe, "Single-atom single-photon quantum interface," Science **317**, 488–490 (2007).

[5] J. Folch, M. J. Cocero, P. Chesné, J. L. Alabart, V. Domínguez, Y. Cognié, A. Roche, A. Fernández-Árias, J. I. Martí, P. Sánchez, E. Echegoyen, J. F. Beckers, A. S. Bonastre, and X. Vignon, "First birth of an animal from an extinct subspecies (*Capra pyrenaica pyrenaica*) by cloning," Theriogenology **71**, 1026–1034 (2009).

[6] D. J. McCauley, M. Hardesty-Moore, B. S. Halpern, and H. S. Young, "A mammoth undertaking: harnessing insight from functional ecology to shape de-extinction priority setting," Functional Ecology **31**, 1003–1011 (2017).

[7] E. F. Nichols and G. F. Hull, "The application of radiation pressure to cometary theory," Astrophysical Journal **17**.

[8] A. Ashkin, "Acceleration and trapping of particles by radiation pressure," Phys. Rev. Lett. **24**, 156–159 (1970).

[9] S. Chu, J. E. Bjorkholm, A. Ashkin, and A. Cable, "Experimental observation of optically trapped atoms," Phys. Rev. Lett. **57**, 314–317 (1986).

[10] A. Ashkin and J. Dziedzic, "Optical trapping and manipulation of viruses and bacteria," Science **235**, 1517–1520 (1987).

[11] M. D. Barrett, J. A. Sauer, and M. S. Chapman, "All-optical formation of an atomic Bose-Einstein condensate," Phys. Rev. Lett. **87**, 010404 (2001).

[12] M. Greiner, O. Mandel, T. Esslinger, T. W. Hänsch, and I. Bloch, "Quantum phase transition from a superfluid to a mott insulator in a gas of ultracold atoms," Nature **415**, 39 (2002).

[13] T. Graß, R. W. Chhajlany, L. Tarruell, V. Pellegrini, and M. Lewenstein, "Proximity effects in cold atom artificial graphene," 2D Materials **4**, 015039 (2017).

[14] T. L. Nicholson, S. L. Campbell, R. B. Hutson, G. E. Marti, B. J. Bloom, W. McNally, R. L.and Zhang, M. D. Barrett, M. S. Safronova, G. F. Strouse, W. L. Tew, and J. Ye, "Systematic evaluation of an atomic clock at 2×10^{-18} total uncertainty," Nature Communications **6**, 6896 (2015).

[15] G. E. Marti, "Next-generation optical lattice clocks," Presentation at UC Berkeley (2017).

[16] Nobel Media AB 2014. Web. 31 Oct 2017, "The Nobel Prize in Physics 1997," `http://www.nobelprize.org/nobel_prizes/physics/laureates/1997/`.

[17] W. D. Phillips, "Nobel Lecture: Laser cooling and trapping of neutral atoms," Rev. Mod. Phys. **70**, 721–741 (1998).

[18] A. J. Kerman, V. Vuletić, C. Chin, and S. Chu, "Beyond optical molasses: 3D Raman sideband cooling of atomic cesium to high phase-space density," Phys. Rev. Lett. **84**, 439–442 (2000).

[19] E. Öpik, "The lunar atmosphere," Planetary and Space Science **9**, 211 – 244 (1962).

[20] H. J. Metcalf and P. van der Straten, *Laser Cooling and Trapping* (Springer, 1999).

[21] P. D. Lett, R. N. Watts, C. I. Westbrook, W. D. Phillips, P. L. Gould, and H. J. Metcalf, "Observation of atoms laser cooled below the Doppler limit," Phys. Rev. Lett. **61**, 169–172 (1988).

[22] J. Dalibard and C. Cohen-Tannoudji, "Laser cooling below the Doppler limit by polarization gradients: simple theoretical models," J. Opt. Soc. Am. B **6**, 2023–2045 (1989).

[23] W. Bin, L. De-Sheng, Q. Qiu-Zhi, Z. Jian-Bo, L. Tang, L. Liang, and W. Yu-Zhu, "Laser cooling of ^{87}Rb to 1.5 µK in a fountain clock," Chinese Physics Letters **28**, 063701 (2011).

[24] E. L. Raab, M. Prentiss, A. Cable, S. Chu, and D. E. Pritchard, "Trapping of neutral sodium atoms with radiation pressure," Phys. Rev. Lett. **59**, 2631–2634 (1987).

[25] T. Walker, D. Sesko, and C. Wieman, "Collective behavior of optically trapped neutral atoms," Phys. Rev. Lett. **64**, 408–411 (1990).

[26] S. Coop, *An optical mask for atomic interferometry experiments*, Master's thesis, The University of Otago (2014).

[27] A. L. Migdall, J. V. Prodan, W. D. Phillips, T. H. Bergeman, and H. J. Metcalf, "First observation of magnetically trapped neutral atoms," Phys. Rev. Lett. **54**, 2596–2599 (1985).

[28] S. Abend, M. Gebbe, M. Gersemann, H. Ahlers, H. Müntinga, E. Giese, N. Gaaloul, C. Schubert, C. Lämmerzahl, W. Ertmer, W. P. Schleich, and E. M. Rasel, "Atom-chip fountain gravimeter," Phys. Rev. Lett. **117**, 203003 (2016).

[29] W. Muessel, H. Strobel, M. Joos, E. Nicklas, I. Stroescu, J. Tomkovič, D. B. Hume, and M. K. Oberthaler, "Optimized absorption imaging of mesoscopic atomic clouds," Applied Physics B **113**, 69–73 (2013).

[30] E. W. Streed, A. Jechow, B. G. Norton, and D. Kielpinski, "Absorption imaging of a single atom," Nature Communications **3**, 933 (2012).

[31] M. K. Tey, Z. Chen, S. A. Aljunid, B. Chng, F. Huber, G. Maslennikov, and C. Kurtsiefer, "Strong interaction between light and a single trapped atom without the need for a cavity," Nature Physics **4**, 924 (2008).

[32] D. B. Hume, I. Stroescu, M. Joos, W. Muessel, H. Strobel, and M. K. Oberthaler, "Accurate atom counting in mesoscopic ensembles," Phys. Rev. Lett. **111**, 253001 (2013).

[33] G. Reinaudi, *Manipulation et refroidissement par évaporation forcée d'ensembles atomiques ultra-froids pour la production d'un jet intense dans le régime de dégénérescence quantique : vers l'obtention d'un "laser à atomes continu"*, Ph.D. thesis, Université Pierre et Marie Curie - Paris VI (2008).

[34] C. F. Ockeloen, A. F. Tauschinsky, R. J. C. Spreeuw, and S. Whitlock, "Detection of small atom numbers through image processing," Phys. Rev. A **82**, 061606 (2010).

[35] "Rubidium 87 d line data," `http://steck.us/alkalidata/rubidium87numbers.pdf`.

[36] G. Reinaudi, T. Lahaye, Z. Wang, and D. Guéry-Odelin, "Strong saturation absorption imaging of dense clouds of ultracold atoms," Opt. Lett. **32**, 3143–3145 (2007).

[37] J. Kronjäger, *Coherent Dynamics of Spinor Bose-Einstein Condensates*, Ph.D. thesis, Universität Hamburg (2007).

[38] M. Erhard, *Experimente mit mehrkomponentigen Bose-Einstein-Kondensaten*, Ph.D. thesis, Universität Hamburg (2004).

[39] D. M. Stamper-Kurn and M. Ueda, "Spinor bose gases: Symmetries, magnetism, and quantum dynamics," Rev. Mod. Phys. **85**, 1191–1244 (2013).

[40] I. Bloch, J. Dalibard, and S. Nascimbène, "Quantum simulations with ultracold quantum gases," Nature Physics **8**, 267 (2012).

[41] A. D. Ludlow, M. M. Boyd, J. Ye, E. Peik, and P. O. Schmidt, "Optical atomic clocks," Rev. Mod. Phys. **87**, 637–701 (2015).

[42] R. Grimm, M. Weidemüller, and Y. B. Ovchinnikov, "Optical dipole traps for neutral atoms," Advances In Atomic, Molecular, and Optical Physics, **42**, 95 – 170 (2000).

[43] J. P. Brantut, J. F. Clément, M. R. de Saint Vincent, G. Varoquaux, R. A. Nyman, A. Aspect, T. Bourdel, and P. Bouyer, "Light-shift tomography in an optical-dipole trap for neutral atoms," Phys. Rev. A **78**, 031401 (2008).

[44] A. Bertoldi, S. Bernon, T. Vanderbruggen, A. Landragin, and P. Bouyer, "In situ characterization of an optical cavity using atomic light shift," Opt. Lett. **35**, 3769–3771 (2010).

[45] M. Pasienski and B. DeMarco, "A high-accuracy algorithm for designing arbitrary holographic atom traps," Opt. Ex. **16**, 2176–2190 (2008).

[46] K. Huang, *Statistical Mechanics*, 2nd ed. (John Wiley & Sons, 1987).

[47] M. H. Anderson, J. R. Ensher, M. R. Matthews, C. E. Wieman, and E. A. Cornell, "Observation of Bose-Einstein condensation in a dilute atomic vapor," Science **269**, 198–201 (1995).

[48] P. van der Straten and H. J. Metcalf, *Atoms and molecules interacting with light* (Cambridge University Press, 2016).

[49] J. Hu, A. Urvoy, Z. Vendeiro, V. Crépel, W. Chen, and V. Vuletić, "Creation of a Bose-condensed gas of ^{87}Rb by laser cooling," Science **358**, 1078–1080 (2017).

[50] S. Stellmer, B. Pasquiou, R. Grimm, and F. Schreck, "Laser cooling to quantum degeneracy," Phys. Rev. Lett. **110**, 263003 (2013).

[51] H.-J. Miesner, D. M. Stamper-Kurn, M. R. Andrews, D. S. Durfee, S. Inouye, and W. Ketterle, "Bosonic stimulation in the formation of a Bose-Einstein condensate," Science **279**, 1005–1007 (1998).

[52] D. M. Stamper-Kurn, M. R. Andrews, A. P. Chikkatur, S. Inouye, H.-J. Miesner, J. Stenger, and W. Ketterle, "Optical confinement of a bose-einstein condensate," Phys. Rev. Lett. **80**, 2027–2030 (1998).

[53] W. Ketterle and N. V. Druten, "Evaporative cooling of trapped atoms," Advances In Atomic, Molecular, and Optical Physics, **37**, 181 – 236 (1996).

[54] K. M. O'Hara, M. E. Gehm, S. R. Granade, and J. E. Thomas, "Scaling laws for evaporative cooling in time-dependent optical traps," Phys. Rev. A **64**, 051403 (2001).

[55] S. P. Álvarez, *Single domain spinor Bose-Einstein condensate*, Ph.D. thesis, Universitat Politècnica de Catalunya/Institut de Ciències Fotòniques (2017).

[56] T. A. Savard, K. M. O'Hara, and J. E. Thomas, "Laser-noise-induced heating in far-off resonance optical traps," Phys. Rev. A **56**, R1095–R1098 (1997).

[57] J. Jiang, L. Zhao, M. Webb, N. Jiang, H. Yang, and Y. Liu, "Simple and efficient all-optical production of spinor condensates," Phys. Rev. A **88**, 033620 (2013).

[58] H. P. Mishra, A. S. Flores, W. Vassen, and S. Knoop, "Efficient production of an ^{87}Rb $F = 2$, $m_F = 2$ Bose-Einstein condensate in a hybrid trap," The European Physical Journal D **69**, 52 (2015).

[59] Y.-J. Lin, A. R. Perry, R. L. Compton, I. B. Spielman, and J. V. Porto, "Rapid production of ^{87}Rb Bose-Einstein condensates in a combined magnetic and optical potential," Phys. Rev. A **79**, 063631 (2009).

[60] J.-F. Clément, J.-P. Brantut, M. Robert-de Saint-Vincent, R. A. Nyman, A. Aspect, T. Bourdel, and P. Bouyer, "All-optical runaway evaporation to Bose-Einstein condensation," Phys. Rev. A **79**, 061406 (2009).

[61] J. Söding, D. Guéry-Odelin, P. Desbiolles, F. Chevy, H. Inamori, and J. Dalibard, "Three-body decay of a rubidium Bose-Einstein condensate," Applied Physics B **69**, 257–261 (1999).

[62] C. J. Myatt, E. A. Burt, R. W. Ghrist, E. A. Cornell, and C. E. Wieman, "Production of two overlapping bose-einstein condensates by sympathetic cooling," Phys. Rev. Lett. **78**, 586–589 (1997).

[63] B. Arora, M. S. Safronova, and C. W. Clark, "Determination of electric-dipole matrix elements in K and Rb from Stark shift measurements," Phys. Rev. A **76**, 052516 (2007).

[64] C. D. Herold, V. D. Vaidya, X. Li, S. L. Rolston, J. V. Porto, and M. S. Safronova, "Precision measurement of transition matrix elements via light shift cancellation," Phys. Rev. Lett. **109**, 243003 (2012).

[65] I. Novikova, A. B. Matsko, V. L. Velichansky, M. O. Scully, and G. R. Welch, "Compensation of ac Stark shifts in optical magnetometry," Phys. Rev. A **63**, 063802 (2001).

[66] D. Budker and M. Romalis, "Optical magnetometry," Nature Physics **3**, 227–234 (2007).

[67] R. Jiménez-Martínez, S. Knappe, and J. Kitching, "An optically modulated zero-field atomic magnetometer with suppressed spin-exchange broadening," Review of Scientific Instruments **85**, 045124 (2014).

[68] A. C. Lee, J. Smith, P. Richerme, B. Neyenhuis, P. W. Hess, J. Zhang, and C. Monroe, "Engineering large Stark shifts for control of individual clock state qubits," Phys. Rev. A **94**, 042308 (2016).

[69] A. Leszczynski, M. Mazelanik, M. Lipka, M. Parniak, M. Dabrowski, and W. Wasilewski, "Spatially resolved control of fictitious magnetic fields in a cold atomic ensemble," Opt. Lett. **43**, 1147–1150 (2018).

[70] T. Zanon-Willette, E. de Clercq, and E. Arimondo, "Probe light-shift elimination in generalized hyper-Ramsey quantum clocks," Phys. Rev. A **93**, 042506 (2016).

[71] B. H. Bransden and C. J. Joachain, *Physics of Atoms and Molecules*, 2nd ed. (Prentice Hall, 2003).

[72] A. Kaplan, M. Fredslund Andersen, and N. Davidson, "Suppression of inhomogeneous broadening in rf spectroscopy of optically trapped atoms," Phys. Rev. A **66**, 045401 (2002).

[73] F. Schmidt, D. Mayer, M. Hohmann, T. Lausch, F. Kindermann, and A. Widera, "Precision measurement of the ^{87}Rb tune-out wavelength in the hyperfine ground state $f = 1$ at 790 nm," Phys. Rev. A **93**, 022507 (2016).

[74] R. H. Leonard, A. J. Fallon, C. A. Sackett, and M. S. Safronova, "High-precision measurements of the ^{87}Rb D-line tune-out wavelength," Phys. Rev. A **92**, 052501 (2015).

[75] G. A. Costanzo, S. Micalizio, A. Godone, J. C. Camparo, and F. Levi, "ac Stark shift measurements of the clock transition in cold Cs atoms: Scalar and tensor light shifts of the D_2 transition," Phys. Rev. A **93**, 063404 (2016).

[76] F. Le Kien, P. Schneeweiss, and A. Rauschenbeutel, "Dynamical polarizability of atoms in arbitrary light fields: general theory and application to cesium," The European Physical Journal D **67**, 1–16 (2013).

[77] F. Levi, J. Camparo, B. Francois, C. E. Calosso, S. Micalizio, and A. Godone, "Precision test of the ac Stark shift in a rubidium atomic vapor," Phys. Rev. A **93**, 023433 (2016).

[78] S. Coop, S. Palacios, P. Gomez, Y. N. M. de Escobar, T. Vanderbruggen, and M. W. Mitchell, "Floquet theory for atomic light-shift engineering with near-resonant polychromatic fields," Opt. Express **25**, 32550–32559 (2017).

[79] P. D. Gregory, J. A. Blackmore, J. Aldegunde, J. M. Hutson, and S. L. Cornish, "ac stark effect in ultracold polar ^{87}Rb^{133}Cs molecules," Phys. Rev. A **96**, 021402 (2017).

[80] G.-B. Jo, J. Guzman, C. K. Thomas, P. Hosur, A. Vishwanath, and D. M. Stamper-Kurn, "Ultracold atoms in a tunable optical kagome lattice," Phys. Rev. Lett. **108**, 045305 (2012).

[81] E. Vetsch, D. Reitz, G. Sagué, R. Schmidt, S. T. Dawkins, and A. Rauschenbeutel, "Optical interface created by laser-cooled atoms trapped in the evanescent field surrounding an optical nanofiber," Phys. Rev. Lett. **104**, 203603 (2010).

[82] P. F. Griffin, K. J. Weatherill, S. G. MacLeod, R. M. Potvliege, and C. S. Adams, "Spatially selective loading of an optical lattice by light-shift

engineering using an auxiliary laser field," New Journal of Physics **8**, 11 (2006).

[83] R. Kohlhaas, A. Bertoldi, E. Cantin, A. Aspect, A. Landragin, and P. Bouyer, "Phase locking a clock oscillator to a coherent atomic ensemble," Phys. Rev. X **5**, 021011 (2015).

[84] T. Vanderbruggen, R. Kohlhaas, A. Bertoldi, S. Bernon, A. Aspect, A. Landragin, and P. Bouyer, "Feedback control of trapped coherent atomic ensembles," Phys. Rev. Lett. **110**, 210503 (2013).

[85] M. S. Safronova and U. I. Safronova, "Critically evaluated theoretical energies, lifetimes, hyperfine constants, and multipole polarizabilities in ^{87}Rb," Phys. Rev. A **83**, 052508 (2011).

[86] E. Fortson and L. Lewis, "Atomic parity nonconservation experiments," Phys. Rep. **113**, 289–344 (1984).

[87] M. C. Noecker, B. P. Masterson, and C. E. Wieman, "Precision measurement of parity nonconservation in atomic cesium: A low-energy test of the electroweak theory," Phys. Rev. Lett. **61**, 310–313 (1988).

[88] B. K. Sahoo, L. W. Wansbeek, K. Jungmann, and R. G. E. Timmermans, "Light shifts and electric dipole matrix elements in Ba^+ and Ra^+," Phys. Rev. A **79**, 052512 (2009).

[89] J. H. Shirley, "Solution of the Schrödinger equation with a Hamiltonian periodic in time," Phys. Rev. **138**, B979–B987 (1965).

[90] S.-I. Chu, "Recent developments in semiclassical Floquet theories for intense-field multiphoton processes," Advances in Atomic and Molecular Physics, **21**, 197 – 253 (1985).

[91] K. F. Milfeld and R. E. Wyatt, "Study, extension, and application of Floquet theory for quantum molecular systems in an oscillating field," Phys. Rev. A **27**, 72–94 (1983).

[92] A. Kramida, Yu. Ralchenko, J. Reader, and NIST ASD Team, NIST Atomic Spectra Database (ver. 5.3), [Online]. Available: http://physics.nist.gov/asd [2016, September 12]. National Institute of Standards and Technology, Gaithersburg, MD. (2015).

[93] `https://github.com/simocop/LightShiftCalculator`.

[94] J. J. Sakurai and J. Napolitano, *Modern Quantum Mechanics*, 2nd ed. (Addison-Wesley, 2011).

[95] B. Albrecht, Y. Meng, C. Clausen, A. Dareau, P. Schneeweiss, and A. Rauschenbeutel, "Fictitious magnetic-field gradients in optical microtraps as an experimental tool for interrogating and manipulating cold atoms," Phys. Rev. A **94**, 061401 (2016).

[96] K. D. Bonin and T. J. McIlrath, "Two-photon electric-dipole selection rules," J. Opt. Soc. Am. B **1**, 52–55 (1984).

[97] T. H. Taminiau, S. Karaveli, N. F. van Hulst, and R. Zia, "Quantifying the magnetic nature of light emission," Nature Communications **3**, 979 (2012).

[98] C. Cohen-Tannoudji, B. Diu, and F. Laloë, *Quantum Mechanics*, Vol. II (John Wiley & Sons, 1977).

[99] D. Tong, S. M. Farooqi, E. G. M. van Kempen, Z. Pavlovic, J. Stanojevic, R. Côté, E. E. Eyler, and P. L. Gould, "Observation of electric quadrupole transitions to Rydberg *nd* states of ultracold rubidium atoms," Phys. Rev. A **79**, 052509 (2009).

[100] A. Trenkwalder, G. Spagnolli, G. Semeghini, S. Coop, M. Landini, P. Castilho, L. Pezzè, G. Modugno, M. Inguscio, A. Smerzi, and M. Fattori, "Quantum phase transitions with parity-symmetry breaking and hysteresis," Nature Physics **12**, 826–829 (2016).

[101] G. Spagnolli, G. Semeghini, L. Masi, G. Ferioli, A. Trenkwalder, S. Coop, M. Landini, L. Pezzè, G. Modugno, M. Inguscio, A. Smerzi, and M. Fattori, "Crossing over from attractive to repulsive interactions in a tunneling Bosonic Josephson junction," Phys. Rev. Lett. **118**, 230403 (2017).

[102] M. Gustavsson, E. Haller, M. J. Mark, J. G. Danzl, G. Rojas-Kopeinig, and H.-C. Nägerl, "Control of interaction-induced dephasing of Bloch oscillations," Phys. Rev. Lett. **100**, 080404 (2008).

[103] J. Javanainen and M. Y. Ivanov, "Splitting a trap containing a Bose-Einstein condensate: Atom number fluctuations," Phys. Rev. A **60**, 2351–2359 (1999).

[104] C. D'Errico, M. Zaccanti, M. Fattori, G. Roati, M. Inguscio, G. Modugno, and A. Simoni, "Feshbach resonances in ultracold ^{39}K," New Journal of Physics **9**, 223 (2007).

[105] G. Roati, M. Zaccanti, C. D'Errico, J. Catani, M. Modugno, A. Simoni, M. Inguscio, and G. Modugno, "^{39}K Bose-Einstein condensate with tunable interactions," Phys. Rev. Lett. **99**, 010403 (2007).

[106] G. Semighini, *Ultracold atoms in three-dimensional disorder*, Ph.D. thesis, Università degli studi Firenze (2016).

[107] M. Landini, S. Roy, G. Roati, A. Simoni, M. Inguscio, G. Modugno, and M. Fattori, "Direct evaporative cooling of ^{39}K atoms to Bose-Einstein condensation," Phys. Rev. A **86**, 033421 (2012).

[108] M. Albiez, R. Gati, J. Fölling, S. Hunsmann, M. Cristiani, and M. K. Oberthaler, "Direct observation of tunneling and nonlinear self-trapping in a single bosonic Josephson junction," Phys. Rev. Lett. **95**, 010402 (2005).

[109] T. Zibold, E. Nicklas, C. Gross, and M. K. Oberthaler, "Classical bifurcation at the transition from Rabi to Josephson dynamics," Phys. Rev. Lett. **105**, 204101 (2010).

[110] S. L. Cornish, S. T. Thompson, and C. E. Wieman, "Formation of bright matter-wave solitons during the collapse of attractive Bose-Einstein condensates," Phys. Rev. Lett. **96**, 170401 (2006).

[111] E. Haller, M. Gustavsson, M. J. Mark, J. G. Danzl, R. Hart, G. Pupillo, and H.-C. Nägerl, "Realization of an excited, strongly correlated quantum gas phase," Science **325**, 1224–1227 (2009).

[112] G. Semeghini, M. Landini, P. Castilho, S. Roy, G. Spagnolli, A. Trenkwalder, M. Fattori, M. Inguscio, and G. Modugno, "Measurement of the mobility edge for 3D Anderson localization," Nature Physics **11**, 554–559 (2015).

[113] K. Binder, "Theory of first-order phase transitions," Reports on Progress in Physics **50**, 783 (1987).

[114] M. Vojta, "Quantum phase transitions," Reports on Progress in Physics **66**, 2069 (2003).

[115] A. Smerzi, S. Fantoni, S. Giovanazzi, and S. R. Shenoy, "Quantum coherent atomic tunneling between two trapped Bose-Einstein condensates," Phys. Rev. Lett. **79**, 4950–4953 (1997).

[116] S. Raghavan, A. Smerzi, S. Fantoni, and S. R. Shenoy, "Coherent oscillations between two weakly coupled bose-einstein condensates: Josephson effects, π oscillations, and macroscopic quantum self-trapping," Phys. Rev. A **59**, 620–633 (1999).

[117] Y. N. M. de Escobar, S. P. Álvarez, S. Coop, T. Vanderbruggen, K. T. Kaczmarek, and M. W. Mitchell, "Absolute frequency references at 1529

and 1560 nm using modulation transfer spectroscopy," Opt. Lett. **40**, 4731–4734 (2015).

[118] J. Kong, V. G. Lucivero, R. Jiménez-Martínez, and M. W. Mitchell, "Long-term laser frequency stabilization using fiber interferometers," Review of Scientific Instruments **86**, 073104 (2015).

[119] Z. B. Wang, J. W. Zhang, S. G. Wang, K. Miao, and L. J. Wang, "Laser frequency stability transfer using a fiber-based interferometer," Appl. Opt. **53**, 3283–3286 (2014).

[120] "Digilent analog shield," `https://reference.digilentinc.com/analog_shield`.

[121] F. Barone, E. Calloni, R. D. Rosa, L. D. Fiore, F. Fusco, L. Milano, and G. Russo, "Fringe-counting technique used to lock a suspended interferometer," Appl. Opt. **33**, 1194–1197 (1994).

[122] "Corning SMF-28 ultra optical fiber," `https://www.corning.com/media/worldwide/coc/documents/Fiber/SMF-28%20Ultra.pdf`.

[123] H. S. Moon, W.-K. Lee, and H. S. Suh, "Hyperfine-structure-constant determination and absolute-frequency measurement of the Rb $4D_{3/2}$ state," Phys. Rev. A **79**, 062503 (2009).

[124] H.-R. Noh, S. E. Park, L. Z. Li, J.-D. Park, and C.-H. Cho, "Modulation transfer spectroscopy for ^{87}Rb atoms: theory and experiment," Opt. Express **19**, 23444–23452 (2011).

[125] W.-K. Lee and H. S. Moon, "Measurement of absolute frequencies and hyperfine structure constants of $4D_{5/2}$ and $4D_{3/2}$ levels of ^{87}Rb and ^{85}Rb using an optical frequency comb," Phys. Rev. A **92**, 012501 (2015).

[126] M. Joos, *Phase contrast imaging of mesoscopic Bose-Einstein condensates*, Master's thesis, University of Heidelberg (2013).

[127] C. Cohen-Tannoudji and J. Dupont-Roc, *Atom-Photon Interactions* (John Wiley & Sons, Inc, 1992).

[128] A. Putra, D. L. Campbell, R. M. Price, S. De, and I. B. Spielman, "Optimally focused cold atom systems obtained using density-density correlations," Review of Scientific Instruments **85**, 013110 (2014).

[129] T. Tiecke, "Properties of potassium," `http://www.tobiastiecke.nl/archive/PotassiumProperties.pdf`.

[130] A. Keshet and W. Ketterle, "A distributed, graphical user interface based, computer control system for atomic physics experiments," Review of Scientific Instruments **84**, 015105 (2013).

[131] J. Appel, A. MacRae, and A. I. Lvovsky, "A versatile digital GHz phase lock for external-cavity diode lasers," Measurement Science and Technology **20**, 055302 (2009).

[132] G.-B. Jo, Y. Shin, S. Will, T. A. Pasquini, M. Saba, W. Ketterle, D. E. Pritchard, M. Vengalattore, and M. Prentiss, "Long phase coherence time and number squeezing of two Bose-Einstein condensates on an atom chip," Phys. Rev. Lett. **98**, 030407 (2007).